KAON AND NEUTRON SCINTILLATION TIME OF FLIGHT DETECTORS IN A SEARCH FOR A STRANGENESS -2 DIBARYON

by

Victor Sum

A thesis

submitted to the Faculty of Graduate

Studies in partial fulfillment of the

requirements for the degree

of

Master of Science

in

Nuclear Physics

Department of Physics

The University of Manitoba

Winnipeg, Manitoba

January 1992

ISBN 0-315-77724-9

KAON AND NEUTRON SCINTILLATION TIME OF FLIGHT DETECTORS IN A SEARCH FOR A STRANGENESS -2 DIBARYON

BY

VICTOR SUM

A Thesis submitted to the Faculty of Graduate Studies of the University of Manitoba in partial fulfillment of the requirements for the degree of

MASTER OF SCIENCE

Abstract

The performance of a kaon time of flight array comprised of 40 scintillation bars of dimension $5.0 \times 8.5 \times 200$ cm^3 and a pair of neutron time of flight arrays each comprised of 50 scintillation bars of dimension $5.1 \times 15.2 \times 183$ cm^3 is reported. The overall time of flight resolution of the kaon array was 130 ± 20 ps σ including the contribution from the timing start scintillators which had a resolution of 68 ± 8 ps σ. (Thus, by itself, the kaon array time resolution was 100 ± 20 ps σ.) The intrinsic time of flight resolution of the scintillator elements in the neutron time of flight array was 128 ± 15 ps σ. Also, a Monte Carlo simulation was carried out to estimate the neutron detection efficiency of the neutron arrays.

Acknowledgements

A great deal of my gratitude must be bestowed upon Professor W.T.H. van Oers for giving me the opportunity to work on a very interesting experiment and for his enthusiastic support throughout my stay with the University of Manitoba Intermediate Energy Physics group. Within the group, Dr. W.D. Ramsay deserves my sincere appreciation for always making time to discuss various aspects of the experiment with me. Dr. C.A. Davis and Dr. A.R. Berdoz contributed many ideas to the analysis of the calibration data, along with Dr. D.R. Gill of TRIUMF — my thanks to them. Many more people have helped me through my work and my thanks to them them all: Dr. J. Birchall; Dr. S.A. Page; Dr. F. Takeutchi; Dr. R.E. Chrien; Dr. R.J. Sutter; Dr. R. Sawafta and T. Iijima, who helped send much information from Brookhaven to TRIUMF to me; Dr. V. Zeps, who provided much information on the problems with the TDCs; Dr. B Quinn, who provided helpful information on the neutron arrays; and G.H. Coombes, whose practical knowledge was very helpful. Thanks, also, to Steve Chan and Chris Stevens of the TRIUMF scintillator shop for putting up with the mess I made when I used their facility and for the work they did making various objects. Finally, I owe much to my family for providing everything that they have done over so many years.

Contents

List of Figures

List of Tables

1 Introduction

In quantum chromodynamics (QCD) — the quantum field theory of the strong nuclear force — the experimentally observed finite range of the strong interaction has yet to be shown to be a consequence of the theory alone, if indeed it can be shown at all. Notwithstanding this, QCD is thought to be the correct dynamical description of the strong interaction. Although the theory itself is very elegant it is currently extremely difficult to derive quantitative predictions from basic principles. Only in the asymptotic region of high momentum transfer where the fundamental equations of QCD become practically solvable can predictions be made. These predictions agree quite well with experimental results and form the basis of the belief that the theory is correct even in the low momentum transfer regime.

A postulate of QCD allows only quark systems of colour-singlet states to exist. As a consequence, in a three colour quark universe this implies that observable quark systems with quark content $q^m\bar{q}^n$ must obey the triality rule $m - n = 3B$ where B is the baryon number. The commonly observed mesons $(m = 1, n = 1)$ and baryons $(m = 3, n = 0)$ are the first two of a host of quark systems allowed by this rule; however, other than these two hadrons no firm evidence has yet been gathered to establish the existence of more exotic quark systems.

The only fundamental way of deriving predictions from QCD has been with the lattice gauge theories or lattice QCD. This approach is based on a Feynman path integral formulation of QCD in which non-analytic calculations are performed on a discrete four-dimensional lattice of finite size that approximates the space-time continuum. The integrals are estimated through Monte Carlo samples. Very extensive computer computations are required. Numerical results from this approach have yielded good agreement with experimental

results for hadron masses and some coupling constants.

Previously, in the absence of a fundamental analytic methodology for the solution of the equations of QCD in the low momentum regime, several disparate phenomenological models were developed, keeping QCD as their base, in order to make quantitative predictions. These models are: *(i)* the bag models, *(ii)* the Skyrmion models, and *(iii)* the nonrelativistic potential models. Only the bag models will be discussed in any detail in the following.

Bag models are simple phenomenological models that artificially confine quarks inside some region of space. Essentially, the quarks are treated as free relativistic particles in a confined region subject to appropriate boundary conditions. With a limited number of parameters these models generate theoretical masses of the known baryons and mesons which are in quite good agreement with the experimentally determined masses, except for the pion. (See Table 1.)

Beyond yielding the masses of the known three-quark baryons (qqq) and two-quark mesons ($q\bar{q}$), the bag models can predict the masses of the more exotic quark structures such as baryonium ($qq\bar{q}\bar{q}$) and dibaryon (q^6) states. Table 2 shows MIT bag model predictions of dibaryons grouped according to their strangeness and compared to the lightest observed two baryon system of equivalent strangeness. The lightest of the non-strange dibaryons predicted has spin and isospin quantum numbers identical to the deuteron but is approximately 300 MeV more massive. The lightest of the singly-strange dibaryons predicted is approximately 100 to 200 MeV above the ΛN mass. The considerable difference in binding between the singly-strange and the non-strange dibaryons is due to the colour-magnetic interaction of the bag models — the interaction potential being consistent with low order one gluon exchange which causes QCD to display higher binding energies for higher colour symmetry. A doubly-strange dibaryon with the highly symmetric quark content of two up quarks, two down

		M^{exp}	M^{bag} [5]	M^{bag} [5] $- M^{exp}$	M^{bag} [2]	M^{bag} [2] $- M^{exp}$
		[MeV]	[MeV]	[MeV]	[MeV]	[MeV]
	N	939	938	-1	939	0
	Λ	1116	1105	-11	1132	16
	Σ	1193	1144	-49	1209	16
Baryons	Ξ	1318	1289	-29	1361	43
	Δ	1232	1233	1	1232	0
	Σ^*	1385	1382	-3	1383	-2
	Ξ^*	1533	1529	-4	1529	-4
	Ω	1672	1672	0	1672	0
	π	138	280	142	420	282
	K	496	497	1	670	174
	ρ	776	783	7	818	42
Mesons	K^*	892	928	36	959	67
	φ	1020	1068	48	1113	97
	ω	782	–	–	782	0
	η_n	549	–	–	583	34
	η_s	958	–	–	873	-85

Table 1: *Compared to their experimental values, the mass predictions of various hadrons from two bag models. (The experimental masses are averaged for those with more than one charge state.)*

quarks and two strange quarks would have even greater colour-magnetic attraction and, as the models predict, it may be bound. Thus of all the possible dibaryons, the bag models predict that only the $S = -2$ dibaryon will be bound against strong decay, being less than the mass of the lowest $S = -2$ threshold, the $\Lambda\Lambda$. Jaffe [1] first showed that this state consisting of *uuddss* quark content with total spin-parity $J^\pi = 0^+$ may be bound. It is referred to, variously, as the H dibaryon, H dilambda, H particle or simply as the H, which should not be confused with the Higgs boson.

Other bag model [2,3] results have confirmed Jaffe's predictions; however, more refined bag models taking into account centre-of-mass motion [5] and pion-cloud effects [6] give somewhat different H mass predictions some of which are larger than the double-Λ mass — in this case the H would not be bound but would appear as a resonant state.

Non-relativistic potential or quark cluster models are relatively simple models in which quark motions must satisfy a Schrodinger equation based on a quark-quark potential. They predict H masses from about 40 MeV bound to about 30 MeV unbound [7,8].

Skyrmion models are based on a SU(3) chiral-soliton model and do not parameterize the known hadron masses as well as the quark bag models. These models agree on predicting a bound H state, but the predicted binding energies vary considerably — from 20 MeV to 1200 MeV [9,10,11].

Lattice QCD calculations of the H mass have also been performed. Mackenzie and Thacker [12] predicted in 1985 that the H would not be bound. More recently, however, Iwasaki, Yoshie and Tsuboi [13] have predicted a bound H utilizing a larger lattice in their calculations than Mackenzie and Thacker.

The predictions from these and other models are shown in figure 1 . The existence or non-existence of the H particle would significantly affect our un-

	T	I	M^{bag} [1,3]	M^{bag} [1,3] $- M^{exp}$	M^{bag} [2]	M^{bag} [2] $- M^{exp}$
			[MeV]	[MeV]	[MeV]	[MeV]
	0	1	2160	280	2180	300
	1	0	2230	350	2240	360
	1	2	2350	470	2360	480
strangeness 0	0	3	2350	470	2380	500
	2	1	2500	620	2460	580
	3	0	2790	910	2690	810
strangeness -1	$\frac{1}{2}$	1	2160	110	2200–2220	150–170
	$\frac{1}{2}$	2	2230	180	2270–2310	220–260
strangeness -2	0	0	2150	-80	2220–2230	-10–0

Table 2: *Predicted masses of* $S = 0, -1, -2$ *dibaryons from two bag models compared to the lightest observed two baryon systems of equivalent strangeness. I and T are, respectively, spin and isospin.*

derstanding of the nature of QCD in the low momentum regime as it is the basis of all the models above. Ultimately, the validity of QCD theory may be determined through this and other experimental manifestations of the theory. It is in the search for the H that the detectors discussed in this document will play a critical role.

There have been several previous experiments that have searched for the existence of the H. A few experiments searched for resonances in the production cross-sections of $\Xi^- p$ or $\Lambda\Lambda$ pairs [17,18,19] — thus were only sensitive to masses greater than the mass of two Λ particles — but found no evidence of the H. However, these results are of limited value mainly due to their poor statistics.

An experiment designed specifically to find evidence for the H by Carroll *et al.* [20] employing the reaction $p + p \rightarrow K^+ + K^+ + X$, where X may be an H particle, also was unsuccessful. It used 5–6 GeV/c protons for the reaction and searched possible H masses from 2.0–2.5 GeV. An upper limit of about 40 nb for the H production cross-section of this reaction was established; however, later calculations showed that the expected cross-section was less than 1 nb due to the inhibition of the production process caused by the large momentum transfer of the reaction, thus the null result should not have been unexpected. This result suggested that experiments that search for the H should involve a reaction mechanism with low momentum transfer to achieve maximum sensitivity — a feature inherent in the current search described here.

Ejiri *et al.* [21] studied the double weak decay of two nucleons in certain nuclei to form the H particle in the mass region below the two nucleon mass, $M_H < 2M_N$. They considered three types of double weak decays in nuclei: $p + p \rightarrow H + 2e^+ + 2\nu$, $p + n \rightarrow H + e^+ + \nu$, and $n + n \rightarrow H$. The decay rate for each of these processes was evaluated theoretically as second order perturbations of the hamiltonian of leptonic and non-leptonic processes (leptonic for

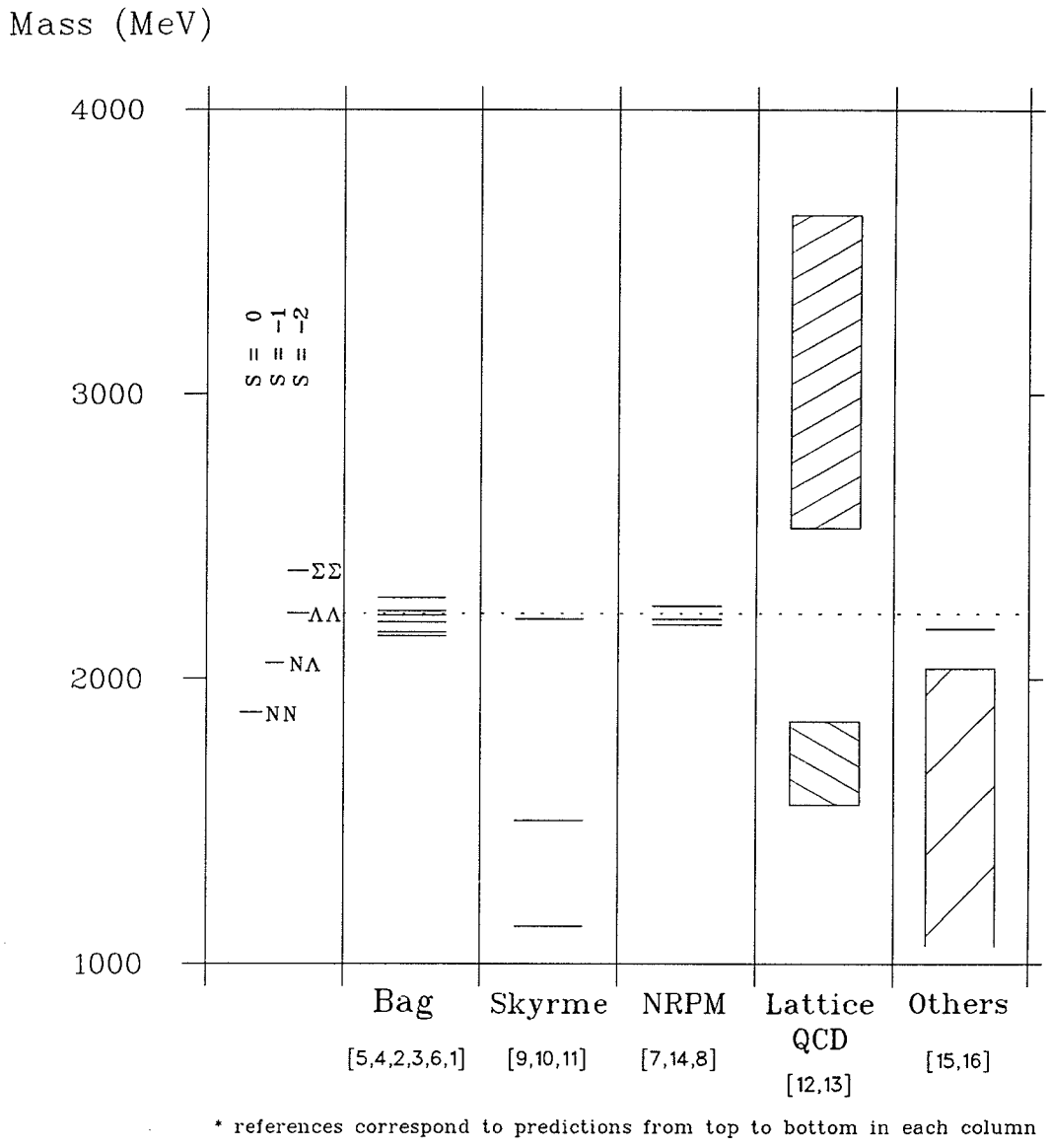

Figure 1: *Predictions from various quark confinement models and lattice gauge theories compared to some six quark thresholds. (The dashed line corresponds to the* $\Lambda\Lambda$ *mass.)*

pp, both leptonic and non-leptonic for pn, and non-leptonic for nn). The pp decay rate was insignificantly small, 10^{-21} – 10^{-18} /year, hence this process was disregarded. The nn decay rate calculation for ^{72}Ge and ^{74}Ge were compared to double weak decay data for germanium. The respective double weak decays were $^{72}\mathrm{Ge} \rightarrow ^{70}\mathrm{Ge}(2^+) + H$ and $^{74}\mathrm{Ge} \rightarrow ^{72}\mathrm{Ge}(2^+) + H$ where the resulting germanium decay products are in the first excited state with spin-parity $J^\pi = 2^+$ and the signature for these decays would be sharp peaks in the decay spectrum coming from the decay of the excited germanium nuclei. No relevant peaks appeared in the germanium decay spectrum. The pn decay rate was calculated for the reaction $^{127}\mathrm{I} \rightarrow ^{125}\mathrm{I} + H + e^+ + \nu$ and was compared to an experimentally obtained decay rate spectrum for ^{127}I which led to negative results. Each of the results above placed a lower bound to the mass of the H; 1861.4 MeV and 1859.9 MeV for the ^{74}Ge and ^{72}Ge results, respectively, and 1862 MeV for the iodine result. However, the highest lower limit was arrived at by calculating the double weak decay half-life of the deuteron, $d \rightarrow H + e^+ + \nu$, and this placed a lower limit of 1875.1 MeV on the mass of the H.

Results from Shahbazian *et al.* [22] of propane bubble-chamber tracks in a 10 GeV/c proton beam appear to show evidence of the H in two events. The second of the two has been interpreted as the weak decay of a stable dibaryon via $H \rightarrow p + \Sigma^-$, $\Sigma^- \rightarrow n + \pi^-$ and a mass of $M_H = 2218 \pm 12$ MeV was calculated with a confidence level of 69.4% that the event was such an occurrence.

An investigation by Alekseev *et al.* [23] of H production by colliding neutrons onto carbon and copper nuclei appears to have produced two events that show the existence of the H. A neutron beam of 3–10 GeV/c, extracted from the internal target of a 10 GeV proton synchrotron, was directed at either a 6 cm thick carbon target or a 4 cm thick copper target and the outgoing reaction products were tracked through a magnetic spectrometer instrumented with spark chambers and scintillating counter hodoscopes. H production via the re-

action $n + A \rightarrow H + X^0$, where A is the target nucleus and X^0 is a neutral particle, was searched for by looking for the decay $H \rightarrow p + \pi^- + \Lambda$ and the subsequent decay of $\Lambda \rightarrow p + \pi^-$. The instrumentation was tuned to trigger on events which produced two collision vertices hopefully corresponding to the decay of the H and the decay of the subsequent Λ. Of the 2×10^6 total trigger events two events passed the criteria that were established for identifying the above decay of the H. The confidence levels for the hypothesis that each of the two events was a H dibaryon were 59.5% and 73.8% and the measured mass of the H is $M_H = 2220.1 \pm 5.4$ MeV.

Another recent experiment, this one at KEK by Aoki *et al.* [24], was unsuccessful in finding the H. Using a 1.66 GeV/c separated K^- beam directed at an emulsion target in a hybrid emulsion-counter detector system no evidence of H production was observed in the mass range 1.90–2.16 GeV; however, an event recorded in the emulsion was uniquely identified, by kinematic arguments, to be the formation and sequential weak decay of a double-Λ hypernucleus [25]. The elementary processes in the reaction are $K^- + p \rightarrow K^+ + \Xi^-$, $\Xi^- + p \rightarrow \Lambda + \Lambda$ where the proton in the latter reaction is embedded in an emulsion nucleus. Using kinematic arguments, the event was interpreted to be either the capture of a Ξ^- by ^{12}C or ^{14}N which then forms a double hypernucleus ($S = -2$) identified as either ${}^{10}_{\Lambda\Lambda}$Be or ${}^{13}_{\Lambda\Lambda}$B, respectively. The double hypernucleus then decays via a weak interaction. Thus this precludes the existence of a strongly bound H since if it were strongly bound the double hypernucleus would decay with the H as a product. Kerbikov [26] has argued that the weak decay of a double hypernucleus excludes the mass of the H particle being below $2M_\Lambda - B_{\Lambda\Lambda}$ where $B_{\Lambda\Lambda}$ is the binding energy of the two Λ hyperons in the nucleus. The binding energies calculated for the above possibilities were $B_{\Lambda\Lambda} = 8.5 \pm 0.7$ MeV for the ${}^{10}_{\Lambda\Lambda}$Be case and $B_{\Lambda\Lambda} = 27.5 \pm 0.7$ MeV for the ${}^{13}_{\Lambda\Lambda}$B case. Hence the lower bound for the H particle mass is 2222.8 ± 0.7 MeV if the double hypernucleus is ${}^{10}_{\Lambda\Lambda}$Be or

the lower bound is 2203.8 $\pm$ 0.7 MeV if the double hypernucleus is ${}^{13}_{\Lambda\Lambda}$B. Dover, Millener, Gal and Davis [27] have analysed this event and argue that the ${}^{13}_{\Lambda\Lambda}$B is the correct interpretation for the recorded event. They demonstrate the reaction mechanism and decay sequences for this interpretation are favored over the other interpretation. The ${}^{10}_{\Lambda\Lambda}$Be interpretation results in a strongly repulsive $\Lambda\Lambda$ interaction which is contrary to any reasonable model that the authors suggest.

2 The Experiments

The search for the H particle is being conducted at the Alternating Gradient Synchrotron at Brookhaven National Laboratory utilizing a newly constructed 1-2 GeV/c beamline. Two separate experiments, sensitive to different mass regions of the H, have been approved to run at this facility. The first version, Experiment 813, uses a dual-chamber liquid hydrogen/liquid deuterium (LH_2/LD_2) target and will be sensitive to H particle binding energies, B_H, from ~20 MeV unbound to ~100 MeV bound. A second version, Experiment 836, with a liquid helium-3 (L^3He) target, will be sensitive up to ~350 MeV bound.

2.1 The LH_2/LD_2 Version

This version of the search, which started running in the spring of 1991, relies on the following multistep reaction mechanism for the formation of the H:

$$K^- + p \longrightarrow K^+ + \Xi^-$$

$$\Xi^- + d \longrightarrow (\Xi^- d)_{\text{atom}}$$

$$(\Xi^- d)_{\text{atom}} \longrightarrow H + n$$

A 1.8 GeV/c kaon, K^-, in the beam is incident upon a proton in the LH_2 target and reacts to yield K^+ and Ξ^-. The Ξ^- hyperon is slowed down in a tungsten energy degrader and passes through a solid state detector before entering the LD_2 chamber where it comes to rest and is captured by a deuteron to form the bound atomic system $(\Xi^- d)_{\text{atom}}$. The $(\Xi^- d)_{\text{atom}}$ may then decay through the capture of the orbiting Ξ^- hyperon by the deuteron nucleus to produce an H and a neutron. See figure 2 for a schematic representation of the reaction (a possible decay of the H is included).

By measuring the scattering angles and the momenta of the incident K^-

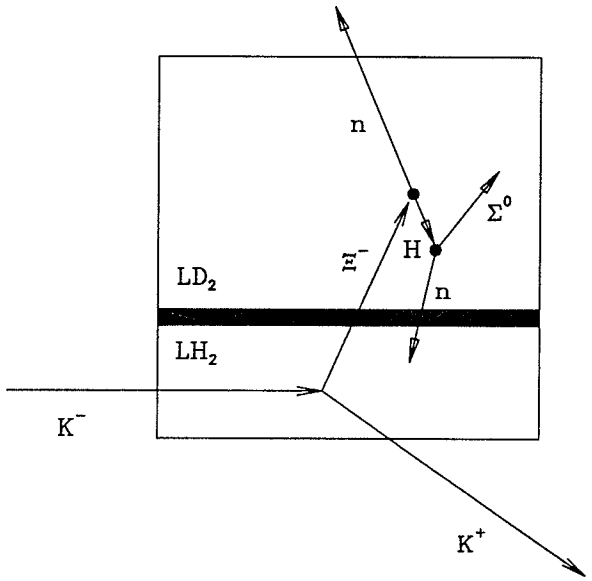

Figure 2: *The anticipated H production reaction with a 1.8 GeV/c K^- incident upon the dual chamber target. The decay products of the H are mass dependent but a possible decay of the H is shown.*

Table 3: *Some kinematic data for the $p(K^-, K^+)\Xi^-$ reaction around the region of interest for the spectrometer and detector setup for Experiment 813.*

$\theta^{lab}_{K^+}$ (°)	$p^{lab}_{K^+}$ (MeV/c)	$\theta^{lab}_{\Xi^-}$ (°)	$T^{lab}_{\Xi^-}$ (MeV)
5.0	1292	12.4	100.7
5.5	1289	13.5	102.8
6.0	1287	14.5	105.0
6.5	1284	15.5	107.5
7.0	1281	16.5	110.2
7.5	1278	17.4	113.0
8.0	1275	18.3	116.1
8.5	1272	19.1	119.3
9.0	1268	19.9	122.6
9.5	1264	20.7	126.2
10.0	1260	21.4	130.0

and outgoing K^+ in the initial reaction, the Ξ^- trajectory and recoil energy can be completely determined since it is a two body reaction. The short lifetime of the Ξ^-, 166ps, makes it necessary to carefully control the target geometry and production kinematics to ensure that there is a high probability of the Ξ^- stopping in the liquid deuterium. Thus the path length between the production point in the liquid hydrogen and the LD_2 vessel must be kept to a minimum. This is accomplished by having a K^- beam with a well defined phase space focused tightly, with small divergence, on a thin sandwich LH_2 target and by using those Ξ^- with recoiling lab angles near their maximum angle, $\sim 20°$ for K^+ lab angles around 10°.

The formation of the H from the $(\Xi^- d)_{\rm atom}$ is as follows: The S and P atomic wavefunctions of a Ξ^- orbiting a deuteron have a large overlap with the nucleus even for large principle quantum numbers n. The overlap is large enough to presume that the particles interact via the strong force. When the stopping Ξ^- is captured by a deuteron to form a $(\Xi^- d)_{\rm atom}$ it will initially be in a high n orbital and will be distributed throughout the available angular momentum states. These atoms in high angular momentum states will undergo electromagnetic transitions to lower angular momentum states through collisions with neighbouring deuterium atoms. The average time for the transition to S or P states is a small fraction of the Ξ^- lifetime and it is expected that less than 20% of the $(\Xi^- d)_{\rm atoms}$ will be lost due to weak decay before undergoing a strong interaction [28]. There are three strong interactions and one significant weak interaction branch for the $(\Xi^- d)_{\rm atom}$ bound system. These are:

$$
\begin{array}{lllllll}
(\Xi^- d)_{\rm atom} & \longrightarrow & H + n & + & 29\ \text{MeV} & + B_H & \text{strong} \\
 & \longrightarrow & \Lambda + \Lambda + n & + & 29\ \text{MeV} & & \text{strong} \\
 & \longrightarrow & \Xi^0 + n + n & + & 3\ \text{MeV} & & \text{strong} \\
 & \longrightarrow & d + \Lambda + \pi^- & + & 66\ \text{MeV} & & \text{weak}
\end{array}
$$

Aerts and Dover [29] have calculated the branching ratio of the $(\Xi^- d)_{\rm atom}$ to form the H in the strong interaction. While model dependent, the ratio may be as high as 0.9 in the S state for an H mass near the $\Lambda\Lambda$ mass ($B_H \sim 0$) and decreases exponentially as the binding energy becomes larger. At $B_H \sim$ 100 MeV, the branching ratio decreases to 0.1; this figure is significant since an adequate count rate and signal to noise ratio is not expected for branching ratios much less than 0.1.

The two body reaction of the $(\Xi^- d)_{\rm atom}$ corresponding to H particle production means that the accompanying neutron is monoenergetic, therefore, the

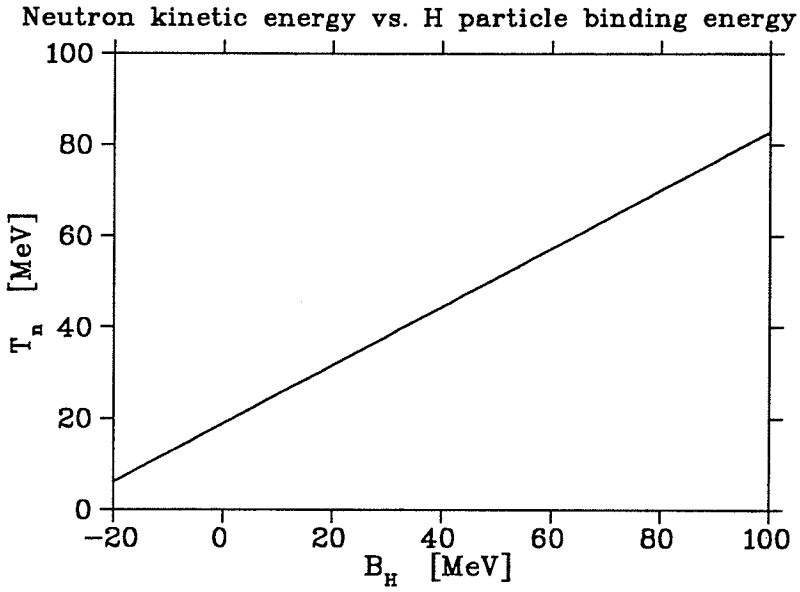

Figure 3: *The relationship between the kinetic energy of the neutrons and the binding energy of an H particle resulting from the decay of the* $(\Xi^- d)_{\rm atom}$.

detection of monoenergetic neutrons would signify the production of H particles and a measurement of the neutron energy would give a measure of the H particle mass. As the mass of the $(\Xi^- d)_{\rm atom}$ is 29 MeV above that of the $\Lambda\Lambda$ mass an unbound H may be produced as long as it is unbound by no more than 29 MeV. However, as a practical matter, the neutrons would have an energy too low to detect for an unbound H of more than 20 MeV. Hence this version of the experiment is sensitive from $B_H \sim -20$ MeV (unbound) to $B_H \sim$100 MeV and the corresponding neutron energies are, respectively, 6 MeV and 90 MeV varying monotonically in between as plotted in figure 3.

Table 3 lists some of the kinematic parameters for the initial $p(K^-, K^+)\Xi^-$ reaction in the region of interest.

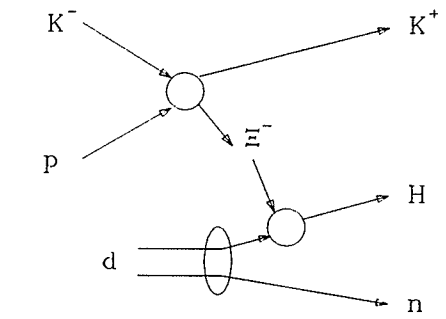

Two Step Process

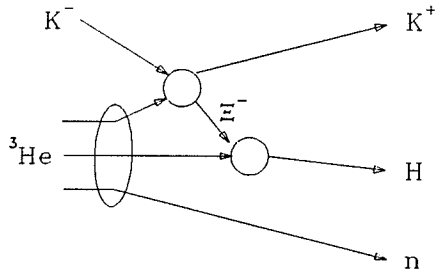

One Step Process

Figure 4: *Comparison of the one and two step* H *particle production reactions.*

2.2 L^{3}He Version

As opposed to the double step reaction with a LH_2/LD_2 target a L^{3}He target with the same incident kaon beam may produce H dibaryons in the single step, double strangeness exchange reaction

$$K^- + {}^3\mathrm{He} \longrightarrow K^+ + n + H.$$

The two H production reactions are quite similar as can be seen in figure 4.

For incident K^- of 1.8 Gev/c, measurement of the trajectories and the momenta of the outgoing K^+ and neutron can then be used with kinematics to calculate the mass of the resulting H. In fact, Aerts and Dover [30] have shown that the neutron need not be detected in certain circumstances to determine the

H mass. For a K^+ lab scattering angle of 0°, the K^+ detection and momentum measurement, by itself, would suffice. The K^+ spectrum should be a peak with a 30 MeV/c FWHM due to broadening caused by the Fermi momentum of the p-p system. The detection of the neutron, however, would improve resolution.

Background rejection is of great importance with the L^{3}He target experiment. The background reactions can be separated into two categories. The first includes misidentification of incoming or outgoing particles in production reactions and the second are quasi-free production of Ξ^- hyperons from the reaction $K^- + {}^3\mathrm{He} \rightarrow K^+ + \Xi^- + p + n$. The misidentification of the outgoing π^+ as a K^+ in the following three reactions with a proton in the ^{3}He nucleus could produce a significant background:

$$\begin{aligned} K^- + p &\longrightarrow \pi^+ + \Sigma^- \\ K^- + p &\longrightarrow \pi^+ + Y* \\ K^- + p &\longrightarrow \pi^+ + \pi^- + \Lambda \end{aligned}$$

The sum of these three reaction cross sections is three orders of magnitude larger than the expected H production cross section as calculated by Aerts and Dover [29] and shown in figure 5. The inefficiency in rejecting the outgoing π^+ can be no more than 1 in 10^4 or else structure from the π^+ background reactions will appear that will simulate an H production signal.

The incident K^- beam is far from pure as will be discussed later. It is expected to be contaminated with an equal number or more of π^- mesons which may produce background events if it is misidentified as a K^- through the reaction:

$$\pi^- + p \longrightarrow K^+ + \Sigma^-$$

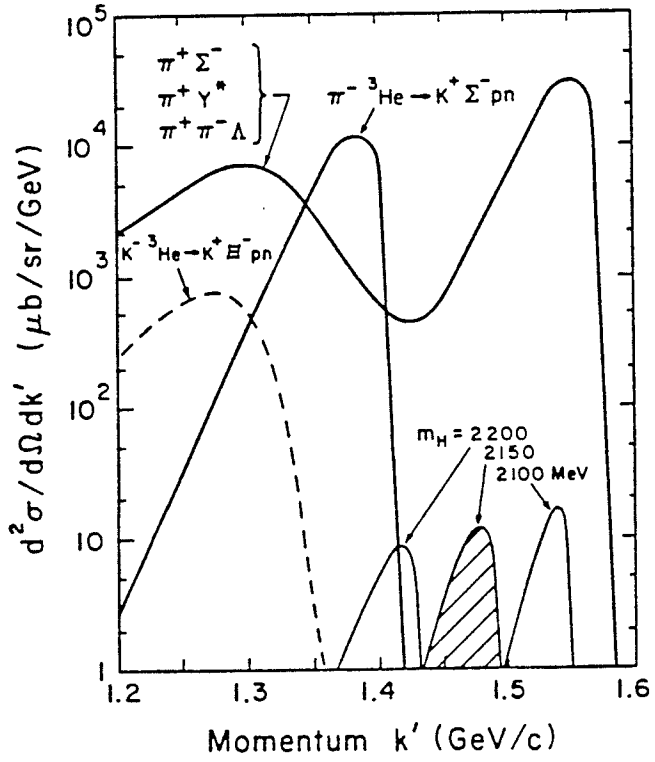

Figure 5: *Background reactions in the ^3He measurement.*

A similar particle identification requirement of 1 error in 10^4 will be needed in the beamline to reduce this background. This misidentification places the upper limit on the mass region of sensitivity.

2.3 Experimental Facility

As mentioned above, the search for the H particle is being conducted at the Alternating Gradient Synchrotron (AGS) at Brookhaven National Laboratory which is located on Long Island, New York. The AGS is a proton synchrotron that can accelerate protons up to a maximum energy of 32 GeV.

The 1.8 GeV/c K^- beam is produced in a new low energy (1-2 GeV/c momentum) secondary meson beamline completed in early 1991 [31]. A layout of the beamline is shown in figure 6.

The kaons are produced at the platinum production target just upstream of the dipole D1 into which 24 GeV protons are directed. In addition to the kaons many other particles, primarily pions, are produced which must be separated out. This is accomplished with the series of magnets, electrostatic separators and apertures that make up the beamline. Separation of the kaons is done in two steps; each step in one of the two segments of the beamline arm — Q1 to MS1 and H4 to MS2 in figure 6. Each segment consists of:

1. the upstream quadrupoles which focus the beam before it enters the separator;

2. the correcting (dipole) magnets and separator combination which spatially separates the various particles in the beam in the vertical direction;

3. the downstream quadrupoles which focus the separated beam at the mass slit;

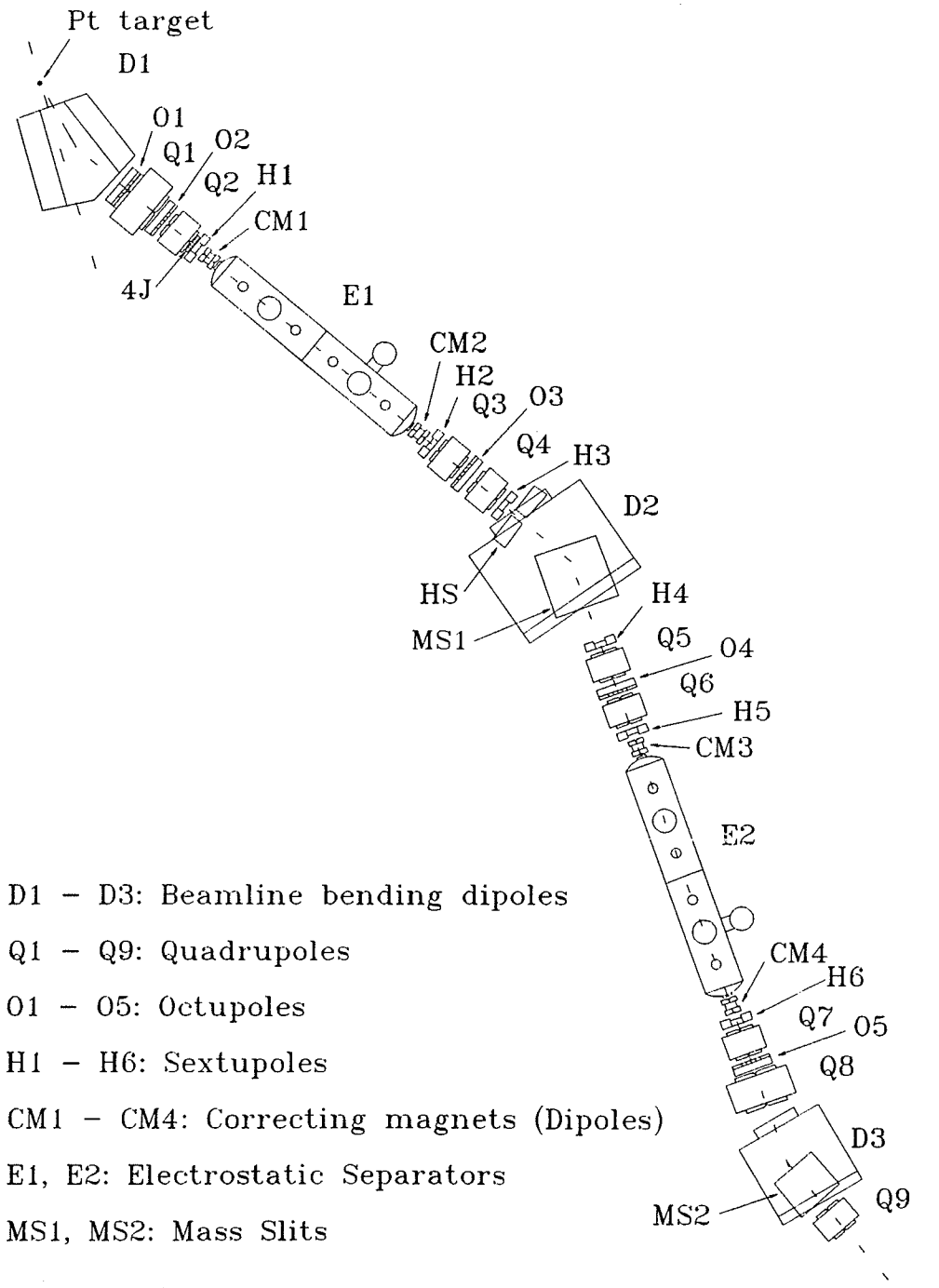

Figure 6: *The new 1-2 GeV/c separated beamline at the AGS.*

4. the sextupoles and octupoles which correct the second and third order vertical focussing aberrations, respectively, at the mass slit; and

5. the mass slit which is a horizontal slit made of thick heavy metal that is centered on the kaons in the beam.

The first segment removes the primary contamination (mostly pions) from the beam while the second segment removes contamination from secondary sources such as particles scattering off the beamline elements, from the decay of short-lived hyperons near the target and from the decay of kaons and pions in the beam itself.

Essentially, the beamline is symmetrical about mass slit 1 (MS1) between dipoles D1 and D3. This design is preferred since many of the aberration coefficients are automatically zero for such a system. The 30° bend in the beamline introduced by dipole D2 was made necessary by space constraints in the existing facilities. The 4-jaw collimator (4J) removes additional pions which are at the fringe of the beam at that location but do pass through the mass slits farther downstream as shown by beam modelling studies. The momentum slit (HS) is a vertical slit used to restrict the momentum range of the particles in the beam. Finally, the last quadrupole in the beamline (Q9) focuses the beam onto the experimental target.

Table 4 shows some expected properties of the beamline. Note that even with the use of two separators the expected composition of the beam at the end of the beamline is approximately three π^- for every K^-. Some data from the initial running of the beamline from April to June 1991 is given in table 5. Note that the electrostatic static separators were not running up to specification (750 kV) during the beam time thus a 1.7 GeV/c beam was used to increase the kaon to pion ratio.

Table 4: *Some expected characteristics of the new beamline.*

1-2 GeV/c Beamline	
Production Parameters	
Primary Proton Intensity	10^{13} protons/spill
Target	0.6cm×1cm×9cm platinum
Production Angle	5°
Beamline Acceptance	
Momentum Range	1-2 GeV/c
Momentum Bite	±3%
Horizontal	±50 mr
Vertical	±8 mr
K-π Separation	
First Mass Slit	3.3 mm
Second Mass Slit	8.0 mm
Estimated Rates At Experimental Target (per 10^{13} proton spill)	
K^-	3.2 ×10^6 /spill
K^+	1.1 ×10^7 /spill
π^-	5.0 ×10^8 /spill
π^+	5.6 ×10^8 /spill
Beam Parameters at Experimental Target	
Horizontal Size	5 cm
Vertical Size	0.5 cm
Horizontal Divergence	30 mr
Vertical Divergence	12 mr
K^-/π^-	1/3

Table 5: *Some results of the 1991 run of the 2 GeV/c beamline.*

Particles/spill with 10^{13} 24 GeV/c protons:				
Momentum (MeV/c)	K^-	π/K	$\bar{p}$	$\pi/\bar{p}$
1000	26,000	0.056:1	21,000	0.14:1
1270	125,000	0.28:1	77,000	0.030:1
1500	320,000	1.0:1	-	-
1700	811,000	3.5:1	510,000	0.022:1

For 1700 MeV/c K^-:		
Condition	K flux	π/K
Sextupoles on and Octupoles on	811,000	3.5:1
Sextupoles off and Octupoles on	10% reduction	33% worse
Sextupoles on and Octupoles off	5% reduction	8% worse

Conditions:

1. Mass Slit #1 (MS1) = 1.8 mm for K^- and 2.7 mm for $\bar{p}$
2. Mass Slit #2 (MS2) = 4 mm for K^- and 5 mm for $\bar{p}$
3. Momentum Slit (HS) 15% closed
4. Theta-Phi (4Jaw) Collimator:

   Lower Left = Closed

   Upper Left = 2/3 Closed

   Upper Right = 2/3 Closed

   Lower Right = Open
5. Separator #1 (E1) = 590 kV
6. Separator #2 (E2) = 600 kV
7. Tune = RAYTRACE with $x/\theta = -.04$ (minimum horizontal image size) and $y/\phi = 0$ at final focus
8. All Sextupoles and Octupoles set to RAYTRACE values

2.4 Experimental Apparatus

2.4.1 Overview

A variety of detectors is required to gather the information necessary to determine, unambiguously, the collision events that occur in the target. Information on position, timing and energy are necessary to accomplish this task. The detector components being utilized in the H particle search experiments can be grouped into four major systems. These are:

1. the experimental target,
2. the in-beam particle tracking and identification detectors,
3. the K^+ spectrometer (including particle identification) and
4. the neutron arrays.

All these systems, except for the target, are common to both BNL Experiments 813 and 836 and have been designed to be as compatible with each version as possible. A brief discussion of these systems will be given here with a more detailed description of the apparatus to follow immediately after a short introduction to detector concepts. A detailed discussion of the neutron arrays and the K^+ time of flight detector will be presented in the following chapters. Figure 7 shows a schematic diagram of the experimental apparatus. Table 6 lists the abbreviated names of the various detectors.

As discussed above, Experiment 813 uses a dual-chamber LH_2/LD_2 target while Experiment 836 uses a L^3He target. The LH_2/LD_2 is an active target which integrates a solid state transmission detector strip into its design. It consists of 160 silicon detectors positioned on the exit face of the tungsten energy degrader wedges which are used to slow down the Ξ^- from the reaction of interest in the hydrogen, $p(K^-, K^+)\Xi^-$, so that they stop in the deuterium. These

Table 6: *List of detectors for E813/836.*

Key to the detector names:

SWIC	Segmented Wire Ionization Chamber
MP	Mass Position Hodoscope
MT	Mass Timing Detector
MD1	Mass Drift Chamber
IV	Incident Beam Veto
IDn	Incident Drift Chamber
IT	Incident Timing Detector
IC	Incident Čerenkov Detector
K	Silicon detectors (Expt. 813 only)
LN	Left Neutron Array
LV	Left Veto
RN	Right Neutron Array
RV	Right Veto
FDn	Forward Drift Chamber
FC	Forward Čerenkov Detector
FP	Forward Position Hodoscope
BDn	Back Drift Chamber
BC	Back Čerenkov Detector
BP	Back Position Hodoscope
BCL	Back Lucite Čerenkov Detector
BT	Back Timing Hodoscope
BS	Back Calibration Fingers for BT

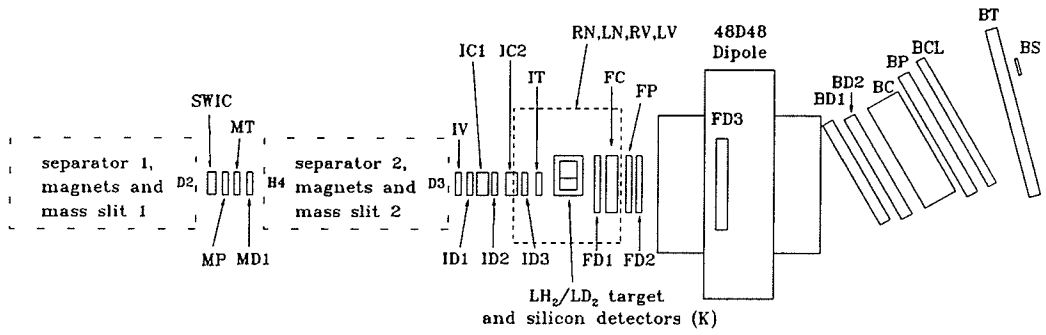

Figure 7: *Side view of the detector layout with the Experiment 813 target. (See table 6 for key to detector names.)*

detectors will help suppress background from misidentification of the outgoing K^+ and from accidental coincidences. Also, at best, only a small number of the Ξ^- produced with trajectories passing into the LD_2 can be expected to come to rest in the LD_2 before decaying, thus by requiring a hit in an appropriate silicon detector events which have a large probability forming a $(\Xi^- d)_{\text{atom}}$ may be selected.

The in-beam detectors include wire chambers, threshold Čerenkov detectors and scintillation counters. The K^+ spectrometer is a multi-component instrument consisting of a large dipole magnet with a 0.5 metre aperture, a series of wire chambers for charged-particle tracking, threshold Čerenkov detectors, and scintillation hodoscope and time-of-flight detectors: the two former items are for charged-particle momentum determination and the two latter items are for particle identification. The neutron arrays are composed of plastic scintillators which cover a solid angle of about $\frac{1}{5}$ of 4π around the target and are 30–50% efficient, depending on the neutron energy. The following will give a short description of the various types of detectors just mentioned.

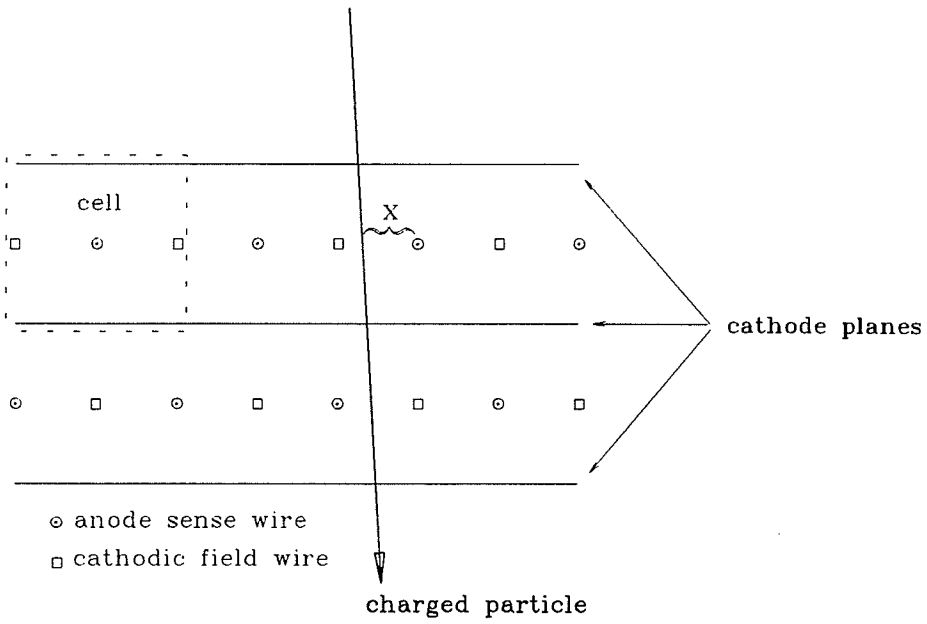

Figure 8: *Drift chamber cross-section.*

2.4.2 Drift Chambers

Drift chambers are instruments which can accurately determine position information and are used to measure the trajectories of charged particles. Figure 8 is a schematic of a cross-section of such a device that gives position in one coordinate.

The chamber is made up of a set of parallel anode sense wires sandwiched between two planar cathode surfaces. Cathode field wires at a lower potential than, and positioned in between, the anode sense wires divide the chamber into a set of cells around each anode wire. The region in between the cathode planes is filled with a gas. When a charged particle passes through a cell it ionises the gas along its path of traversal. The electrons thus produced are swept by the electric field toward the anode sense wires while the corresponding positive ions are swept toward the cathode. As the electrons move to within a few diameters of the anode wire the electric field they encounter becomes very intense due to the $\frac{1}{r}$ dependence around the wire. Multiplication of the number of electrons

occurs as electrons accelerated toward the anode wire gain sufficient energy to ionize the gas to produce secondary electrons. A signal is generated in the anode wire by the collection of these electrons and by that induced by the positive ions created near the wire. The chamber gas used is chosen for its gain in the electron multiplication process, its x-ray inefficiency, and, most importantly, for its electron drift velocity characteristics. By knowing the drift velocity of the electrons in the gas it is possible to determine the distance from the anode sense wire at which a charged particle passes through the plane of the wires. (The distance x in figure 8.) However, which side of the anode sense wire the particle passes by cannot be determined by the single wire plane shown. One way to determine this is to place a second plane of wires directly behind the first plane with its anode sense wires positioned in between those of the first as shown in figure 8. With the additional information from the second plane the ambiguity is removed if the angle of the particle relative to plane of the chamber is not too large. If the incident angle of the particle is known then the data from the two planes can be used to define the particle trajectory more accurately even for large angles. Typically, the spatial resolution obtainable from a drift chamber is in the order of a few hundred μm. By stacking two pairs of wire planes perpendicular to each other, two spatial coordinates may be obtained for an ionizing event. The trajectory of a charged particle can be measured by using two or more aligned drift chambers set a distance apart.

The drift chambers used in the H particle search are mostly constructed with adjacent wire planes rotated by 60°. In figure 7 and table 6 MD1, ID1, ID2, ID3, FD1, FD2, FD3, BD1, and BD2 are drift chambers.

2.4.3 Organic Plastic Scintillators

The scintillation process, which occurs when an ionizing particle loses some energy when passing through certain materials thereby causing the material to emit some electro-magnetic radiation as the energy is dissipated, has been utilized in the study of nuclear physics since its inception at the turn of this century when the naked human eye was the instrument used to detect the scintillation of a ZnS screen in alpha scattering experiments. Since then, the development of photomultiplier tubes and of modern organic plastic scintillators has kept this process as an indispensable tool in the study of nuclear and particle physics.

These plastic scintillators are composed of a small amount ($\sim$ a few % by volume) of fluorescent aromatic hydrocarbons dissolved in a base of solid polymerized plastic solvent (commonly polyvinyltoluene or polystyrene.) The mechanism by which these materials scintillate is somewhat involved (see *eg* Birks [32]) but, essentially, the light released originates from the molecular bonding electrons, which are not associated with any particular atom in the aromatic molecule, when they return to their ground state after being excited to higher energy states by ionizing radiation. An important property of these materials is that the molecules have absorption and emission spectra at different wavelengths, hence they are transparent to their own radiation. The differing absorption and emission wavelengths arise from the different shapes of the excited and ground-state electron energy levels as a function of the interatomic spacing as depicted in figure 9 and from the interplay of the vibrational states of the lattice on those energy levels. The electronic levels are typically a few eV while the vibrational levels of the molecule are typically a few tenths of eV. Consider an electron initially at the ground state energy level that is excited into an excited state energy level (A $\rightarrow$ B). The electron is also in an excited vibrational state so that it begins to decay and transfer some of its energy to the lattice and moves

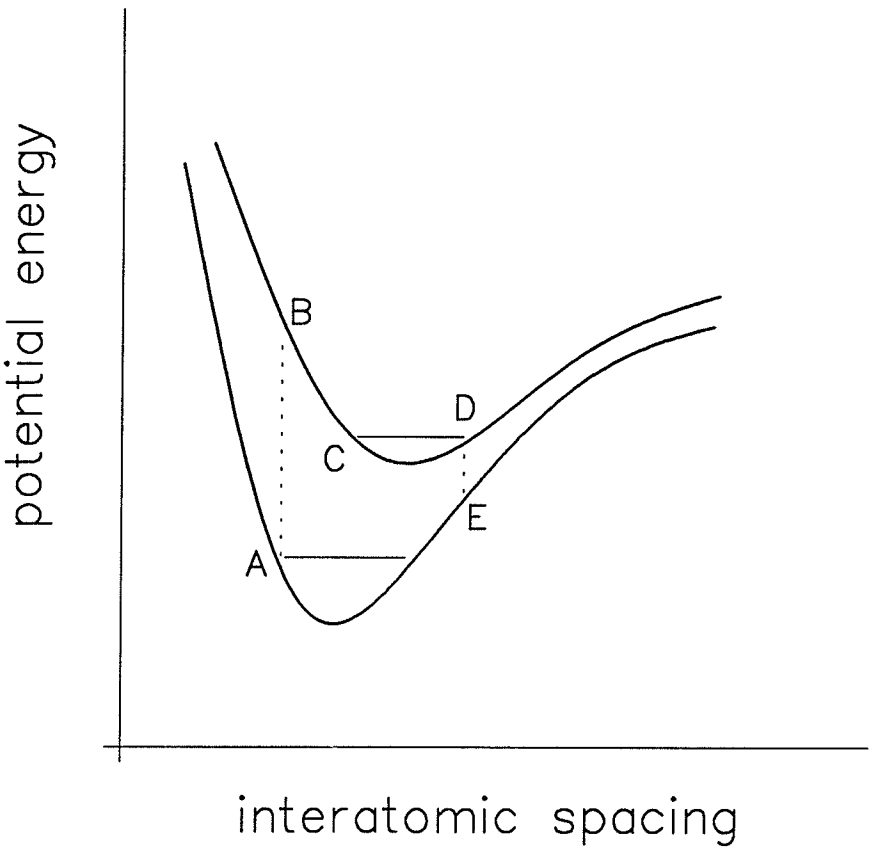

Figure 9: *Molecular potential energy versus interatomic spacing for plastic scintillator. (See text for details.)*

down to the level CD. A short amount of time later the electron decays to some vibrational energy level of the electromagnetic ground state. The vibrational states then decay back to the initial vibrational energy level in the ground state. The combination of differing energy level functions and vibrational energy levels makes the transition from the ground to excited electron state different from the inverse transition.

Among the properties desired for scintillators are good efficiency and linearity for detecting charged particles of different energies, transparency to its own light emission wavelengths, a light output spectrum near that of the photomultiplier tube used with it and a short decay time for the scintillation. Organic plastic scintillators have properties quite compatible with those listed.

The timing detectors MT, IT, and BT; the position hodoscopes MP, FP, and BP; the neutron arrays LN and RN; and the in-beam veto IV in figure 7 and table 6 are scintillating detectors.

2.4.4 Čerenkov Detectors

When a charged particle passes through an optically transparent or translucent medium at a speed greater than that of the speed of light in the medium, that is when $v_{\text{particle}} > \frac{c}{n}$ or $\beta > \frac{1}{n}$ where n is the index of refraction of the medium and $\beta = \frac{v}{c}$, an electromagnetic shock wave is produced (this is analogous to the sonic shock wave produced in air when an object travels faster than the speed of sound in air). The light is emitted in a continuous spectrum of frequencies and is linearly polarized. A conical coherent wavefront is produced at an angle, relative to the trajectory of the charged particle, given by the relation $\cos\theta = \frac{1}{\beta n}$. Generally, there are two methods used in nuclear and particle physics which exploit Čerenkov radiation for identification of particles. One method uses the relation $\cos\,\theta = \frac{1}{\beta n}$ to determine the velocity of the charged particles and such

devices are called differential Čerenkov counters. The other method relies on the threshold condition $\beta > \frac{1}{n}$ and are consequently called threshold Čerenkov counters. The latter type of detectors are used in BNL Experiments 813 and 836.

In figure 7 and table 6, IC, FC, BC and BCL are threshold Čerenkov detectors. The first three Čerenkov detectors use silica aerogel which can be manufactured with a very low index of refraction (slightly above one) which is required for thresholds close to the speed of light in vacuum. Silica aerogel also has a very low density ($\sim$0.2 g/cm^3) which helps in keeping multiple scattering to a minimum.

2.4.5 Photomultiplier Tubes

The photomultiplier tube is an indispensible piece of equipment in nuclear and particle physics experiments. It makes possible the detection of the light emitting interactions of certain materials with radiation: interactions that release only a very small amount of light. Photomultiplier tubes (PMTs) detect the light produced converting it into an electronic signal and amplifying that tiny signal tremendously into a convenient size.

A schematic of a PMT is shown in figure 10. It is a linear focussing type which has better linearity than other types of PMT construction and is the most widely used in experimental nuclear and particle physics. Its essential features are the photocathode where incident photons cause the release of electrons, the dynodes where the electronic signal is amplified and the anode where the signal is collected and made available for output. Briefly, the operation of the PMT is as follows: An incoming photon strikes the photocathode where it releases a photoelectron which is then accelerated towards the first dynode held at a higher potential than the photocathode; upon striking the first dynode the photoelec-

tron causes the release of several secondary electrons which then are accelerated to the second dynode held at a higher potential than the first; these electrons, in turn, cause the release of more secondary electrons upon striking the second dynode. This process of electron multiplication continues on down the chain of dynodes, each held at a progressively higher potential, and the current is finally collected at the end of the chain at the anode. Typical gains of PMTs used in experimental nuclear and particle physics are $\approx 10^6 - 10^8$.

The photocathode releases electrons from light quanta via the photoelectric effect. It is composed of a semi-transparent thin film of material with a low work function. Typically, the quantum efficiency (*i.e.* number of released electrons / number of incident photons) of the photocathode is $\lesssim 30\%$ and is wavelength dependent. Dynode materials are chosen to have a high secondary emission factor and a secondary emission factor which is stable at high rates.

A typical voltage divider used to operate PMTs is shown in figure 10. Capacitors or zener diodes are frequently used in the last few dynode stages in order to maintain a steady inter-dynode potential difference when large currents flow through them. The sample voltage divider circuit in figure 10 employs capacitors between the last four dynode stages for this purpose.

Transit times for the electrons through the PMT dynodes, while dependent on the applied voltage, are typically in the tens of nanoseconds and time jitter, dependent mainly upon where a photon strikes the photocathode, is typically 1–3 ns.

2.4.6 A Few Details About the Detectors

A few of the parameters describing the detectors are given in tables 7, 8 and 9. The coordinate system defined for this experiment is as follows: the z-axis follows along the beam direction in the beamline, the y-axis points directly

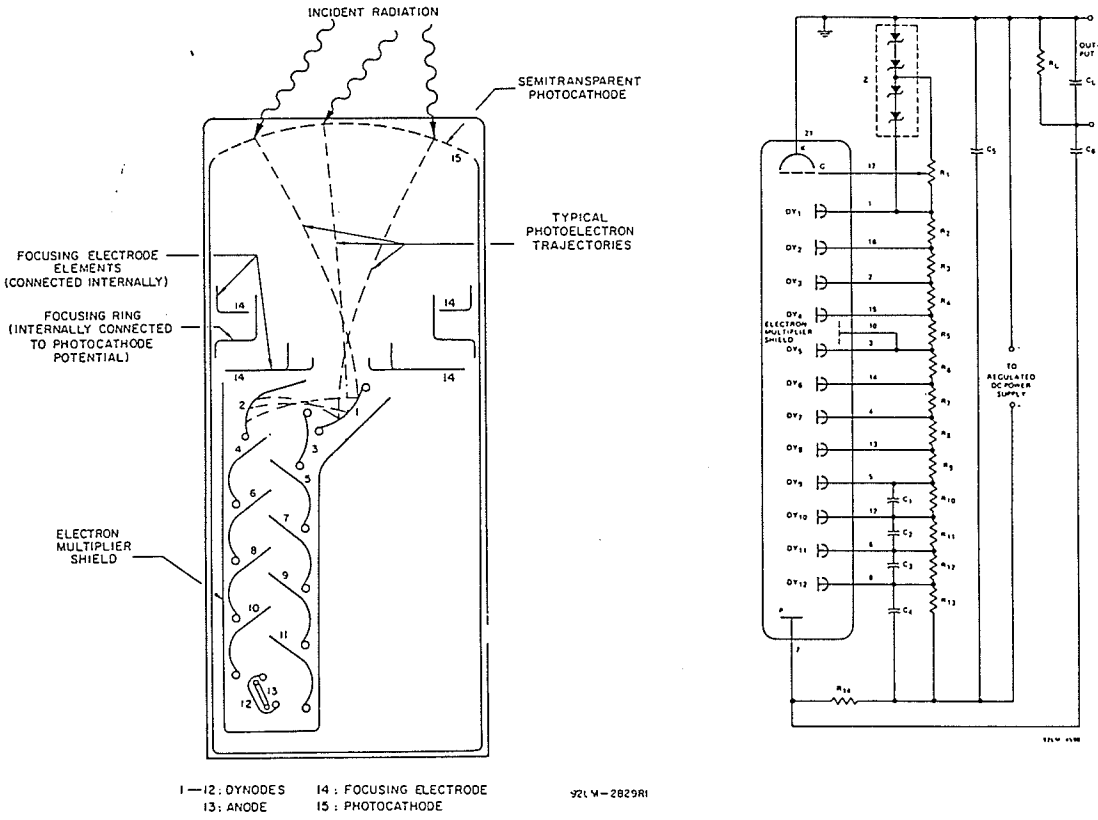

Figure 10: *Cross-sectional view of a RCA 8575 photomultiplier tube and a typical voltage divider for its operation*

vertical and is perpendicular to the z-axis, and the x-axis points horizontally to the right when viewed from upstream of the beam and is also perpendicular to the z-axis. The origin is located at the experimental target centre.

The in-beam particle tracking and identification equipment are all the detectors upstream of the experimental target; everything from the drift chamber MD1, between the separators, to the incident threshold Čerenkov just before the LH_2/LD_2 target in figure 7. Incoming particles are tracked through the dipole D3 to determine their momentum. The mass slit (MD1) and incident (ID1,2,3) drift chambers, along with the mass hodoscope (MP) do this. The mass position scintillating detector MP is made up of 72 - 6 mm wide overlapping scintillators designed in such a manner as to give a position resolution to within 2.3 mm. Particle identification is accomplished with a combination of the incident Čerenkov (IC) and mass (MT) and incident (IT) timing scintillation detectors.

The K^+ spectrometer is made up of everything downstream of the experimental target. It is a non-focusing spectrometer built around a modified 48D48 dipole magnet which has a gap large enough to allow the noninteracting part of the 1.8 GeV/c K^- beam to pass through without striking the magnet yoke in addition to deflecting the beam away from the outgoing K^+. Drift chambers upstream (FD1,2), downstream (BD1,2) and one in the magnet gap itself (FD3) provide a momentum resolution of $\sim$0.5% for the spectrometer. Position hodoscopes (FP,BP) provide information to reject multiple charged particle events such as the quasi-free Ξ^- production reaction $K^- + {}^3\mathrm{He} \rightarrow K^+ + \Xi^- + p + n$ in Experiment 836. Threshold Čerenkov detectors are used for particle identification: the forward Čerenkov (FC) and back Čerenkov (BC) detectors which distinguish the K^+ from the π^+ and μ^+ that result from the decay of K^+ created in the target that do not make it through the whole spectrometer and the back Lucite Čerenkov which distinguish the K^+ from protons. Finally, the back time of

Table 7: *Various drift chamber data.*

	Chamber Centre [cm]			Chamber Angles[a] [°]			width	height	# of	wires per	wire spacing	plane wire angles	resolution
	c_x	c_y	c_z	c_α	c_β	c_γ	[cm]	[cm]	planes	plane	[cm]	[°]	[μm]
MD1	0	0	-420.0	0	0	0	11.9	11.9	2	32	0.952	0.0, 90.0	150
ID1	0	0	-135.12	0	0	0	12.2	10.6	3	48	0.508	120.0, 60.0, 0.0	150
ID2	0	0	-108.63	0	0	0	12.2	10.6	3	48	0.508	120.0, 60.0, 0.0	150
ID3	0	0	-82.93	0	0	0	12.2	10.6	3	48	0.508	120.0, 60.0, 0.0	150
FD1	0	-6.8	30.06	0	0	0	24.4	21.2	3	96	0.508	210.0, 150.0, 90.0	150
FD2	0	-6.8	66.80	0	0	0	24.4	21.2	3	96	0.508	210.0, 150.0, 90.0	150
FD3	0.17	-3.62	149.4	0	0.13	0	45.7	81.3	4	64	1.27	150.0, 90.0, 90.0, 30.0	300
BD1	0.010	68.26	372.72	30.105	-0.076	0.0085	114.0	214.0	3	112,128	2.00	90.01, 119.97, 59.99	300
BD2	0.014	69.08	455.35	30.039	-0.071	0.0229	114.0	214.0	4	112,128	2.00	119.99, 59.99, 89.98	300

[a] c_α is the angle of the chamber planes to the vertical, c_β is the angle between the chamber planes and the x-axis, and c_γ is the angle of rotation of the chamber planes about their normal lines perpendicular to the planes

[b] angle relative to vertical axis along wire planes

Table 8: *Composition of the Čerenkov detectors.*

	Material	n^a	Dimensions[b] [cm^3]	Centre Position x	y	z [cm]	$\beta_{\text{threshold}}$[c]	Momentum Thresholds $p_{\pi^\pm}$ [GeV/c]	$p_{K^\pm}$ [GeV/c]	$p_{\mathrm{p},\bar{\mathrm{p}}}$ [GeV/c]
IC1	aerogel	1.03	15×5×6	0	0	-128	0.971	0.566	2.00	3.80
IC2	aerogel	1.03	15×5×6	0	0	-101	"	"	"	"
FC	aerogel	1.04	25×25×9	0	0	47	0.962	0.489	1.73	3.28
BC	aerogel	1.04	120×190×9	0	73	472	"	"	"	"
BCL	lucite (acrylic)	∼1.5	140×210×1	0	130	590	0.666	differential type		

[a] Index of refraction
[b] Active area ×thickness
[c] radiating threshold velocity as a fraction of c

Table 9: *Various data for scintillation counters.*

	Centre Position[a]			vertical	element	# of	Active	Element
	x	y	z	angle	angle	elements	Area	Size
	[cm]			[°]	[°]		[cm^2]	[cm^3]
MP	0.0	0.0	-440.0	0.0	0.0	72	33.3×1.3	0.7×1.3 ×0.3
MT	0.0	0.0	-430.0	0.0	0.0	9	33.1×1.5	3.7×1.5 ×0.6
IT	0.0	0.0	-72.4	0.0	0.0	4	10.0×3.0	2.5×3.0 ×1.3
FP	0.0	0.0	60.0	0.0	90.0	16	24.0×24.0	24.0×1.5 ×0.4
BP	0.0	101.0	527.0	30.0	0.0	6	120 ×180	21.0×180.0 ×0.95
BT	0.0	210.3	737.0	15.0	90.0	40	200 ×320	200.0×8.5 ×5.0
RN	97.2	0.0	-34.3	0.0	0.0	50	158 ×183	182.8×15.2 ×5.1
LN	-103.5	0.0	-31.8	0.0	0.0	50	158 ×183	182.8×15.2 ×5.1

[a]for RN and LN the x coordinate refers to the position of the front face of the detector.

flight array (BT) also serves as a particle identification detector and provides a desired level of redundancy which is particularly needed in Experiment 836.

3 Time-of-Flight Scintillation Detectors

The next few sections will briefly describe some aspects of time-of-flight scintillating detectors and, in particular, how they relate to the kaon and neutron time-of-flight detectors in the H particle search. The following points should be kept in mind: As noted above, the K^+ TOF hodoscope wall is an integral part of the K^+ spectrometer downstream of the target. Along with the back Čerenkov detector its purpose is to distinguish the K^+ from the other single positively charged particles of the same momentum, especially the π^+ that are expected to be slightly too slow to fire the back Čerenkov. The momenta of the particles are determined by the kaon spectrometer — specifically, the combination of forward drift chambers, 48D48 dipole magnet and back drift chambers. The expected momentum resolution is $\sim 0.5\%$ FWHM with this combination of chambers and magnet. Thus with the momenta of charged particles determined with other apparatus the main purpose of the K^+ TOF hodoscope wall is particle identification.

3.1 Charged Particle TOF Detectors for Particle Identification

The TOF method for particle identification is based on the fact that particles with the same momenta but different masses will have different velocities. By measuring the velocity of particles of known momenta their masses can be determined. In practice, the time-of-flight of the particles are measured for a fixed distance from which the velocity may be easily determined. The relationship between mass and time-of-flight is as follows: For a particle with known momentum p and a measured time-of-flight of τ over a distance d, the rest mass of

the particle is

$$m = \frac{p}{c}\sqrt{\frac{\tau^2 c^2}{d^2} - 1},$$

where c = speed of light in vacuum. (This is simply derived by rearranging the familiar equation for momentum, $p = \gamma m v$.) It then follows that the TOF difference between two particles, one with mass m_1 and the other with mass m_2, with the same momentum over a distance d is

$$\begin{aligned} \tau_1 - \tau_2 &= \frac{d}{c}\left[\sqrt{1 + \frac{m_1^2 c^2}{p^2}} - \sqrt{1 + \frac{m_2^2 c^2}{p^2}}\right] \\ &\simeq \frac{dc}{2p^2}\left(m_1^2 - m_2^2\right), \quad \text{for } p \gg m_{1,2}c \text{ to first order.} \end{aligned}$$

Plots of the TOF difference per unit path length versus momentum for π-K and p-K are shown in figure 11.

The extent to which particle identification with time-of-flight scintillators can be a useful tool is limited by the finite time resolution of real detectors. If the detector resolution measurement uncertainty of $\tau_1 - \tau_2$ is $\sigma_{\tau_1-\tau_2}$ then the maximum momentum at which the two massive particles can be distinguished is

$$p_{max} \simeq \sqrt{\frac{dc}{2\sigma_{\tau_1-\tau_2}}(m_1^2 - m_2^2)}. \tag{1}$$

For example, the maximum momentum at which π-K separation is possible over a 7 meter flight path for a very good timing resolution of $\sigma_{\tau_1-\tau_2} = 100$ ps is $\sim$ 5.1 GeV/c. The 2σ, 3σ, and 4σ π-K maximum momentum separation, p_{max} , are $\sim$ 3.6 GeV/c, $\sim$ 2.9 GeV/c, and $\sim$ 2.6 GeV/c respectively. These numbers would seem to indicate that time-of-flight by itself would satisfy the background rejection level of 10^{-4} required for the current search for the H particle since the the 4σ maximum momentum π-K separation is well above 2 GeV/c. However, experience has shown that beyond about 3σ from its peak the time-of-flight resolution function deviates significantly from a Gaussian distribution.

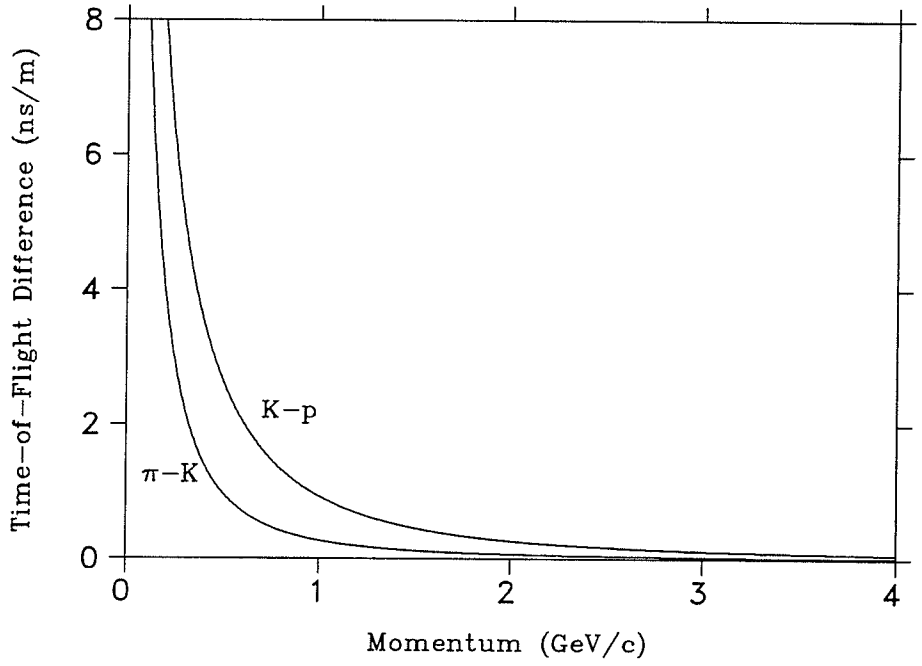

Figure 11: *Time of flight difference per metre of path length versus momentum for π-K and p-K.*

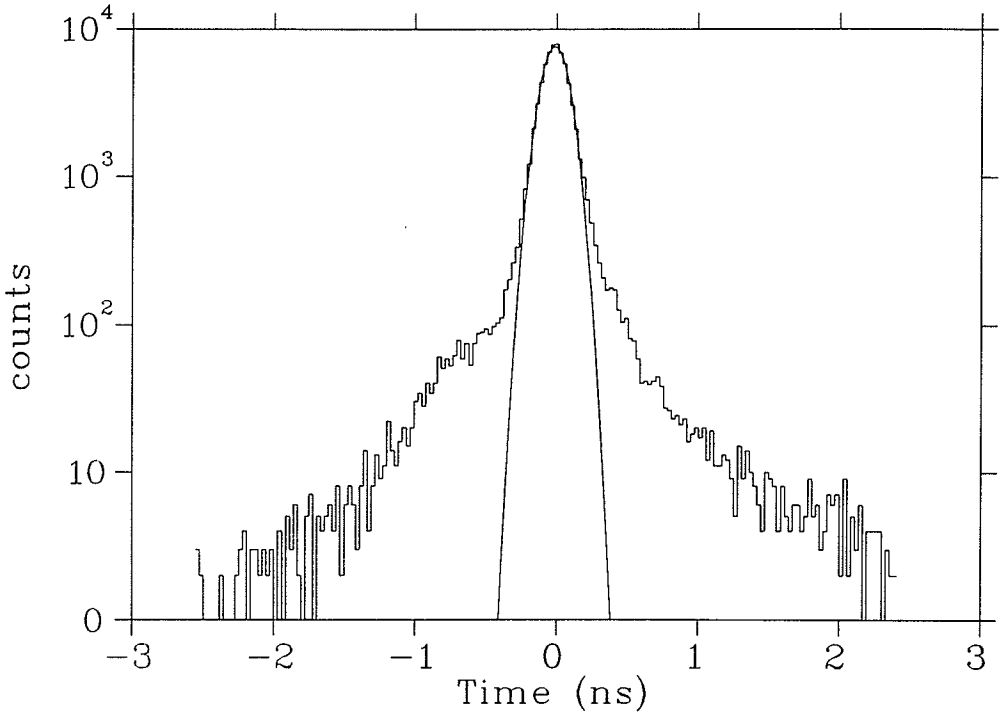

Figure 12: *Typical time of flight spectrum between two high quality in-beam timing scintillators as measured in AGS Experiment 788.*

Figure 12 shows the TOF spectrum between two high quality in-beam time-of-flight scintillators for a pion beam obtained from BNL Experiment 788 and it indicates that there is a low level process, more complicated than the simple statistical fluctuations of the photomultiplier tubes and electronics occurring. This behavior limits the identification power of this type of detector. Thus the required background rejection level of 10^{-4} for the experiments cannot be met by time-of-flight alone; hence, the employment of the back Čerenkov detector.

3.2 Neutron TOF Detectors

Neutron time-of-flight detectors serve two purposes similar to those of charged particle identification time-of-flight detectors though they differ in their application. Firstly, the neutron time-of-flight detectors must detect the neutrons. This is not as simple a matter as detecting charged particles. Secondly, the neutron time-of-flight detector is used to determine the velocity and hence energy of the neutron as opposed to using time-of-flight for particle identification where the momentum of the charged particle is known. The mechanism by which neutrons are detected is different from that of charged-particle detection. Due to its lack of charge there is no ionization by the neutron itself. Neutron detection relies upon the detection of the secondary charged particles produced in interactions of the neutron. In organic plastic scintillators, which are just hydrocarbon compounds, neutrons are detected through interactions such as $n-p$ elastic scattering in which the recoiling proton causes the scintillation, (n, np) scattering on carbon and in inelastic $n - C$ scattering $(n + C \rightarrow n + C + \gamma)$ where the photon may be detected by Compton scattering off electrons, among others (more details will be given in a later section). In contrast to charged-particles, where the detection efficiency of scintillators is virtually 100% as long as the charged-particle passes through the scintillator thereby causing ionization in the scintillator, neutrons are not so readily detected since they do not directly ionize. A rough value for the detection efficiency of energetic (> few MeV) neutrons in ordinary scintillator is <2% per centimetre traversed.

Neutron time-of-flight detectors serve both to detect neutrons and determine their energy. The kinetic energy, T, of a particle is simply the difference between the total energy $(E = \gamma mc^2)$ and its rest energy $(E_0 = mc^2)$: $T = (\gamma - 1)mc^2$, where $\gamma = [1 - \beta^2]^{-\frac{1}{2}}$, $\beta = \frac{v}{c}$, v is the particle velocity, and c is the speed of light in vacuum. For a time-of-flight τ over a distance d,

$T = \{[1 - \frac{d^2}{c^2\tau^2}]^{-\frac{1}{2}} - 1\}mc^2$. If τ and d are statistically independent then the error in kinetic energy (σ_T) is related to the error in τ (σ_τ) and the error in d (σ_d) by:

$$\sigma_T^2 = \left(\frac{\partial T}{\partial \tau}\right)^2 \sigma_\tau^2 + \left(\frac{\partial T}{\partial d}\right)^2 \sigma_d^2 \quad (2)$$

$$= (\gamma^3\beta^2 mc^2)^2 \left[\frac{\sigma_\tau^2}{\tau^2} + \frac{\sigma_d^2}{d^2}\right] \quad (3)$$

Therefore,

$$\begin{aligned} \sigma_T &= \gamma^3\beta^2 E_0 \sqrt{\frac{\sigma_\tau^2}{\tau^2} + \frac{\sigma_d^2}{d^2}} \\ &= \frac{\beta^2}{1-\beta^2}[E_0 + T]\sqrt{\frac{\sigma_\tau^2}{\tau^2} + \frac{\sigma_d^2}{d^2}} \\ &= \frac{T(T+E_0)(T+2E_0)}{E_0^2}\sqrt{\frac{\sigma_\tau^2}{\tau^2} + \frac{\sigma_d^2}{d^2}}. \end{aligned} \quad (4)$$

As the last equation demonstrates, the energy resolution varies as the cube of the energy that is determined by time of flight. However, for $T \ll E_0$ as is the case for the neutrons in Experiment 813 ($6 < T < 100$ MeV)

$$\begin{aligned} \sigma_T &= 2T(1 + \frac{T}{E_0})(1 + \frac{T}{2E_0})\sqrt{\frac{\sigma_\tau^2}{\tau^2} + \frac{\sigma_d^2}{d^2}} \\ &\simeq 2T\sqrt{\frac{\sigma_\tau^2}{\tau^2} + \frac{\sigma_d^2}{d^2}}, \quad T \ll E_0. \end{aligned} \quad (5)$$

3.3 Practical Aspects of Scintillating TOF detectors

Scintillating time-of-flight detectors can be divided into two general types: in-beam and out-of-beam. As appropriately described by their names in-beam detectors are physically located to intersect the beam before it hits an experimental target and thus are usually small in size, while out-of-beam detectors are usually physically outside of the beam and are used to detect reaction products escaping from the target. These may cover a large solid angle and, in order to

have a reasonable flight length to the detector, out-of-beam detectors tend to be relatively large. Generally, both types are composed of arrays of identical, independent modules that are placed side by side with adjacent modules overlapping a small amount so that there are no cracks which particles may pass through without traversing the active part of the detector. Also, the modules are viewed by two photomultiplier tubes, one at each end in order to produce reliable timing information since the timing deduced at each end is dependent upon the position at which the light is produced in the scintillator. The light from the scintillator, owing to the usual geometry of the end of the scintillator not being the correct shape or size to effectively couple to the photomultiplier tube, is transmitted from the end of the scintillator to the photomultiplier tube via a light guide. The next section will briefly discuss light guides and will be followed by a brief discussion on timing. Organic plastic scintillators were discussed earlier (Section 2.4.3).

3.4 Light Guides

Light guides or light pipes are usually made from optically transparent acrylic plastic which may be machined and polished quite readily. The index of refraction of acrylic plastic is 1.51–1.54 which is suitably close to that of plastic scintillators (generally ~1.58) so as to allow almost all of the scintillation light to pass through the interface when the light guide is optically glued to the scintillator. (The optical cement used to glue the two also has an index of refraction close to that of plastic scintillator). This material may also be bent and twisted into a great number of shapes when it is heated until soft. To optically couple a wide and thin scintillator of rectangular cross-section to the circular cross-section of a photomultiplier tube face a geometric transformation along the light guide must occur. This is accomplished either by *(i)* a bi-wedge shaped

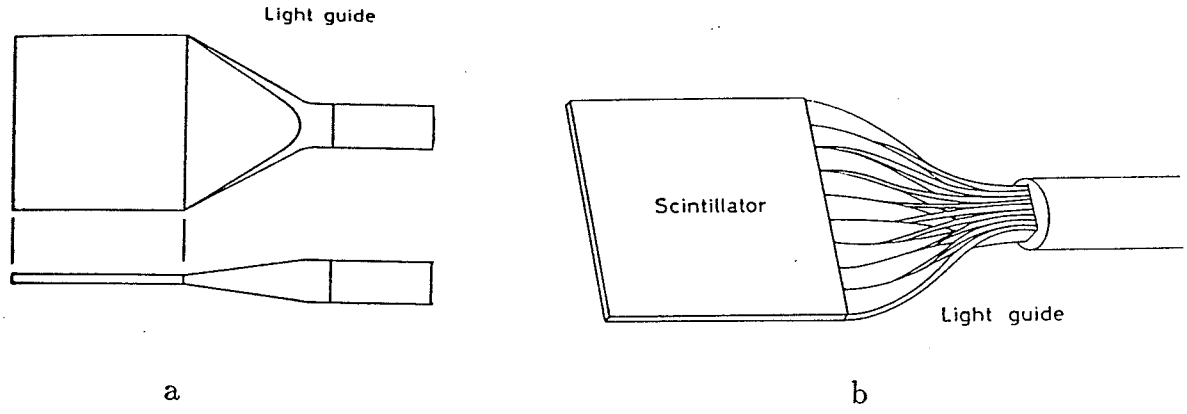

Figure 13: *(a) Fish-tail type light guide. (b) Twisted-strip light guide.*

frustum in which the corners of the scintillator end are translated into a regular cross-section which is connected to the photomultiplier tube or by *(ii)* a number of strips of rectangular cross-section which cover the end of the scintillator and are twisted and positioned so as to form a square cross-section when stacked together at the other end of the strips. The former is commonly referred to as a fish-tail type of light guide; the latter a twisted-strip light guide. Figure 13 shows samples of both types of devices.

For light collection efficiency, the cross-sectional area of the optically coupled scintillator end should be less than or equal to size of the sensitive area of the photomultiplier tube and the area transformation of the light guide from the scintillator to the photomultiplier tube should be of constant cross-section all along the length of the light guide. This would ensure that most of the light travelling through the device is collected by the photomultiplier tube. The second criterion above is due to Garwin [33] who showed that uncollimated light travelling through a light guide cannot be concentrated into a smaller area at its

output. If the entrance area of the light guide were A_i and the output area A_o with $A_o \leq A_i$ then, at most, $\frac{A_o}{A_i}$ of the light would exit the light guide. The best light conductance that can be achieved is with light guides of constant cross-sectional area. Such light guides are called adiabatic. However, if the twists in the strips are too severe light will be lost through the sides of the strips. Massam [34] showed this through modelling the light collection process through twisted strips: To retain 95% light transmission any bends in the light guide should have a bending radius no less than eight times the thickness of the strip. In situations where the twisted strips are all the same length, which is important for timing applications, the light guide is called isochronous.

Light collection can be improved with the use of certain light collection cones. For instance, the Winston cone [35] can select light up to a designed maximum angle relative to the optical axis to enter the photomultiplier tube. Its shape, length and exit radius are uniquely determined by the radius of the photocathode and the desired maximum angle at which light is selected.

3.5 Timing of TOF Detectors

Out-of-beam TOF detectors are typically arrays of relatively long and narrow scintillation counters viewed by a PMT at each end to reduce timing uncertainties and to give coarse position resolution. Position along the length of the bar may be determined by the time difference between the PMT signals at each end of the bar as discussed later. The output from each PMT is usually split, resistively, into two branches with one branch input to an analog to digital converter and the other branch connected through a discriminator to the STOP input of a time to digital converter. The analog to digital converter (ADC) measures the size of the signal by charge integration while the time to digital converter (TDC) measures the time difference between two signals — START and STOP

signals.

The START signal of the TOF TDC is typically from a detector upstream of the target in the beam. The timing of charged particles in the beam can be easily deduced by having two or more timing detectors upstream of the target where the time-of-flight over a known distance for the same particle can be measured. The timing of outgoing charged particles and neutrons from reactions in the experimental target is more involved since the beam charged particles determine the start signal and different reaction product particles provides the stop signal. In the case of outgoing charged particles, a series of two out-of-beam timing detectors may be used to determine time-of-flight from their time difference. This will not work for neutrons, however, due to both its low detection probability and high scattering probability when it does interact. But by collecting the appropriate data, the vertex timing and position information of the reaction may be calculated and hence the time-of-flight and flight lengths may be derived for both neutrons and charged particles.

3.6 Discriminators

In order to derive precise timing information from PMTs the raw signals from the PMT anodes must be converted into logic pulses and this is done with discriminators. In timing applications, the type of discriminator used can have a great influence on the results achieved. Discriminators select appropriate analog detector signals and generate logic pulses if the detector signal exceeds a threshold voltage.

There are two types of discriminators that are widely used in nuclear and particle physics; leading edge and constant fraction. Leading edge discriminators are the simplest type. Logic pulses are derived from the time that input pulses cross a threshold level. For analog pulses of nearly constant risetime and

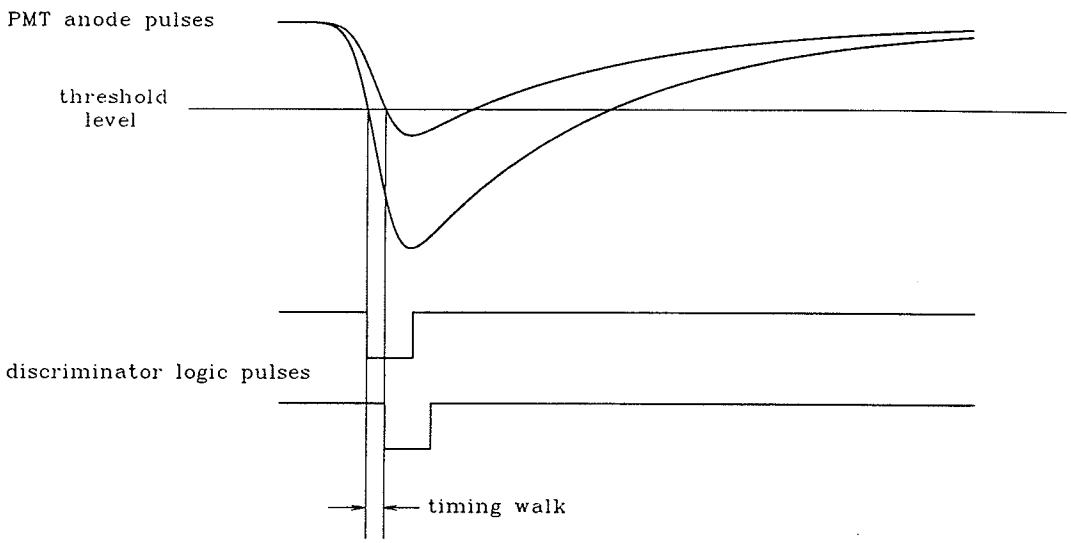

Figure 14: *Walk induced in the logic signal of a leading edge discriminator by pulses of different amplitudes.*

amplitude the walk of the logic pulses will be small; however, if the input pulses have even a moderate dynamic range a large walk effect would be induced (Figure 14). Fortunately, the walk can be corrected for as described by Braunschweig *et al* [36] by fitting the time walk of a TOF PMT signal to the relation

$$t - t_0 = W\left(\frac{1}{\sqrt{a_0}} - \frac{1}{\sqrt{a}}\right)$$

where $t - t_0$ is the time walk of a signal of pulse height a, a_0 is some reference pulse height and W is a constant fitted to the TOF walk distribution of the equation.

Constant fraction discriminators, in contrast, provide timing logic signals of very little walk for analog pulses of constant risetime and wide dynamic range. This is accomplished by deriving the logic signal from the point when the analog signal reaches a certain constant fraction of its maximum amplitude. Figure 15 illustrates the signal processing of a constant fraction discriminator. The input signal is split in two and then processed such that an attenuated signal of the

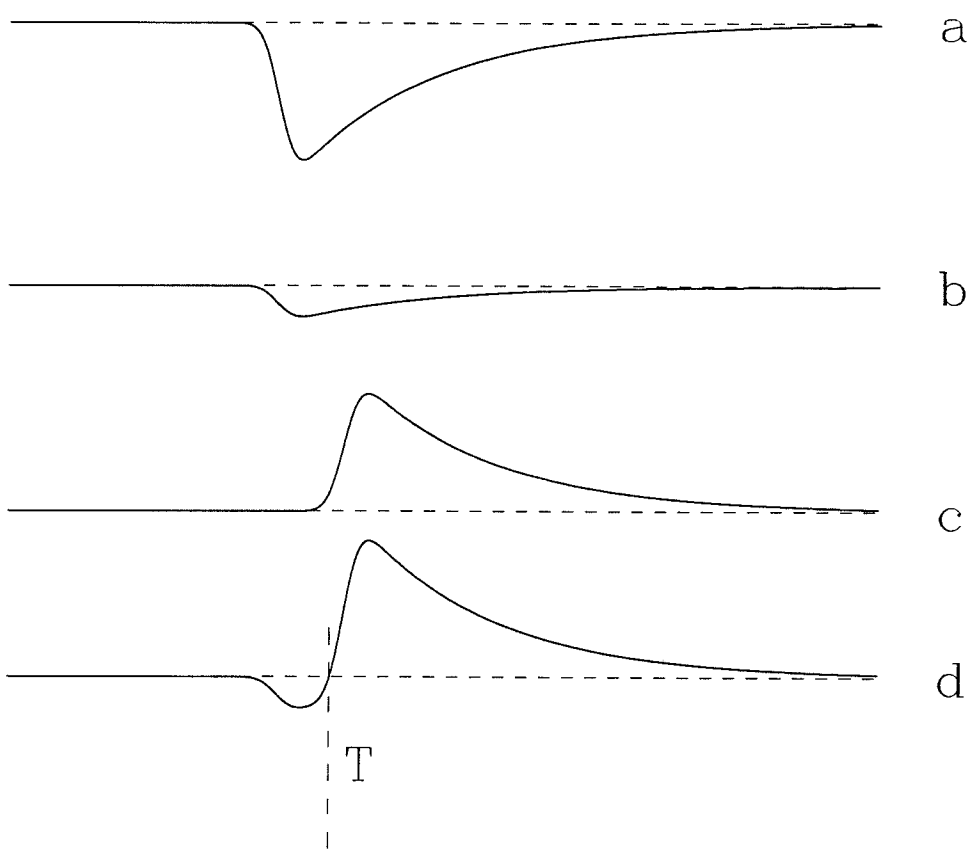

Figure 15: *Sketch of the operation of a constant fraction discriminator: (a) the original PMT anode signal, (b) attenuated signal, (c) inverted and delayed signal, (d) the bipolar signal from the sum of b and c. The logic pulse is derived from the zero-crossing time T.*

original is added to an inverted delayed input signal with delay larger than the risetime of the original signal. The zero-crossing of the resulting bipolar pulse then occurs at a constant fraction of the input pulse height.

In addition to walk, a factor that affects the timing of discriminators is jitter which is caused by the electronic noise or statistical fluctuations in the formation of the signal in the detector. It would show up as small fluctuating deviations added to the PMT signals in figures 14 and 15. Jitter affects both

types of discriminators.

3.7 Timing Resolution for TOF Scintillation Counters

Consider the arrangement of TOF counters shown in Figure 16. Suppose that the timing uncertainty in the TOF start module is zero. If the TOF stop is derived from a scintillator bar of length L, the effective velocity of light in the scintillator bar is c_{eff}, and the true time of flight of the particle is τ then the TDC stop times from PMTs A and B are

$$T_A = \tau + \frac{\frac{L}{2} + x}{c_{eff}} + \varepsilon_A \quad \text{and} \tag{6}$$

$$T_B = \tau + \frac{\frac{L}{2} - x}{c_{eff}} + \varepsilon_B \tag{7}$$

where $\varepsilon_{A,B}$ are quantities that include the transit times of the PMT, jitter, etc. and contain all the uncertainty of $T_{A,B}$. As evident from equations 6 and 7, $T_{A,B}$ are functions of the position along the bar where the particle passes through. If the average of $T_{A,B}$ is taken for the stop time then the position dependence disappears.

$$T_{stop} = \frac{1}{2}(T_A + T_B) \tag{8}$$

$$= \tau + \frac{1}{2}\left(\frac{L}{c_{eff}} + \varepsilon_A + \varepsilon_B\right). \tag{9}$$

The second term on the right-hand side of equation 9 is the time of flight offset and must be determined experimentally. Also the uncertainty in T_{stop} is less than the uncertainty in T_A or T_B alone. The uncertainties σ_{ε_A} and σ_{ε_B} are statistically independent since PMTs A and B are independent:

$$\sigma_{T_A} = \sigma_{\varepsilon_A}, \quad \sigma_{T_B} = \sigma_{\varepsilon_B}$$

$$\sigma_{T_{stop}} = \frac{1}{2}\sqrt{\sigma_{\varepsilon_A}^2 + \sigma_{\varepsilon_B}^2}. \tag{10}$$

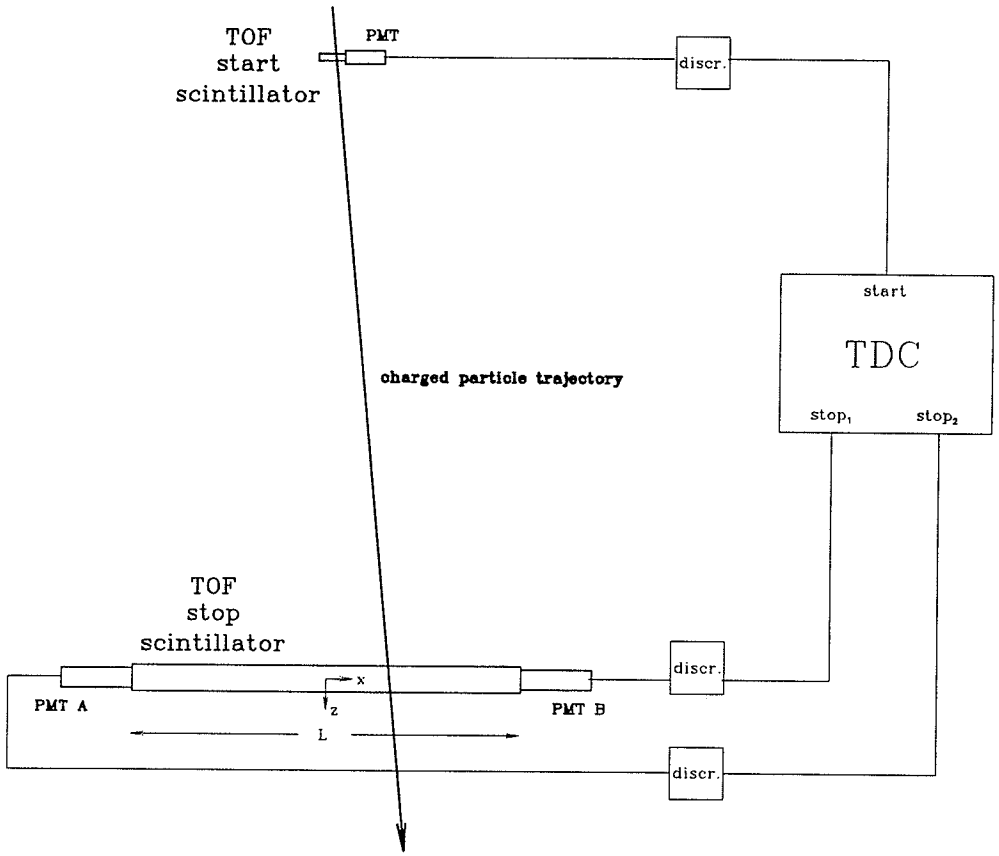

Figure 16: *Simplified set up for charged particle time-of-flight measurements using scintillating detectors. For simplicity, the time-of-flight start counter is drawn with only one photomultiplier tube viewing it and the same charged particle starts and stops the TDC.*

Call this the intrinsic stop resolution of the scintillator module, $\sigma_{T_{stop}} = \sigma_{stop}^{intrinsic}$. If we assume the PMTs A and B have similar timing uncertainty, $\sigma_{\varepsilon_A} \simeq \sigma_{\varepsilon_B}$, then $\sigma_{t_{stop}} \simeq \frac{1}{\sqrt{2}}\sigma_{\varepsilon_A}$; *i.e.* the error in the time average stop signal is $\frac{1}{\sqrt{2}}$ that of the error from signal in each single PMT.

Now, suppose that the timing uncertainty in the TOF start module is $\varepsilon_{start} = \varepsilon_0$. Then if $t_{A,B}$ are the stop times from PMTs A and B in this case:

$$t_A = T_A - \varepsilon_0 \quad \text{and} \tag{11}$$

$$t_B = T_B - \varepsilon_0 \tag{12}$$

and

$$t_{stop} = \frac{1}{2}(t_A + t_B) \tag{13}$$

$$= T_{stop} - \varepsilon_0 \tag{14}$$

$$= \tau + \frac{1}{2}\left(\frac{L}{c_{eff}} + \varepsilon_A + \varepsilon_B\right) - \varepsilon_0. \tag{15}$$

Hence,

$$\sigma_{t_{stop}} = \sqrt{(\sigma_{stop}^{intrinsic})^2 + \sigma_{start}^2} \tag{16}$$

$$= \sqrt{\frac{1}{4}(\sigma_{\varepsilon_A}^2 + \sigma_{\varepsilon_B}^2) + \sigma_{\varepsilon_0}^2}. \tag{17}$$

That is, for actual time of flight measurements, the resolution of the time of flight stop time measured includes a contribution from the timing uncertainty of the start counter. It is important to take both the start time resolution and the stop time resolution into account as the overall time resolution depends on both.

Consider the timing difference between PMTs A and B:

$$t_{diff} = t_A - t_B = T_A - T_B = \frac{2x}{c_{eff}} + \varepsilon_A - \varepsilon_B \tag{18}$$

which gives

$$\sigma_{t_{diff}} = \sqrt{\sigma_{\varepsilon_A}^2 + \sigma_{\varepsilon_B}^2}. \tag{19}$$

It is evident that $\sigma_{stop}^{intrinsic} = \frac{1}{2}\sigma_{t_{diff}}$.

As mentioned previously, the position along the bar can be determined by the difference between the signals from each end of the bar: Refering to figure 16 the time difference between the arrival of the scintillation light at each end is

$$t_A - t_B = \frac{\frac{L}{2} + x}{c_{eff}} - \frac{\frac{L}{2} - x}{c_{eff}} \quad (20)$$

$$= \frac{2x}{c_{eff}}. \quad (21)$$

The uncertainty in x is then

$$\sigma_x = \frac{c_{eff}}{2}\ \sigma_{t_A - t_B}. \quad (22)$$

3.8 Silicone Rubber Optical Coupling Discs

To ensure that the light lost at the optical coupling between the light guide and the photomultiplier tube is kept to a minimum, an optical coupling material is usually applied as an interface. Traditionally, the material used for this purpose has been optical quality couplant grease. In the recent past, however, optical coupling material made from pliable clear silicone rubber have found favour for this application due to its convenience over grease. This section will discuss the production of the silicone rubber optical coupling discs manufactured to suit the particular requirements for such materials for use in the neutron time of flight modules discussed later.

The desired properties for an optical coupling material include: transparency to the light wavelengths it is to conduct, an index of refraction close to those of the two media which it couples, a surface which wets those media (thus establishing optical contact), and a non-viscous nature so that it remains where it was applied. If the region around the optical joint is not prepared otherwise, optical grease has a tendency to wick through the air gaps between the light opaque wrapping or reflective wrapping, if present, and the light guides and

scintillator thus ruining the total internal reflection along the scintillator and light guides due to the air being around these surfaces. If not applied carefully this can be a major disadvantage in using optical grease.

The attributes that were desired for the silicone rubber optical coupling discs for the current purpose were that they completely couple the 5 cm diameter optical joints in the neutron time of flight modules where they would be used and that they would be reusable. To test whether coupling discs fulfilled the former requirement a light guide blank made of 5 cm diameter plexiglas with both ends exposed so that the optical joint could be viewed and a photomultiplier tube and base assembly used in the neutron arrays were employed. The GHC photomultiplier base assembly, shown in figure 37, had a spring loaded coupling mechanism which applied a relatively small amount of pressure at the photomultiplier tube face to help keep the optical contact at the coupling joint. The optical coupling disc had to be pliable enough to couple the joint under this pressure.

Three different types of silicone products were experimented with to make the discs: they were General Electric RTV 615 silicone rubber, Dow Corning Sylgard 184 silicone rubber, and Dow Corning Sylgard 527 silicone gel. The last product produced material much softer than the first two which were comparable in hardness. All three products come in two component kits with room temperature curing times of 24 hours for Sylgard 527 and about 7 days for the others when mixed as instructed; however, after 24 hours the RTV 615 and Sylgard 184 will have cured sufficiently to allow handling. Shorter curing times could be achieved with elevated temperatures. Some of the properties of the above products are listed in table 10. The RTV 615 compound had previously been used for optical light pipe joints in a barrel calorimeter system [37]. There a 35 to 1 base to curing agent ratio was used with success to make 2" diameter discs 3–6 mm thick. The Sylgard 184 compound was used to make optical joints

Table 10: *Some properties of the silicone products.*

Product	Suggested Mixing Ratio[b]	n^a	Cure Time @ room temp.
RTV 615	10 to 1	1.406	6–7 days
Sylgard 184	10 to 1	1.43	7 days
Sylgard 527	1 to 1	1.407	24 hrs

[a] index of refraction
[b] resin to curing agent or base to hardener

for a calorimeter for BNL Experiment 787 [38]. A base to hardener ratio of 1 to 2 was used.

Three techniques were experimented with to cast the discs. The first technique was similar to that used in reference [37] as the silicone was poured into moulds made by clamping plexiglas sheets of $\frac{1}{16}$" and $\frac{1}{8}$" thicknesses that had 2" holes, machined and polished, onto a $\frac{3}{8}$" thick plexiglas sheet. A thin mylar sheet (0.001" thick) was placed in between the plexiglas plates to facilitate easy removal of the discs. In the second technique, the silicone was cast directly onto the photomultiplier tube face. A mould was created on top of the photomultiplier tube face by attaching a strip of 'invisible' cellophane tape to form a ring around the circumference of the tube that extended from between $\frac{1}{16}$" and $\frac{1}{8}$" beyond the end. The third technique was similar to the second and only differed in that instead of the photomultiplier tube itself a $\frac{3}{8}$" thick plexiglas puck with a ring of 'invisible' cellophane tape around it was used as a mould.

All three products were used to cast samples with the first technique. Mixing ratios varying from between 10 to 1 and 45 to 1 base to curing agent were cast for both RTV 615 and Sylgard 184 and cured at room temperature. Corresponding samples with the same mixing ratio had about the same flexibility and compressibility for the two products. The 10 to 1 ratio samples were quite

hard and not very compressible. When inserted into the coupling tester only a small fraction of the area of the photomultiplier tube face was optically coupled. Samples of 45 to 1 and 40 to 1 ratios were much softer and more flexible than the 10 to 1 ratio samples but were still much too incompressible to achieve complete optical coupling in the GHC test base. Higher base to hardener ratios were not tested as the Sylgard 527 tests showed much more promise for producing a useful optical coupling disc.

Sylgard 527 samples with base to hardener ratios varying through 1 to 1 and 1 to 6 were also cast using the first technique. Samples with ratios greater than approximately 1 to 2 were impossible to remove from the mylar sheets intact and samples with ratios less than approximately 1 to 6 did not solidify completely — probably due to excess hardener. The remaining samples were tested by coupling them in the GHC test base. None completely coupled the photomultiplier tube face but as expected the softer higher ratio samples did couple more area than the harder lower ratio samples.

Attempts to make a suitable disc with the second and third techniques did not fully succeed. All the coupling discs made from casting directly onto the photomultiplier tube face were in fact irremovably bonded to the fused silica of the tube face for the three silicone compounds. In contrast, all of the discs could be removed completely or mostly intact, if done carefully, from the tape and plexiglas puck moulds. As above the RTV 615 and Sylgard 184 compounds were much too incompressible as were the Sylgard 527 samples with base too hardener ratios of less than about 2 to 1; however, Sylgard 527 samples with 1 to 1 and 1 to 1.5 ratios where able to completely optically couple the 2" diameter joint area. Unfortunately, there were two related problems with these discs: they were quite delicate and they were very tacky. A rub across the surface of these discs with a finger resulted in pits being formed. In addition, if Sylgard 527 sample discs of ratios greater than about 1 to 2.5 made in the tape and

plexiglas moulds were left in contact with the photomultiplier tube face for a day or more it would permanently bond with it.

With the previous information, it was apparent that in order to fabricate optical coupling discs that were both effective and reusable from the above silicone products it would be necessary to make them with a tougher, harder outside surface and a softer, easily compressible inner core of Sylgard 527. Such discs were made in the tape and plexiglas moulds by casting three layers of silicone gel or rubber — the first layer (bottom) and the third layer (top) were harder than the second layer (middle). Experiments using RTV 615 to form the outer layers proved to be unsuccessful as such discs when removed from the moulds would curl up significantly with the bottom layer quite plano-convex and the top layer complimentarily plano-concave. Outside layers made from Sylgard 527 produced discs with no such problem.

Silicone optical coupling discs which met the design objectives were produced with Sylgard 527 in tape and plexiglas moulds about $\frac{1}{8}$" thick. The outside layers could be made from ~1 g of the silicone gel with base to hardener ratios between about 1 to 3 and 1 to 4 while the inside layer could be made from ~3.0–3.5 g of silicone gel with base to hardener ratio between about 5 to 4 and 1 to 1. Such discs completely coupled the 2" diameter photomultiplier tube and light guide joint area in the GHC base and could removed and reused if they have not been coupled too long (if coupled for more than a few weeks or months some of the discs bond permanently to the photomultiplier tube face but the silicone gel may be scraped off.) The transmission coefficient as a function of wavelength for a sample disc is shown in figure 17. The transmission curve matches the characteristic light output of plastic scintillators very well as it transmits light of wavelengths into the ultraviolet whereas most plastic scintillators emit light at optical frequencies.

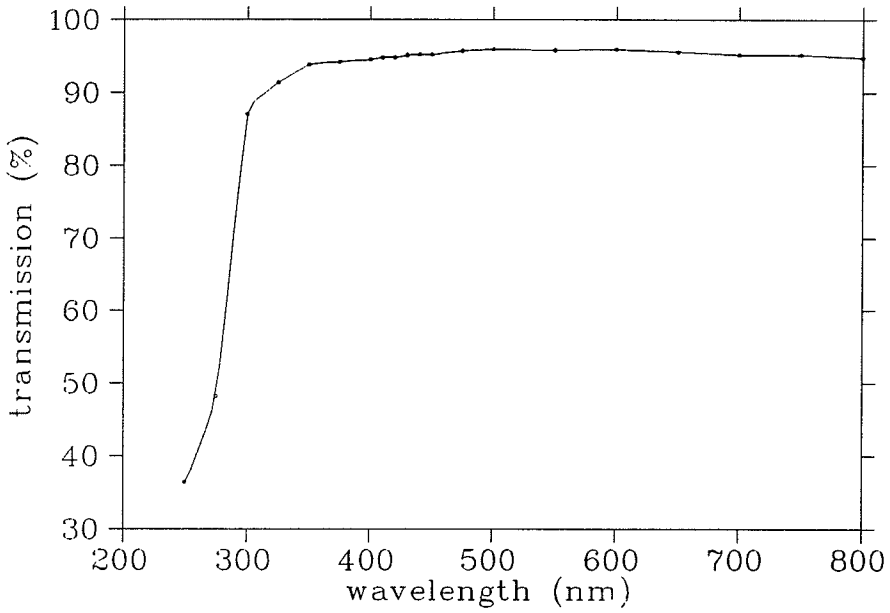

Figure 17: *Wavelength dependence of the transmission coefficient through a silicone gel optical coupling disc sample.*

4 The K^+ Time of Flight Wall

The K^+ time of flight wall stand and the individual scintillator modules were designed in a manner such that it was possible to change the orientation of the entire array relative to the 48D48 spectrometer magnet if the need ever arose. Figure 18 shows possible trajectories out of the magnet for charged particles of varying momentum and vertical scattering angles. The angle of the plane in which the scintillator bars lay could be adjusted so that any future changes could be more easily accommodated.

4.1 Scintillation Counter Modules for K^+ Time of Flight Hodoscope Wall

The individual modules that comprise the K^+ time of flight wall are now described. Each module is made up of a long block of BC-408 plastic scintillator of dimensions $5 \times 8.5 \times 200$ cm^3 with Hamamatsu H1949 photomultiplier tubes viewing through the two ends. The photomultiplier tube at each end was attached to the scintillator by a machined polyvinylchloride (PVC) pipe socket (2" Schedule 40 socket-socket coupling) which was glued directly onto the scintillator. The μ-metal magnetic shield housing of the PMT and voltage divider assembly was inserted into the PVC coupling socket which protruded about 40 mm from the end of the scintillator and held with set screws (see Figure 19). To protect the end of the scintillator a 5 mm thick disc of ultraviolet transmitting (UVT) plexiglass was glued with optical cement onto the scintillator end inside the PVC coupling; the PMT was then optically coupled to this through a silicone rubber disc. The scintillator bars were wrapped in non-reflecting rigid black vinyl and black vinyl electrical tape. Over each scintillator - PVC coupling joint was placed a pre-moulded piece of heat-shrink tubing, shaped to fit snugly

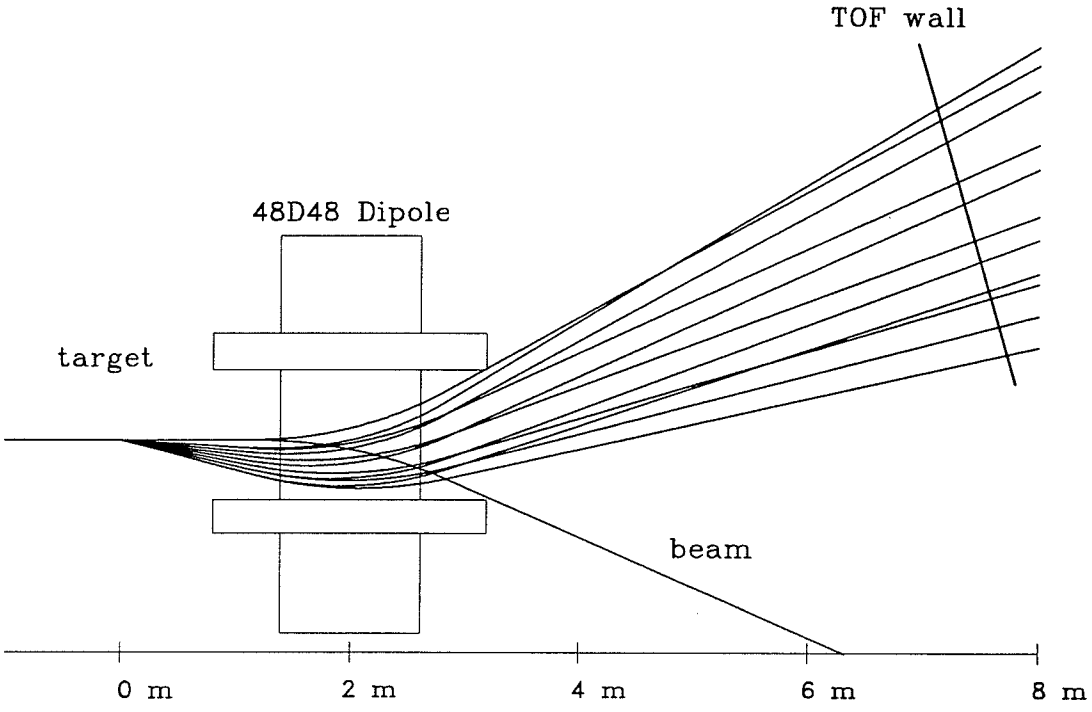

Figure 18: *Simulated trajectories of 1.25 and 1.5 GeV/c positively charged particles through the 48D48 spectrometer dipole.*

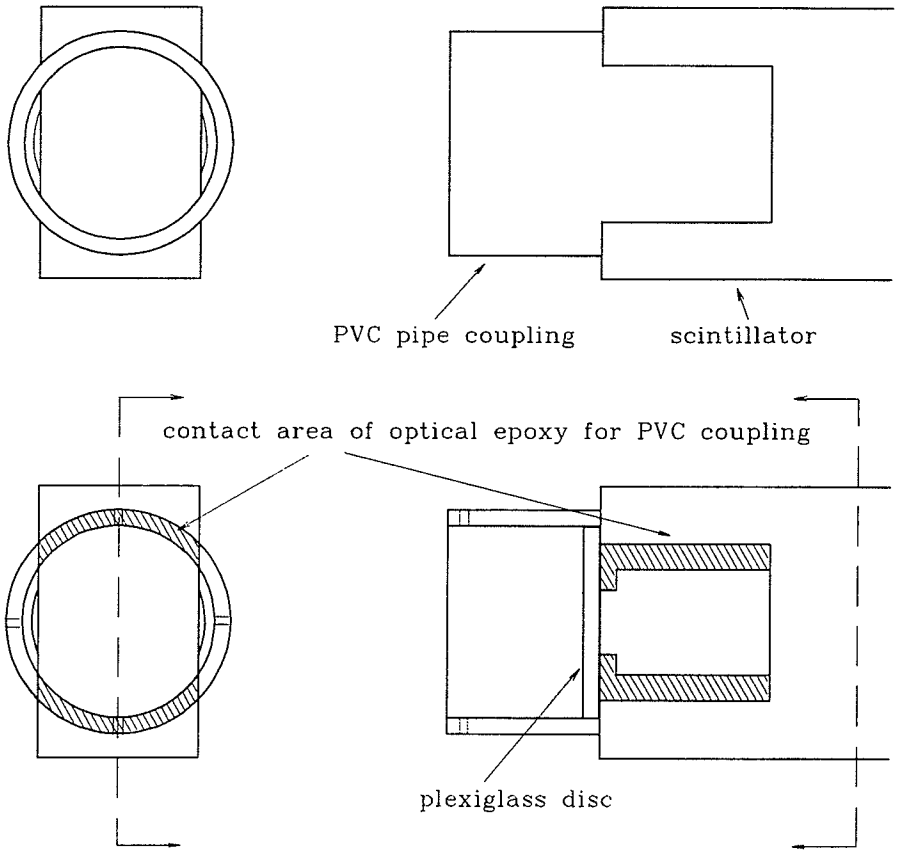

Figure 19: *The photomultiplier tube coupling to the scintillator.*

over most of the PVC coupling and ~7–8 cm of the end of the scintillator. The moulded tubing was quite stiff and strong and served to hold the joint together if the glue joint were to fail.

Inserted inside the light tight wrapping of each of the modules is a fibre optic light guide that was positioned so that it centred along the length and across the 8.5 cm face of the scintillator. These fibres are part of a laser based system which monitored the performance of many of the scintillating counters over time. The heart of the system is a pulsed nitrogen laser which produces ultraviolet light at a wavelength of 337.1 nm. The light from this laser is split and is routed to the scintillators through the ultraviolet transmitting fibres. This type of monitoring system provides an ideal signal since the plastic scintillator reacts to the ultraviolet light similar to the manner in which it reacts to charged particles. (However, there were problems with the reliability of the laser that was used during the 1991 run.)

By supporting the modules at the protruding ends of the PVC couplings in a round clamp, it was then possible to position the module at an arbitrary angle with respect to its long axis. Several different epoxy adhesives were tested for their strength in fastening PVC to polyvinyltoluene (PVT) based scintillator — the same base material of BC-408. It was found that the Nuclear Enterprises NE 581 Optical Cement commonly used in glueing light pipes to scintillator was as strong as any of the other adhesives when used to join small 0.5 square-inch PVC to PVT samples. A prototype of the PVC coupling with the notch machined through one end was then glued to a piece of scintillator with 5 × 8.5 cm^2 cross-section using the NE 581 optical cement. The shear strength of the prototype joint was measured to be approximately 200 kg before failure. The density of BC-408 is 1.032 g/cm^3 hence the mass of one of the bars is about 8.5 kg (5×8.5×200 cm^3 × 1 g/cm^3) which is supported at the PVC couplings at each end. Thus the strength of the NE 581 optical cement joint was more

than adequate to support the bars.

The notches in the PVC couplings were cut to fit the 5 cm nominal thickness of the bars. This dimension varied quite a bit away from 5 cm for individual bars as these faces of the bar were cast, not machined, when they were fabricated. The actual thickness varied from 4.95 cm to 5.28 cm. To ensure a proper fit with no large gaps to fill with cement, the PVC couplings had their notches machined to match the thickness of the bars. The surface finish of the long 5 cm wide sides varied significantly between the scintillator bars. Originally, these sides were to be polished to an optical quality finish; however, the manufacturer made a mistake and did not polish these surfaces. There was insufficient time to return the scintillators to Bicron to have them polished and to have the array completed before the start of the experiment in early 1991. Even so, the sides were reportedly diamond milled by Bicron and diamond milled scintillator surfaces have been shown to give results close to that of polished surfaces. Some of the scintillators did have quite a good machined surface appearance and reflected light quite well when they were viewed through their ends with the eye; however, many of the scintillators had sides of poor quality that did not reflect light well when they were viewed through the end. The scintillator bars with the better quality sides were placed at the middle locations on the array while the bars with the poorer quality sides were placed at the upper and lower locations of the array.

4.2 The Stand

The stand for the scintillator bars is shown in figure 20. The detector plane is adjustable between 10° and 20° from vertical in a direction towards the 48D48 magnet. It is currently set at 15.0°. The scintillator modules are arranged in two planes 9 cm apart with adjacent bars in different planes (figure 21) to allow

for overlap of coverage between the front and back bars so that no area was left uncovered and charged-particles could not sneak through any cracks. The two planes also allowed for the rotation of the modules about their long axis.

The array design allows the individual modules to be positioned such that kaons going through the spectrometer and which hit the back time of flight array will impinge upon the modules approximately perpendicular to their front (for kaons near the centre between the two ends). This geometry minimizes the variation in path lengths through the scintillator, which in turn reduces pulse height spread and timing walk.

4.3 Determination of the Module Pitch Angles

To determine the pitch angles at which to orient the scintillators, simulations of appropriate outgoing K^+ from the experimental target through the spectrometer to the time of flight array were carried out. The expected K^+ momenta and trajectories of interest for both the LH_2/LD_2 and L^3He experiments were propagated through a measured field map of the spectrometer dipole which had large fringe fields. Table 11 lists the expected angles for K^+ of interest for positions along the array within the vertical acceptance of the spectrometer.

The graph in figure 22 plots the expected K^+ angles against the position along the array. The actual bar angles were taken from the linear fit shown.

To ensure complete coverage of the time of flight wall area the support structure for the modules was designed in the following manner: In the front plane of the array the modules were positioned so that their centres were 16.0 cm apart with appropriate pitch angles. Then the modules in the back plane were aligned, with appropriate pitch angles, so that the gaps between the modules in the front plane were completely covered by them for incoming K^+ at the expected angles. The 8.5 cm width of the scintillators provided some overlap of

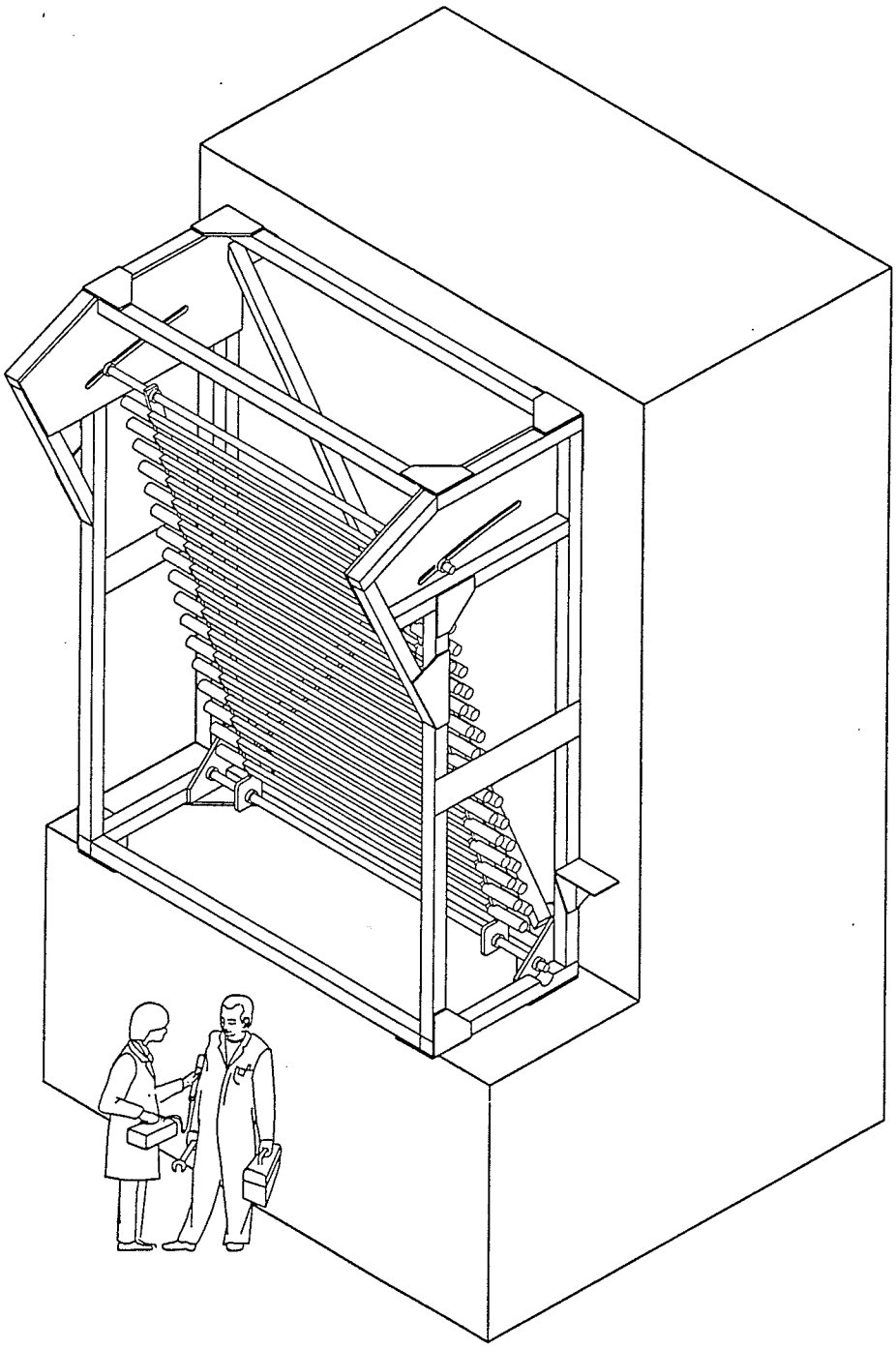

Figure 20: *The* K^+ *time of flight wall stand.*

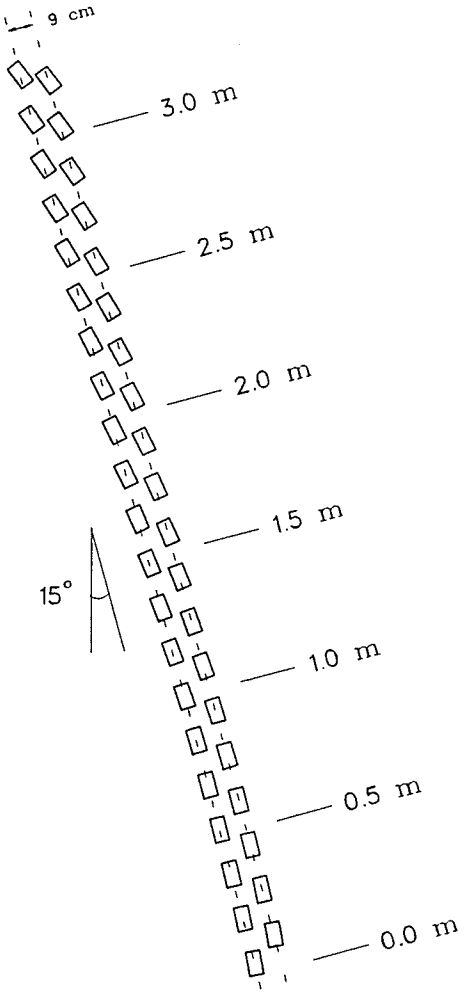

Figure 21: *The varying pitch angles of the individual modules in the* K^+ *time of flight array.*

Table 11: *Predicted* K^+ *angles at back time of flight wall.*

distance along wall[c], s (cm)	L^3He target[a] (p_{K+} = 1.4 – 1.8 GeV/c) θ (°)	LH_2/LD_2 target[b] (p_{K+} = 1.25 GeV/c) θ (°)
12	11.1	
50	13.9 – 15.3	
100	17.6 – 19.5	
150	21.4 – 23.2	
200	25.3 – 27.1	28.0
250	30.0 – 30.9	31.8
270	32.4	

[a] Experiment 836
[b] Experiment 813
[c] from bottom of array

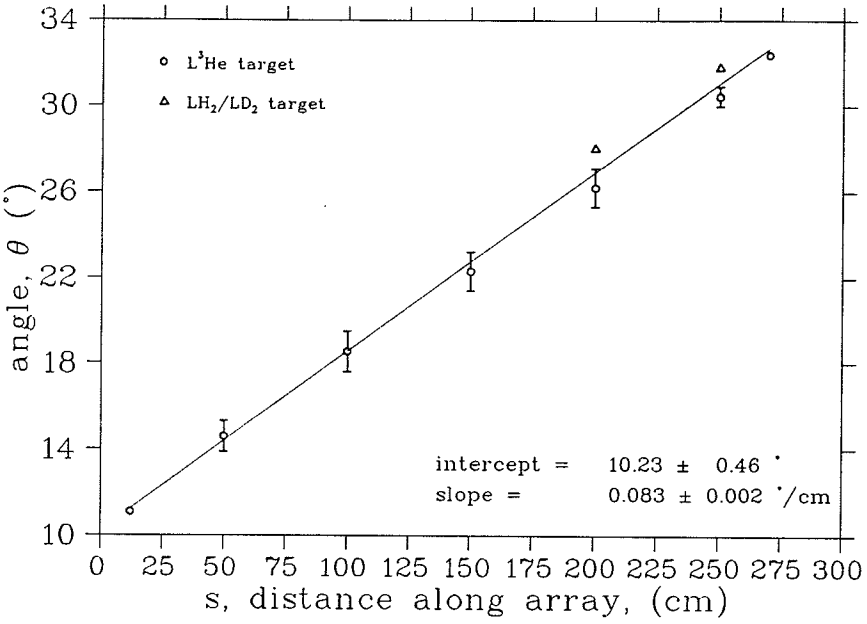

Figure 22: *Predicted pitch angles of* K^+ *at BT.*

coverage for adjacent modules. The positions and angles of the modules in the array are given in table 12.

4.4 Finger Calibration Detectors

Located directly behind the long scintillation counter planes are three narrow calibration scintillation detectors. They are made from $\frac{1}{8}'' \times \frac{3}{4}'' \times 12''$ BC-418 scintillator (Nuclear Enterprise Pilot-U equivalent) each viewed by a Hamamatsu H3167 photomultiplier tube.

These finger counters are oriented with their long dimension perpendicular to that of the long dimension of the time of flight bars and are mounted on a linear track which permits them to be moved along the vertical span of the array. The performance of the individual modules in the array could thus be monitored at three points defined by a coincidence with these fingers. Figure 23

Table 12: K^+ *time of flight array module positions.*

module number	distance along array, s (cm)	angle[a], θ (°)	effective angle[b], θ_{eff} (°)
1	4.25	10.6	-4.4
2	12.21	11.2	-3.8
3	20.25	11.9	-3.1
4	28.31	12.6	-2.4
5	36.25	13.2	-1.8
6	44.37	13.9	-1.1
7	52.25	14.6	-0.4
8	60.37	15.2	0.2
9	68.25	15.9	0.9
10	76.48	16.6	1.6
11	84.25	17.2	2.2
12	92.70	17.9	2.9
13	100.25	18.5	3.5
14	108.80	19.3	4.3
15	116.25	19.9	4.9
16	124.94	20.6	5.6
17	132.25	21.2	6.2
18	141.08	21.9	6.9
19	148.25	22.5	7.5
20	157.18	23.3	8.3
21	164.25	23.9	8.9
22	173.49	24.6	9.6
23	180.25	25.2	10.2
24	189.72	26.0	11.0
25	196.25	26.5	11.5
26	205.87	27.3	12.3
27	212.25	27.8	12.8
28	222.04	28.6	13.6
29	228.25	29.2	14.2
30	238.25	30.0	15.0
31	244.25	30.5	15.5
32	254.65	31.3	16.3
33	260.25	31.8	16.8
34	271.00	32.7	17.7
35	276.25	33.1	18.1
36	287.22	34.1	19.1
37	292.25	34.5	19.5
38	303.49	35.4	20.4
39	308.25	35.8	20.8
40	319.88	36.8	21.8
41	324.25	37.1	22.1

[a] angle relative to vertical
[b] vertical angle relative to array angle, $\theta_{eff} = \theta - 15°$

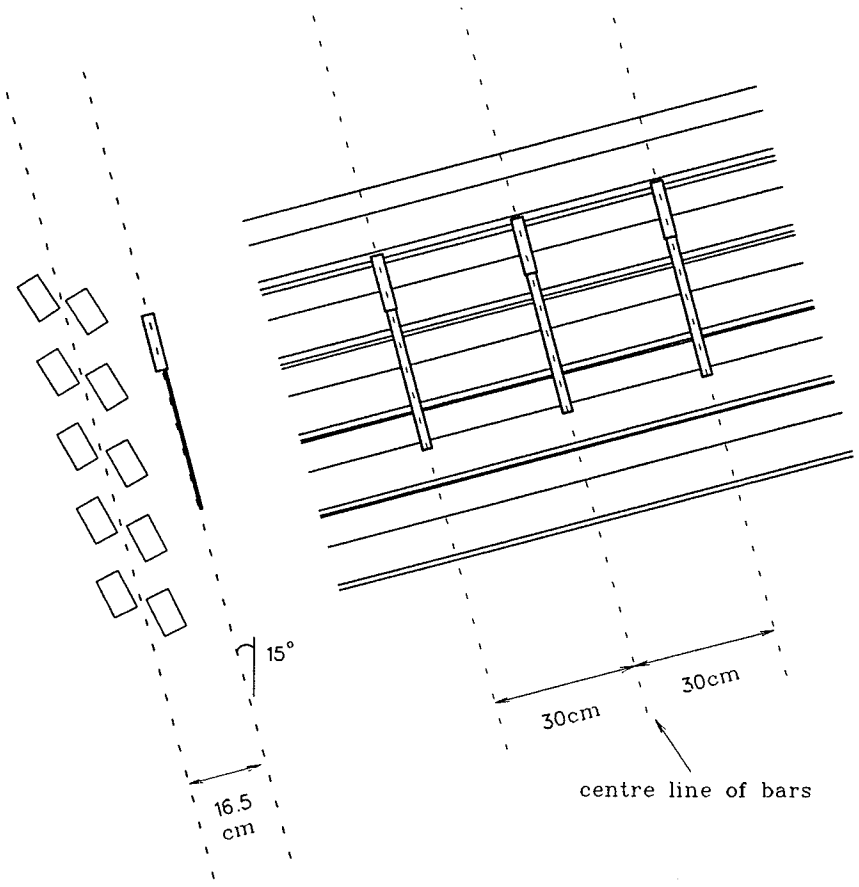

Figure 23: *Finger counters for the* K^+ *time of flight wall.*

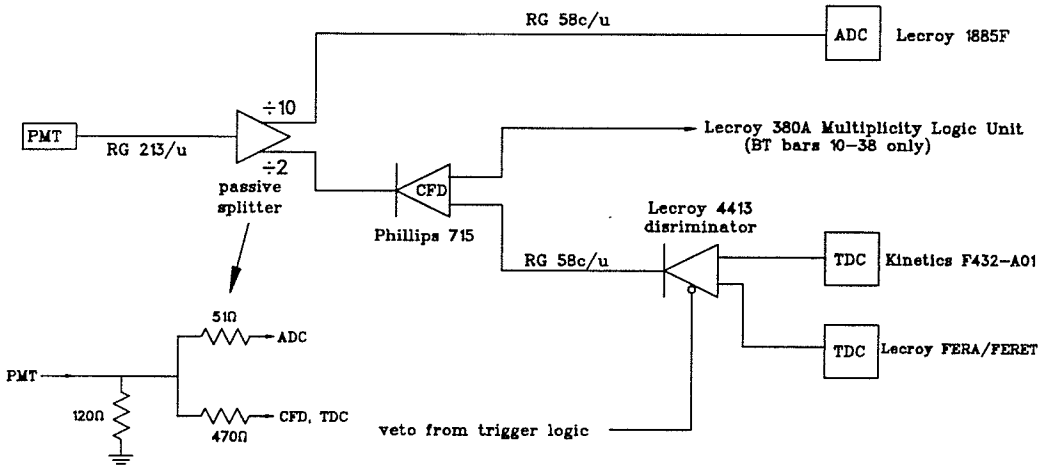

Figure 24: *Schematic of the* K^+ *time of flight wall electronics.*

shows the orientation of the fingers with respect to the scintillator array. They are currently positioned with the centre finger directly behind the middle of the 2 m length of the time-of-flight modules and the other two 30 cm to either side of the centre finger. Each finger may be adjusted within $\sim \pm 8$ cm from its present horizontal position.

4.5 Electronics

The photomultiplier tubes monitoring the time of flight scintillators are connected to ADCs and TDCs. Signals from the photomultiplier tubes are split, passively, resulting in $\frac{1}{10}$ of the original signal fed into the ADCs and $\frac{1}{2}$ of the original signal fed into the constant fraction discriminators which, in turn, are connected to the TDCs. (See figure 24 and table 13.) Two different TDCs are used to measure the timing signals. The Kinetics F432-A01 TDCs provide a fine timing resolution of 25 ps/channel. The Lecroy FERA/FERET are very fast conversion time TDCs (finest resolution of 50 ps/channel) which can pro-

Table 13: *Some specifications of the* K^+ *time of flight array electronics.*

CFD:	Phillips 715	- 5 channels - 100 MHz throughput - ± 75 ps time walk, typically (these CFDs do not have an adjustable zero crossing compensation network)
Discr.:	Lecroy 4413	- 16 channels - 150 MHz max. throughput - burst guard and updating modes
	these are leading edge discriminators	
TDCs:	Kinetics F432-A01	- 64 channels - 12 bit resolution - 25 ps minimum LSB (Least Significant Bit) - common STOP - $\leq$300 μs conversion time
	Lecroy 4300B/610 & 4303 FERA/FERET (Fast Encoding and Readout ADC and TDC)	- 16 input 11 bit ADC & 16 input time-to-charge converter - 50 ps/channel resolution - common START or STOP - 8.5 μs conversion time, typically
ADC:	Lecroy 1885F	- 96 channels - 15 bit resolution - 50 fC sensitivity - 8 event buffer - 265 μs conversion time

vide timing data that is fast enough to be used in a second level trigger. Both of the TDCs work with ECL logic signals which are derived from Camac 4413 discriminators which regenerate the CFD NIM signals and output ECL signals. In order to achieve better timing characteristics, the signal cables from the photomultiplier tubes in the experimental area to the CFDs located in an electronics trailer were kept to a minimal but equal length to reduce degradation of the signals. In addition, low dispersion coaxial cable was used to connect the PMT signals from the signal cable patch panel on the array frame to the splitters in the trailer which housed the electronics. The delay cables needed to allow for the processing of the data acceptance triggers were wired between the CFD outputs and the ECL-out discriminators. Aside from converting the NIM CFD signals to ECL, the 4413 discriminators restore fast rise times of the signals, lost to dispersion in the delay cable, before being fed to the TDCs

4.6 A Cursory Look at the Second Level Trigger

A large source of background which triggers the data acquisition system is (K^-,p) scattering in the target. These events are not a problem in terms of possible misinterpretation as H particle production but are a large problem in that they may overburden the data acquisition system and cause interesting events to be missed. Also, it is not desirable to have large numbers of these uninteresting events recorded onto the data tapes as it would impede the data analysis. A secondary trigger derived from information from the drift chamber inside the spectrometer magnet (FD3) and the K^+ time of flight array (BT) can be used to reduce the number of scattered proton events put to tape. This trigger was implemented for the last part of the 1991 LH_2/LD_2 target run. The primary level trigger for exiting K^+ from the target which go through the spectrometer was that the forward and back Čerenkov detectors do not fire and that

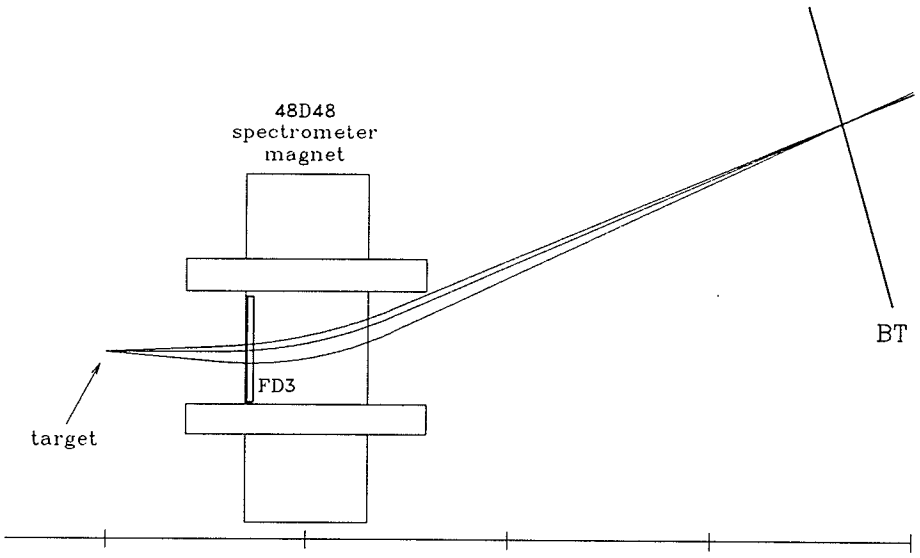

Figure 25: *Example of a higher momentum, 2.1 GeV/c, proton (top) impinging at the same BT position as lower momentum* K^+, *1.8 GeV/c (middle) and 1.4 GeV/c (bottom), within about 0.5 ns.*

the rear scintillation detectors do fire, all in coincidence ($\overline{\mathrm{BC}} \cdot \overline{\mathrm{FC}} \cdot \mathrm{FP} \cdot \mathrm{BP} \cdot \mathrm{BT}$). This rather loose definition of the primary level trigger for outgoing K^+ allows for scattered protons to initiate the trigger. The second level trigger makes use of the relationship between the position and time of flight to BT and the position of the particle when it passed through FD3 inside the magnet. Generally, protons and kaons with approximately the same time of flight (within ~ 0.5 ns) to a certain module in BT will have quite different trajectories through the spectrometer. For example, consider the situation in figure 25 where a proton and a kaon strike the same BT module with about the same time of flight. A proton with a higher momentum than the kaon can have the same time of flight as the kaon. But the proton will have a trajectory with a shallower bend and shorter flight path length through the spectrometer which will mean that it traverses

FD3 at a higher vertical position than the kaon. Along a similar line, this holds for all the modules in the BT array. Thus a series of maps of the FD3 active area can be made which could be used to distinguish between protons from kaons for known hit positions and times of flight by checking the region where the particle passed through FD3. Essentially, the trigger is generated after a low level test like this.

4.7 Calibration of the Array

A calibration run of the K^+ time of flight array was done early in the startup of Experiment 813 in May, 1991. The calibration was accomplished by reversing the field of the 48D48 spectrometer magnet from its normal operating mode in order to bend the beam up into the array. By varying the magnetic field of the dipole and selecting suitable momenta for the beam it was possible to sweep the beam vertically across the modules in the array. As this calibration run was done during the first few days of beam on the totally new beamline, a good K^- tune was not available. The beam consisted mostly of π^- and only a few per cent K^-. More K^- than was present in the beam at the time would have been useful. The data acceptance trigger was the coincidence of several of the scintillating detectors including the finger counters; specifically, the coincidence of IT·FP·BP·BS where any one of the modules in IT, FP, BP, or BS was hit. The finger counters did not extend up far enough to cover modules 39 and 40 in the array for this calibration. These calibration runs were done in two sessions. The first took data for the bottom half of the array with a beam momentum of 1.8 GeV/c while the second took data for the top half at a beam momentum of 1.0 GeV/c. The finger counters were moved by two array modules at a time — although the fingers could cover three modules completely at one time — and the beam was steered by the spectrometer magnet to intersect the fingers.

Also, the beam was defocused horizontally so that the beam particles would pass through the area defined by the three finger counters. Of the two TDC types monitoring the array, only the Kinetics F432-A01 TDCs were installed at the time of this calibration; thus there was no calibration of the FERA/FERET TDCs for these runs.

A second opportunity to obtain calibration data for BT occurred when the lucite Čerenkov detector was installed part way into the run time. Data to calibrate the FERA/FERET TDCs was taken at this time as well as additional data for the other TDCs. The data triggers for this calibration run were '$\pi\pi$' and 'πK' triggers which were defined mainly by the Čerenkov detectors. ('πK' signifies a pion incident on the target and a kaon out through the spectrometer.) The finger counters were not utilized during this calibration run and the beam was focused tightly as for normal operation so that the beam spot intersected the middle of the modules in the array with minimal dispersion.

Various timing constants were determined by the calibration. These included, for each module, the time of flight offsets — the difference between what is output by the TDCs and the true time of flight — and the time difference offsets — the difference between the TDC outputs for either end of the modules. The calibration also checked the performance of the modules of the array. The offsets are due to anything in the signal path from the photomultiplier tube to the TDC, which affects the timing of the signal: items such as the lengths of the signal cables, the transit times of electrons through the photomultiplier tubes and the propagation times of the various electronic devices, among other things.

To check if the constant fraction discriminators did indeed remove timing walk due to pulse height variations, plots of the ADC versus TDC values for the events impinging some of the modules were done. Figure 26a shows a density box plot of the pulse height against stop time for the right photomultiplier tube

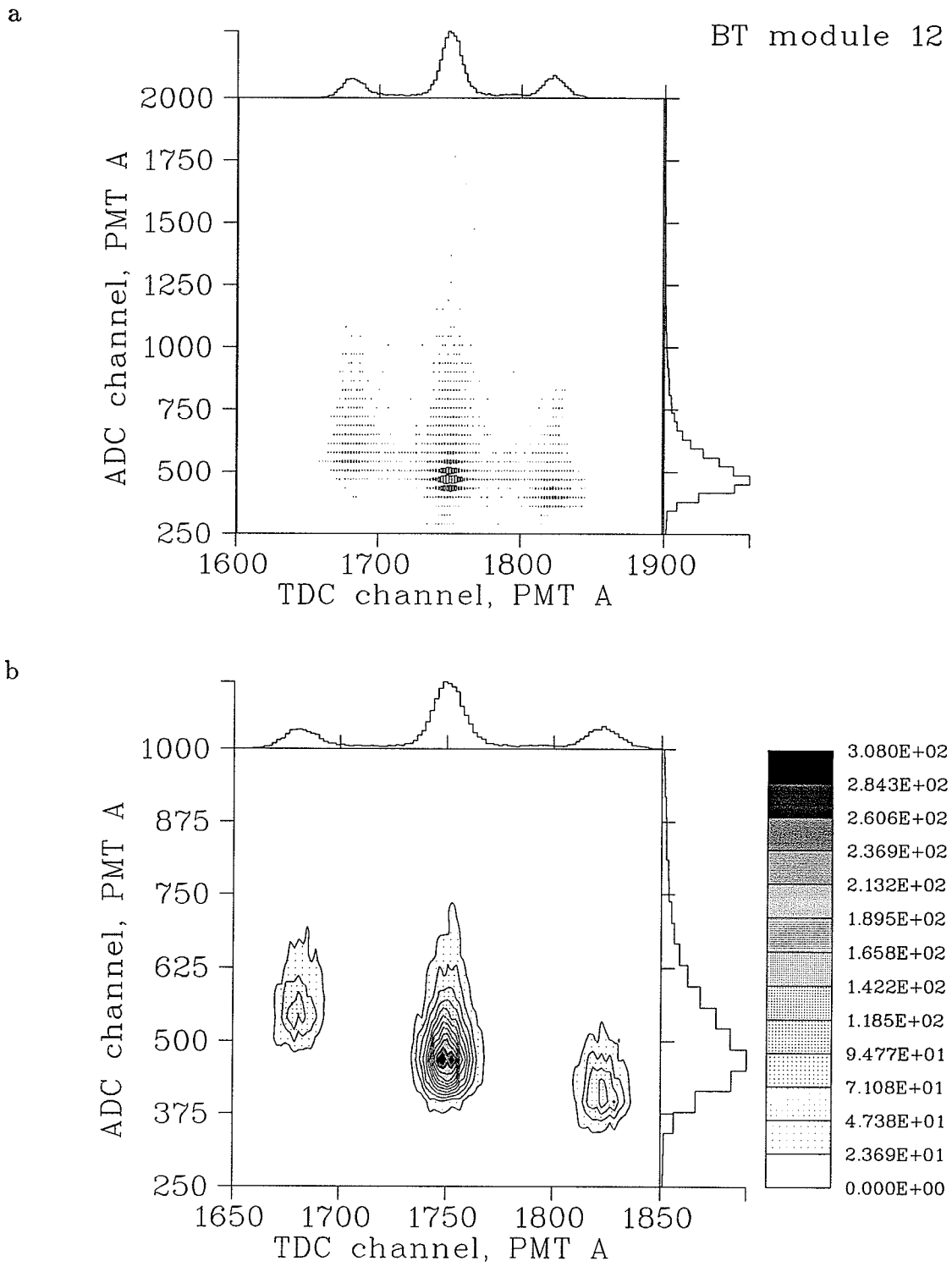

Figure 26: *Pulse height versus stop time for the right photomultiplier tube of BT module 12. (a) Box density plot, (b)Dithering density (contour) plot.*

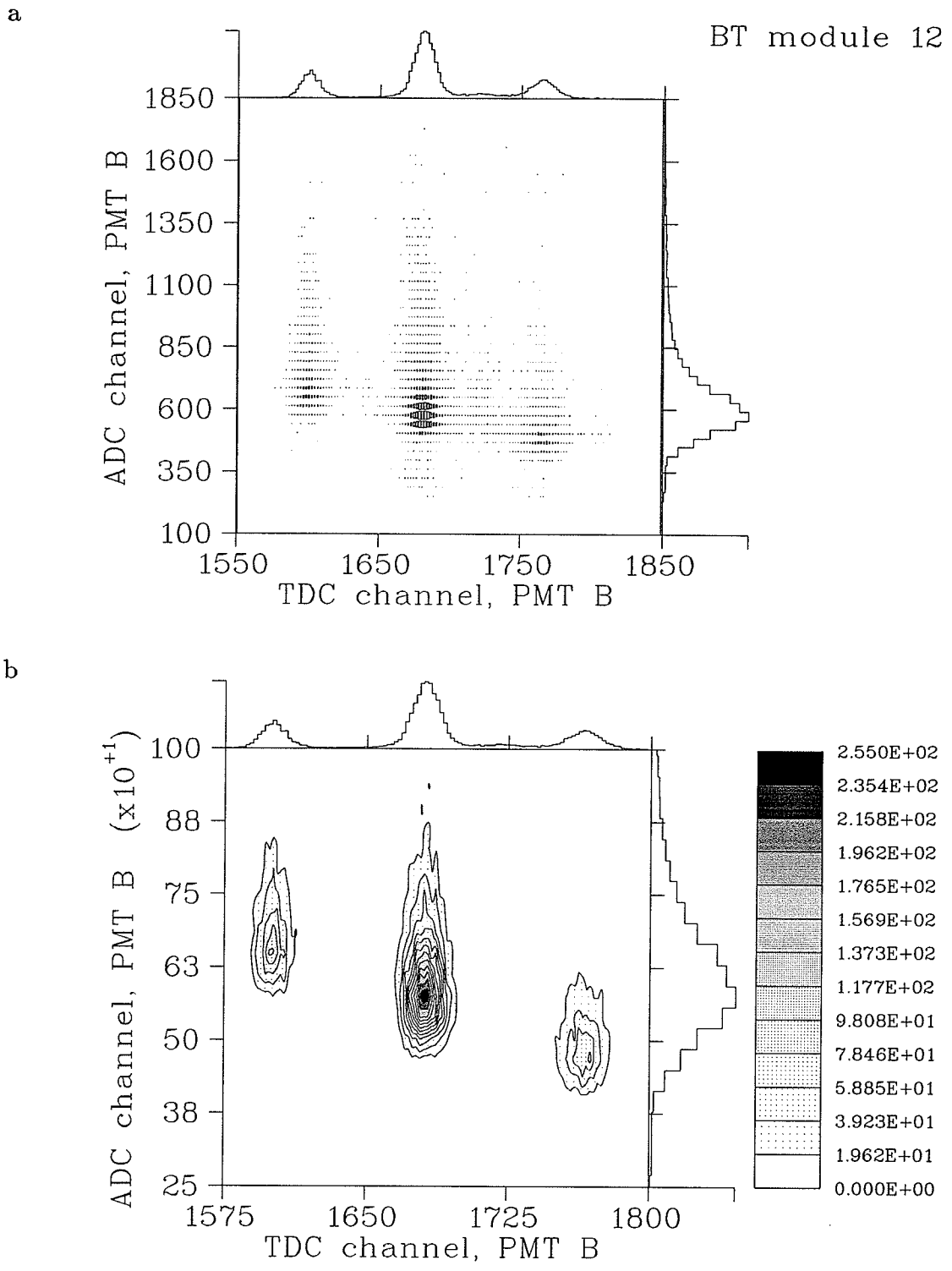

Figure 27: *Pulse height versus stop time for the left photomultiplier tube of BT module 12. (a) Box density plot, (b)Dithering density (contour) plot.*

on module 12. The three data clusters are due to the finger counters present in the trigger; thus each cluster represents a well defined position along the length of the scintillator bar. Notice that the data in each cluster does not show a dependence on the pulse height as there is no apparent shift in the TDC values within the ADC range. This may be more obvious in figure 26b which shows the data as a dithering density plot. Similarly, figure 27 shows the independence of the stop time from pulse height variations in the left photomultiplier tube in module 12. If leading edge discriminators were used the time walk would appear as a shift to smaller time values for larger pulse heights. Hence it may be concluded that the timing walk from the constant fraction discriminators is insignificant.

4.7.1 Time Difference Offsets and the Effective Speed of Light in the Modules

The time difference offsets which calibrate the centre position of the scintillator modules were determined by looking at events where there was a coincidence between the centre finger counter and the individual time of flight array modules. The calibrated time difference between the two ends of the modules at the centre position was defined to be zero and the time difference offsets were then simply taken as the difference of the right TDC value from the left TDC value, $t^{offset}_{difference} = t_{left} - t_{right}$ where left and right are defined by looking into the front face of the array.

The effective speed of light, c_{eff}, in the individual modules was determined by looking at the time difference spectra for events that were in coincidence with the left, centre, and right finger counters. The centroids of the time difference spectra for the finger coincidences were then fitted with a straight line to the respective finger positions. The fit was weighted according to the number of

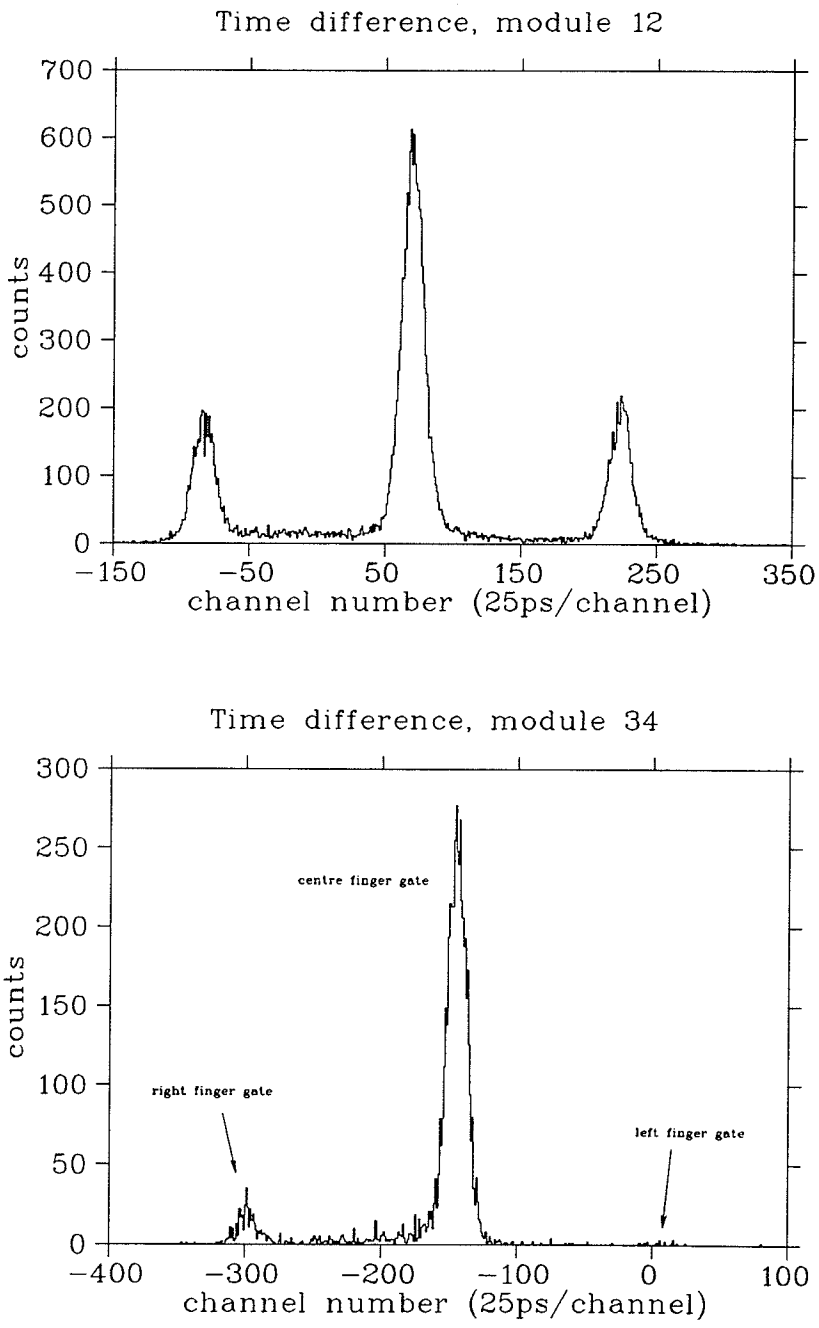

Figure 28: *The time difference spectra of modules 12 and 34 from the May 1991 BT calibration runs.*

hits in each finger coincidence as the distribution of hits among the three fingers varied considerably (see figure 28).

Table 14 lists the above calibration constants. With the time difference offsets and the effective speeds of light of the modules the hit position along the scintillator bars may then be determined.

4.7.2 Time of Flight Offsets

The time of flight offset is the difference between the time average of the TDC measurements from the two ends of a scintillator module and the actual time of flight of a particle from some reference point to the module. (Section 3.7, equation 9.) For the H particle search the reference timing comes from the IT counters. Hence, the calibration is needed to find the difference between the TDC time average measurements and the actual time of flight for particles travelling from IT through the spectrometer back to BT. The actual time of flight for particles from IT to BT was determined by dividing the flight path length by the particle velocities. The path length from IT to BT is not constant but depends on where the beam particle hits the BT array. Only particles striking the centre of the BT array modules were examined for the following to reduce the path length variations that needed to be considered. The flight path lengths were estimated by following beam particles bent up towards BT through the mapped spectrometer field in a simulation. Assuming that the entire magnetic field of the spectrometer scales linearly or nearly linearly as the central field is varied, the trajectories of charged particles of different momenta with the magnet adjusted so that the particles hit the same position on the array should be the same. Thus the path lengths of charged particles to the same position on the array would be the same regardless of the magnet setting or the beam momentum.

The path length versus centre position along the array relationship was fitted to a fifth order polynomial with the result, for odd number bars:

$$\begin{aligned}\text{path length} &= 72.4 + 782.2 - 0.1787s + 8.516 \times 10^{-4}s^2 - 3.374 \times 10^{-7}s^3 \\ &\quad +2.105 \times 10^{-9}s^4 + 4.497 \times 10^{-12}s^5, \end{aligned} \tag{23}$$

where s is the distance, in cm, from the array bottom to the centre of the module and the path length is in cm also. The first constant term represents the distance from IT, the time of flight start, to the target centre and the remaining terms are the fitted path length parameters which were calculated by taking the start from the target centre. For even number bars which lie 9 cm behind the plane of the odd number bars, an additional path length of $9/\cos\theta_{eff}$ cm was added, where θ_{eff} are listed in table 12. This was an approximation which assumed that the beam particles had trajectories near perpendicular to the front face of the bars. Table 14 lists the time average offsets and their resolutions.

The time of flight offsets for the Kinetics F432-A01 TDCs listed in table 14 were derived from multiplicity one data spectra. That is data from trigger events where only a single module in the array was hit. This excluded events where beam particles traversed through two modules where adjacent modules overlapped. This was done because some of the modules had spectra peaks for these data — multiplicity two events in adjacent modules — at anomalously large separations from the multiplicity one peaks. This will be discussed further in section 4.7.6.

4.7.3 Timing resolutions

Also listed in table 14 are the time average and time difference resolutions for the individual modules. On average, over all the counters with sufficient events, the raw time average resolution was 0.29 ± 0.04 ns FWHM and the raw time difference resolution was 0.43 ± 0.04 ns FWHM. These numbers do not include

Table 14: *Calibration constants of the* K^+ *time of flight wall modules. (See the bottom of the table for a key.)*

	Kinetics F432-A01								Lecroy FERA/FERET	
module	path length (cm)	tof_0 (ns)	$fwhm_{tof}$ raw (ns)	$fwhm_{tof}$ fitted (ns)	t_0^{dif} (ns)	$fwhm_{dif}$ raw (ns)	$fwhm_{dif}$ fitted (ns)	c_{eff} (cm/ns)	tof_0 (ns)	t_0^{dif} (ns)
p = 1.8 GeV/c									p = 1.4 GeV/c	
1	853.91	13.10	0.33	–	-6.35	–	0.51	16.26 ± 0.37	15.64	0.05
2	861.52	14.57	0.30	0.32	-3.55	0.50	0.55	16.29 ± 0.09	15.58	-3.20
3	851.38	12.21	0.45	0.45	0.55	0.82	0.86	15.93 ± 0.12	11.53	3.85
4	859.23	10.94	0.25	0.29	-7.95	0.43	0.44	15.59 ± 0.08	15.71	-3.30
5	849.28	11.45	0.33	0.32	-3.73	0.43	0.44	15.92 ± 0.04	16.05	-1.95
6	857.36	10.38	0.25	0.30	-4.75	0.38	0.45	15.73 ± 0.04	15.03	-1.25
7	847.60	10.83	0.28	0.30	-11.18	0.40	0.46	16.10 ± 0.05	14.25	-3.40
8	855.92	14.55	0.25	0.31	6.65	0.50	0.50	15.58 ± 0.04	14.22	0.05
9	846.35	14.50	0.25	0.28	-9.05	0.40	0.42	15.76 ± 0.13	12.19	-2.55
10	854.89	16.24	0.25	0.29	-4.45	0.43	0.45	15.77 ± 0.14	13.11	-2.65
11	845.52	13.08	0.23	0.26	-6.70	0.40	0.42	15.77 ± 0.09	13.82	-1.65
12	854.28	14.38	0.28	0.31	1.75	0.47	0.52	15.69 ± 0.04	13.43	-2.85
13	845.12	15.01	0.30	0.31	-4.28	0.45	0.45	15.80 ± 0.04	11.19	-2.15
14	854.11	11.61	0.25	0.33	8.18	0.47	0.45	15.60 ± 0.03	10.88	-1.95
15	845.14	11.26	0.25	0.31	-3.67	0.40	0.42	15.62 ± 0.04	12.09	0.85
16	854.35	13.03	0.25	0.32	-6.65	0.45	0.45	15.64 ± 0.08	11.13	-3.90
17	845.59	17.35	0.23	0.31	4.72	0.45	0.42	15.70 ± 0.04	12.42	-0.85
18	855.03	16.16	0.33	0.38	3.53	0.40	0.42	15.40 ± 0.04	12.55	-0.80
19	846.47	12.62	0.30	0.33	4.53	0.38	0.39	15.78 ± 0.08	11.84	-2.05
20	856.14	15.37	0.30	0.33	7.33	0.43	0.51	15.27 ± 0.07	11.96	-0.40
21	847.77	17.28	0.25	0.31	4.28	0.38	0.37	15.57 ± 0.06	12.85	2.45
⋮	⋮	⋮	⋮	⋮	⋮	⋮	⋮	⋮	⋮	⋮

continued

path length: as determined from equation 23

tof_0: time of flight offset

t_0^{dif}: time difference offset of the ends of the module

$fwhm_{tof,dif}$

raw: the Full Width at Half Maximum of the timing peak from the histogram spectrum (25 ps histogram bin width)

fitted: the Full Width at Half Maximum of the timing peak from the width of a Gaussian fitted to it

c_{eff} effective speed of light in the module as determined with the finger counters

Table 14: (continued) *Calibration constants of the* K^+ *time of flight wall modules.*

	Kinetics F432-A01								Lecroy FERA/FERET	
module	path length (cm)	tof_0 (ns)	$fwhm_{tof}$ raw (ns)	$fwhm_{tof}$ fitted (ns)	t_0^{dif} (ns)	$fwhm_{dif}$ raw (ns)	$fwhm_{dif}$ fitted (ns)	c_{eff} (cm/ns)	tof_0 (ns)	t_0^{dif} (ns)
p = 1.0 GeV/c									p = 1.4 GeV/c	
22	857.68	18.08	0.35	0.34	8.70	0.43	0.47	15.52 ± 0.13	13.26	1.25
23	849.50	17.78	0.30	0.33	6.28	0.45	0.43	15.91 ± 0.15	11.59	-1.65
24	859.65	25.57	0.33	0.40	0.28	0.43	0.45	15.67 ± 0.06	13.54	-3.20
25	851.64	15.86	0.35	0.31	1.20	0.40	0.46	15.65 ± 0.01	–	–
26	862.02	10.99	0.30	0.35	-4.93	0.40	0.45	15.44 ± 0.05	10.96	-1.15
27	854.19	12.63	0.30	0.39	8.88	0.47	0.48	15.40 ± 0.14	11.28	1.05
28	864.81	16.79	0.38	0.34	-0.45	0.43	0.47	15.59 ± 0.14	11.51	-0.70
29	857.14	17.18	0.30	0.34	-0.25	0.45	0.45	15.75 ± 0.03	12.58	-1.40
30	868.00	14.19	0.33	0.34	3.23	0.43	0.45	15.43 ± 0.07	11.20	0.00
31	860.47	14.74	0.40	0.41	3.10	0.68	0.66	15.86 ± 0.02	10.77	0.15
32	871.60	14.54	0.30	0.34	-4.97	0.50	0.49	15.38 ± 0.25	11.93	-3.05
33	864.16	14.66	0.23	0.33	-2.40	0.40	0.45	15.72 ± 0.12	12.65	-1.55
34	875.55	18.56	0.33	0.33	-3.60	0.45	0.43	15.55 ± 0.06	10.84	-1.25
35	868.18	15.80	0.30	0.34	-6.55	0.40	0.44	15.87 ± 0.08	11.56	-2.65
36	879.79	20.24	0.30	0.31	-2.65	0.43	0.45	14.97 ± 0.02	12.55	-3.10
37	872.51	15.46	0.30	0.34	-10.48	0.40	0.44	15.76 ± 0.04	11.02	-1.05
38	884.34	20.89	0.23	–	-5.45	0.38	0.43	15.81 ± 0.11	13.64	-1.15
39	877.09	14.75	–	–	–	–	–	–	11.97	–
40	889.17	-29.93	–	–	–	–	–	–	13.27	–

the results from modules 3 and 31 which have worse resoltion due to bad timing in one of the photomultiplier tubes in the modules. The time average resolutions have folded into them the time of flight start resolution of the IT counters. On close inspection, it can be noticed that the resolutions of the modules in the bottom half of the array were somewhat better than those for the top half of the array. This was an artefact of the momentum spread in the beam and the two different beam momenta used to calibrate the two halves of the array and was not due to intrinsic differences between the upper and lower modules. The measured momentum spread in the beam was $dp/p = 5\%$ FWHM. At a beam mometum of 1.8 GeV/c, this momentum spread led to a time of flight spread of $\sim$8 ps FWHM for pions over 8m. The corresponding time of flight spread for 1.0 GeV/c pions was $\sim$25 ps FWHM. These time spreads contributed linearly to the timing resolutions of the modules and accounted for the difference in the resolutions of the top and bottom modules.

The IT start resolution for each of its four modules can be determined by taking one-half of the time difference between the two photomultiplier tubes attached to each one — the IT scintillators are small enough so that position dependence of the time difference is small also. Table 15 lists the resolutions of the IT modules. Nearly all of the beam particles hitting BT passed through either IT modules 2 or 3 with very few through the outer modules, 1 and 4. If the resolution of IT is taken to be the average of modules 2 and 3, for the purposes here, then the time of flight start resolution is 0.16 ns FWHM. The position resolution for each module was determined from the time difference resolution and the effective speed of light in the module and the average over all the modules was 3.5 ± 0.7 cm FWHM.

Table 15: *Time of flight start resolutions of the individual IT modules.*

module number	raw time resolution (ns) FWHM
1	0.26
2	0.13
3	0.18
4	0.14

4.7.4 Finger Timing

Attempts to determine whether or not the above assumption that the trajectories, and hence path lengths, of charged particles intersecting the BT array at the same location was valid were made by analysing the data from the calibration in different ways. Since the finger counters were used to gather data needed to find the time average offsets for all the BT modules in the first calibration runs the finger timing data ostensibly contained information about how the time of flight of the beam particles varied as the fingers were moved up the array. As the same detectors, which have constant timing offsets, measured the time of flight variations along the array, the finger timing could be used to determine whether the path length formula held true in principle. However, the fingers were not designed for timing and several significant factors concerning the fingers worked to the detriment of a good comparison between the two. Firstly, the finger scintillators were viewed by only one photomultiplier tube. Because of this the timing recorded by the finger TDC would be dependent on the hit position along the finger length. Secondly, the fingers were rather thin and long which meant that there would be a relatively small amount of light released by

charged particles traversing through the scintillator and there would be a rather large variation in amplitude of the light received and signal output by the photomultiplier tube between charged particles traversing the scintillator near the end close to the photomultiplier tube and those traversing at the far end. Thirdly, the discriminator to which the photomultiplier tube was connected was a leading edge discriminator and, fourthly, the signal size was not monitored by an ADC. Hence, the timing walk of the time measurements could not be corrected for. In spite of all this and a somewhat convoluted analysis needed to obtain the desired data, the comparison was done as described below.

The general idea behind this particular analysis was that if the finger timing recorded during the calibration could be corrected for the hit positions on the finger then the remaining variation in the timing of the finger would be due solely to the time of flight variations of the particles for different positions on the array. It turned out that a rough correction could be made to the timing data. As above, only the centre finger counter was used in this analysis. Even though the positions of the centre finger counter was known during the calibration, the hit position along the finger was not well defined due to it being viewed by the single photomultiplier tube. The hit positions on the finger had to be known for some of the data for this procedure to work. Narrow relative hit positions on the finger were estimated by projecting the positions where adjacent BT scintillators overlap back onto the finger counter at the average of the two overlapping bar pitch angles. This was done for the points where multiplicity two events on the BT modules had a sufficient number of events to analyse (recall that the finger counters were in the trigger). Figure 29 shows the estimated relative hit positions on the centre finger for the various positions of the finger along the array. It was noted that the hit positions on the finger relative to the corresponding BT module overlap positions remained about constant as the finger was moved along the array as can be seen by the roughly horizontal bands in which points

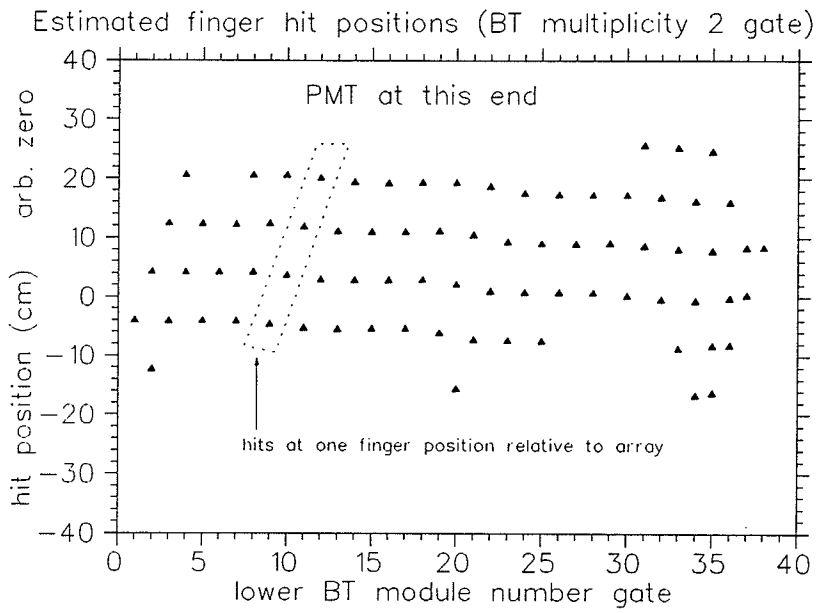

Figure 29: *Relative hit positions on the centre finger counter predicted for multiplicity two events in the BT array.*

in figure 29 lie. Hence, some roughly defined finger hit positions with several points at each position were available.

To correct for the timing of the finger counter due to the hit position on the finger as extracted above, timing data obtained under the same circumstances (*i.e.* the same time of flight to the finger) for the various hit positions need to be used. However, this sort of information was not available and had to be estimated from the multiplicity two finger timing data which had the different time of flight distances for the finger positions along the array folded into it. The procedure was to normalise the beam particle time of flight distances so that the timing differences remaining in the finger timing would be due only to the hit position on the finger. This had to be done with the known beam momentum and the path length equation 23. Although this was the equation that was to be checked with the work here, it was the only way to get the required information.

Consequently, the comparison here was not independent but the results would show if the path length formula were consistent with the data.

The timing data were taken as the centroids of the timing spectra of the multiplicity two gated finger events. The path lengths to the finger from IT were estimated to be the sum of the path lengths from equation 23 to the BT module overlap positions and the distance from the overlap position to the finger at the average pitch angles of the overlapping modules. The reference path length was chosen to be the one from IT to the finger gated on multiplicity two events in modules 20 and 21. The path length differences from the reference were converted to time differences using the π^- velocity which were then used to adjust the timing data. The finger timing data obtained by normalising the path length traveled by the π^- is shown in figure 30. The points plotted with the same symbol in the figure represent one finger hit position as the finger was moved across the array. The roughly horizontal timing bands of the different finger hit positions demonstrated that the reasoning for the analysis above was reasonably sound.

Finally, the correction to the multiplicity two finger timing data was taken to be the time differences in the average time of the points in each band of hit position in figure 30. The finger timing corrected in this manner are shown in figure 31. Included in the figure is a fit of the predicted time of flight curve to the centre finger derived from the path length formula. (Note that the discontinuity is due to the change in beam momentum from the calibration of the top and bottom halves of the array.) From the coarse agreement of the corrected data and the predicted data it was concluded that the path length equation was approximately correct.

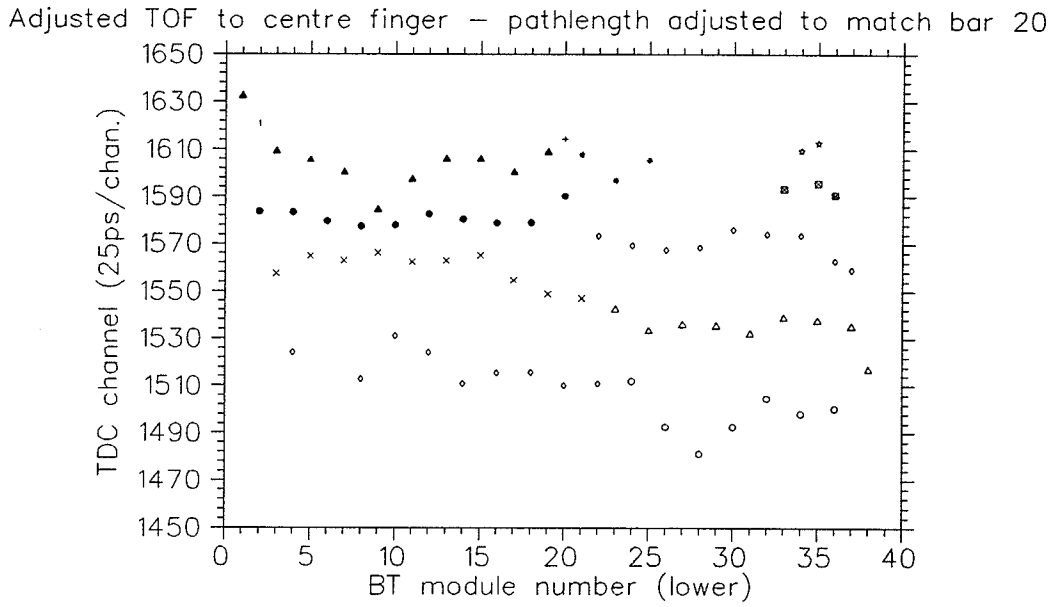

Figure 30: *Timing to the finger adjusted so that flight path lengths are the same as path length through the bar 20 and 21 multiplicity two gate. The time of flight offset is not accounted for in the plot.*

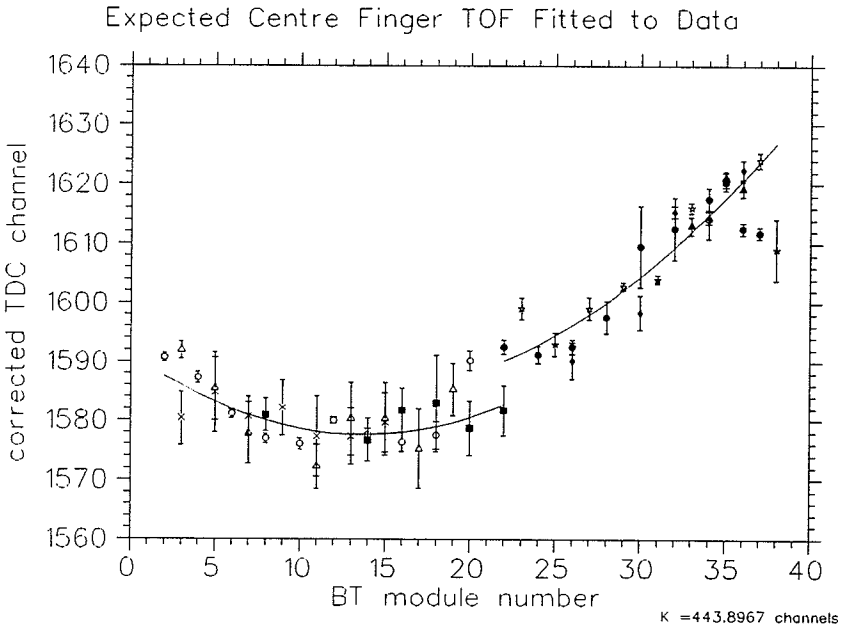

Figure 31: *The timing to the centre finger counter after time correction due to hit position. Note that the discontinuity in the curve is a result of the two different beam momenta used to calibrate the array — 1.0 GeV/c for the lower half and 1.8 GeV/c for the upper.*

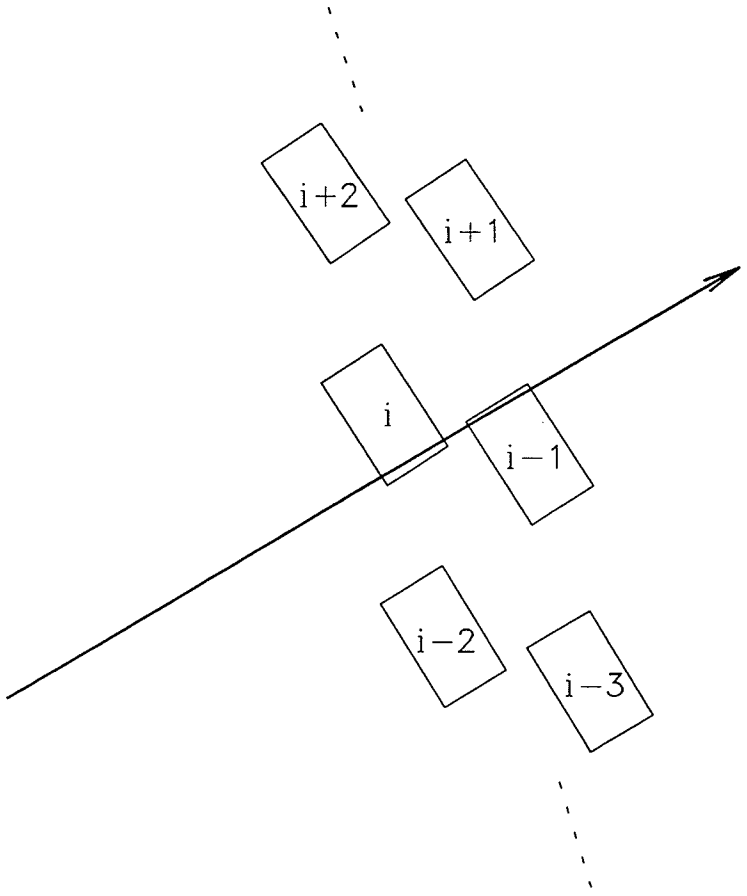

Figure 32: *A charged particle resulting in a multiplicity two event in adjacent scintillator bars.*

4.7.5 Multiplicity Two Timing

Another method was used in an attempt to derive the time of flight offsets; this one without relying totally on the path length equation. This method relied upon the multiplicity two data in the array and used the centre finger counter to define the centre of the BT modules only. However, as briefly mentioned above, problems with the Kinetics F432-A01 TDCs limited the value of such an offset determination. In any case, the following few paragraphs describe how this calculation was done.

Consider the schematic diagram in figure 32 which shows a side view of

some of the bars in the array. Let τ be the time of flight or time average offset, T be the time average as measured by the TDCs, and t be the actual or true time of flight. Define $t = T - \tau$. Assume that the time average offset for each bar is constant throughout the width of the bar. That is, assume that if the time average offset were measured for different positions across the width of the bar at the same distance between the ends of the bar then the same offset would result. For the charged particle traversing through both bars i and $i-1$ in figure 32, the actual time of flight to bar $i-1$ relative to bar i is

$$t_{i-1}^{\text{top}} = t_i^{\text{bottom}} + t_{i,i-1}^{\text{gap}}$$

where top and bottom refer to the top and bottom edges of the bars and $t_{i,i-1}^{\text{gap}}$ is the time of flight of the charged particle between the front face of the bottom edge of bar i and the front face of the top edge of bar $i-1$. Substituting the actual time of flight with the measured time average and offset gives

$$T_{i-1}^{\text{top}} - \tau_{i-1} = T_i^{\text{bottom}} - \tau_i + t_{i,i-1}^{\text{gap}}$$

and rearranging gives

$$\tau_{i-1} = T_{i-1}^{\text{top}} - T_i^{\text{bottom}} + \tau_i - t_{i,i-1}^{\text{gap}}.$$

For multiplicity two events $T_{i-1}^{\text{top}} - T_i^{\text{bottom}}$ can be measured. Then for the next bar line,

$$t_{i-2}^{\text{top}} = t_{i-1}^{\text{bottom}} + t_{i-1,i-2}^{\text{gap}}$$

which when rearranged gives

$$\tau_{i-2} = T_{i-2}^{\text{top}} - T_{i-1}^{\text{bottom}} + \tau_{i-1} - t_{i-1,i-2}^{\text{gap}}.$$

When τ_{i-1} is substituted for and rearranged, this yields

$$\tau_{i-2} = T_{i-2}^{\text{top}} - T_i^{\text{bottom}} + (T_{i-1}^{\text{top}} - T_{i-1}^{\text{bottom}}) + \tau_i + t_{i-1,i-2}^{\text{gap}} - t_{i,i-1}^{\text{gap}}.$$

It is obvious that $T_{i-1}^{\text{top}} - T_{i-1}^{\text{bottom}} = t_{i-1}^{\text{top}} - t_{i-1}^{\text{bottom}}$ which shows that the time of flight difference between the top edge and bottom edge of the individual bars is automatically accounted for in this procedure. Hence the explicit time of flights to the bottom and top edges for the same bars are not required which is fortunate since we do not know them.

Similarly, time average offsets for bars $i-3, i-4, \ldots, i+1, i+2, \ldots$ may be computed in this manner of daisy chaining the offsets for multiplicity two events until entire array is done. In fact, these time average offsets are all relative to the initial reference module, i, and are independent of the path length equation 23. What is uncertain about this procedure is whether or not the assumption that the offset is constant across the width is good. Also, the actual trajectory of the charged particle which produces the multiplicity two event has an effect on the actual $t_{i,i-1}^{\text{gap}}$ and will affect the calculated offsets somewhat.

The time of flight between the bars of the π^- in the calibration were estimated by using the known π^- momentum and using the distance between the front planes of the adjacent bars assuming the π^- impinge upon the front bar face at right angles and near the edge. Figure 33 compares the time average offsets derived this way with those determined with the path length formula. The relatively large oscillations in the difference between the two offset calculations in figure 33 was due to the aforementioned discrepancy between multiplicity one and multiplicity two spectra peaks in some of the modules. Some of the multiplicity one and two peaks were more than 0.5 ns apart, quite a large difference.

4.7.6 Problems with Some TDCs

During the initial analysis of the time of flight wall calibration data from the beginning of beam time in May 1991 it was apparent that some modules in the array showed two peaks in their time average spectra where there should

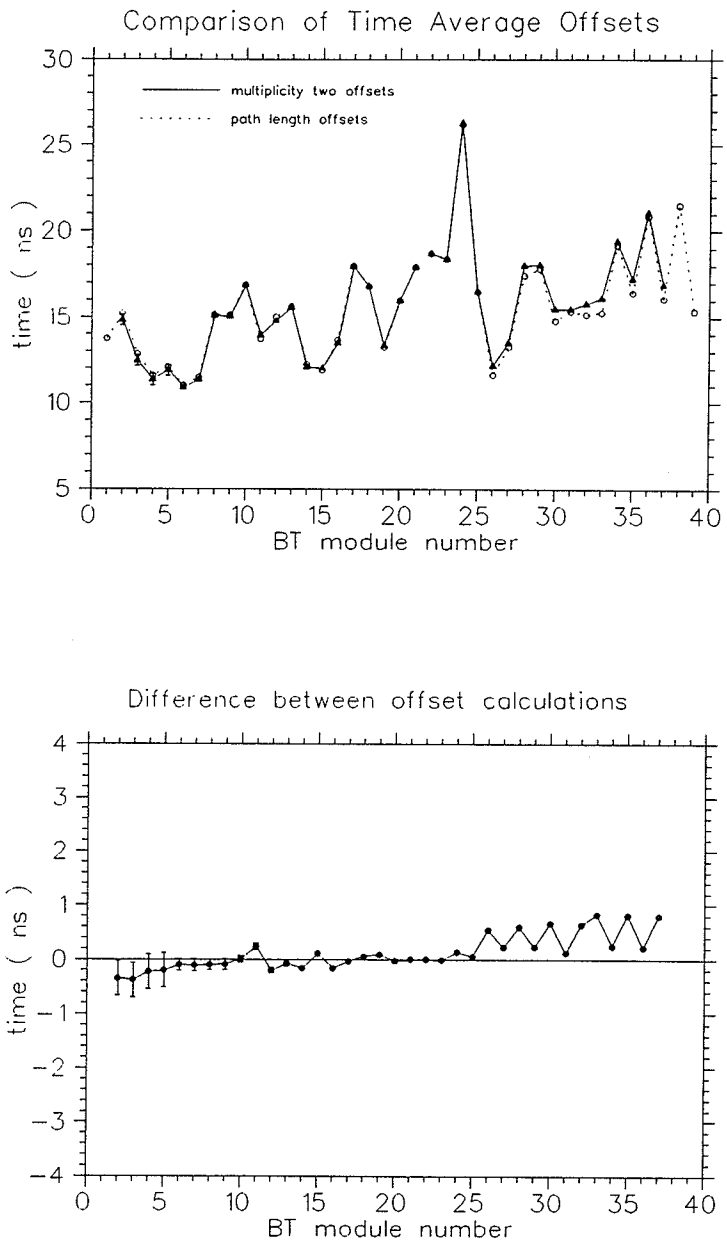

Figure 33: *Comparison of the time of flight offsets for BT calculated with the predicted path length formula and daisy chaining the multiplicity two data.*

have only been one, namely a single peak from the π^- that essentially made up all of the beam. The origin of the mysterious double peaks was completely unknown until the attempt to extract the time of flight offsets from multiplicity two data was done. It was discovered that the time average peak positions for the anomalous modules differed depending on whether a single bar was hit or two adjacent bars were hit. The modules which clearly showed some peculiar behavior between multiplicity one and two events were modules 25, 27, 29, 31, 32, 34, and 36. Modules 10 and 12 had a much smaller separation between multiplicity one and two peak centroids which were only discernable when the two types of events were separated. This discrepancy solves the above puzzle of the oscillating behaviour in the time difference curve between multiplicity one and two events in figure 33 but it is a more fundamental problem. Notice that the modules with the discrepancy occur in every other one from module numbers 25 to 31 and from 32 to 36. Thus with the determination of the multiplicity 2 offsets by daisy chaining through the bars the offsets for those bars will be incorrect while the ones between them would be, more or less, correct. The discrepancy was always on the smaller side of the single hit peaks hence the problematic offsets were always larger than the multiplicity 1 offsets and when the difference was taken against the multiplicity one values the result would oscillate at every other bar. That is, the oscillations were due to a combination of the anomalous offsets always being larger and the fact that only every other module was problematic. It is interesting to note that only the time average spectra showed this behavior while the time difference spectra did not. Also, the separation appeared in the time spectra of the individual photomultiplier tubes at each end of the modules with anomalies.

When the time of flight data from the BCL (lucite Čerenkov) calibration was analysed, it became apparent that only the Kinetics F432-A01 TDCs had the strange behaviour. Recall that Lecroy FERA/FERET were not installed in

the initial calibration. Figure 34 shows the time average spectra for module 34 with both the F432 and FERA/FERET TDCs separated for multiplicity one and two events where both π^- and K^- are in the beam. Since the FERA/FERET TDCs do not act up in this way it can be concluded that the problem lies in the F432 TDCs and not elsewhere in the array electronics.

As of the writing of this material, these latter TDCs were being tested at Carnegie Mellon University and by Kinetics, the manufacturer. Preliminary results of the tests indicated that there was cross-talk in certain channels in the TDC between the 'channel hit' logic signal, which notes the presence of an input pulse in that channel, and the analog charge signal from which the time is determined. It was noticed that sets of 4 TDCs on the 64 channel module caused time shifts to occur in other TDC channels. Interestingly, the shifts did not have any dependence on the timing of the signals that were input to the sets of 4 TDCs causing the shifts — it mattered, only, that there was data in the channels. Information from Kinetics about the design of the TDC suggested a cause for this. Essentially, the Kinetics F432-001 64 channel TDC is a differential analog to digital converter whose input is the multiplexed signal from 65 time to charge (TQC) converters : 64 stop channels and 1 start channel. The 65 TQCs are, actually, small daughter cards that are attached to the mother board of the unit. The TDC has an output called the 'hit bit' which signifies that there was a time signal in one of its 64 channels. This 'hit bit' is derived from logic data from the daughter cards and is the grand OR of all the channels. The hit information data from daughter cards, themselves, are arranged so that groups of 4 form a wire-wrapped OR and these ORs are wired onto the mother board where the grand OR is formed. Thus, here was the manner in which the TDC channels were grouped in 4. A possible explanation for the shifts was cross-talk between the wire-wrapped OR signal traces on the mother board and the TQC output signal traces on the mother board. This was tested on a couple of

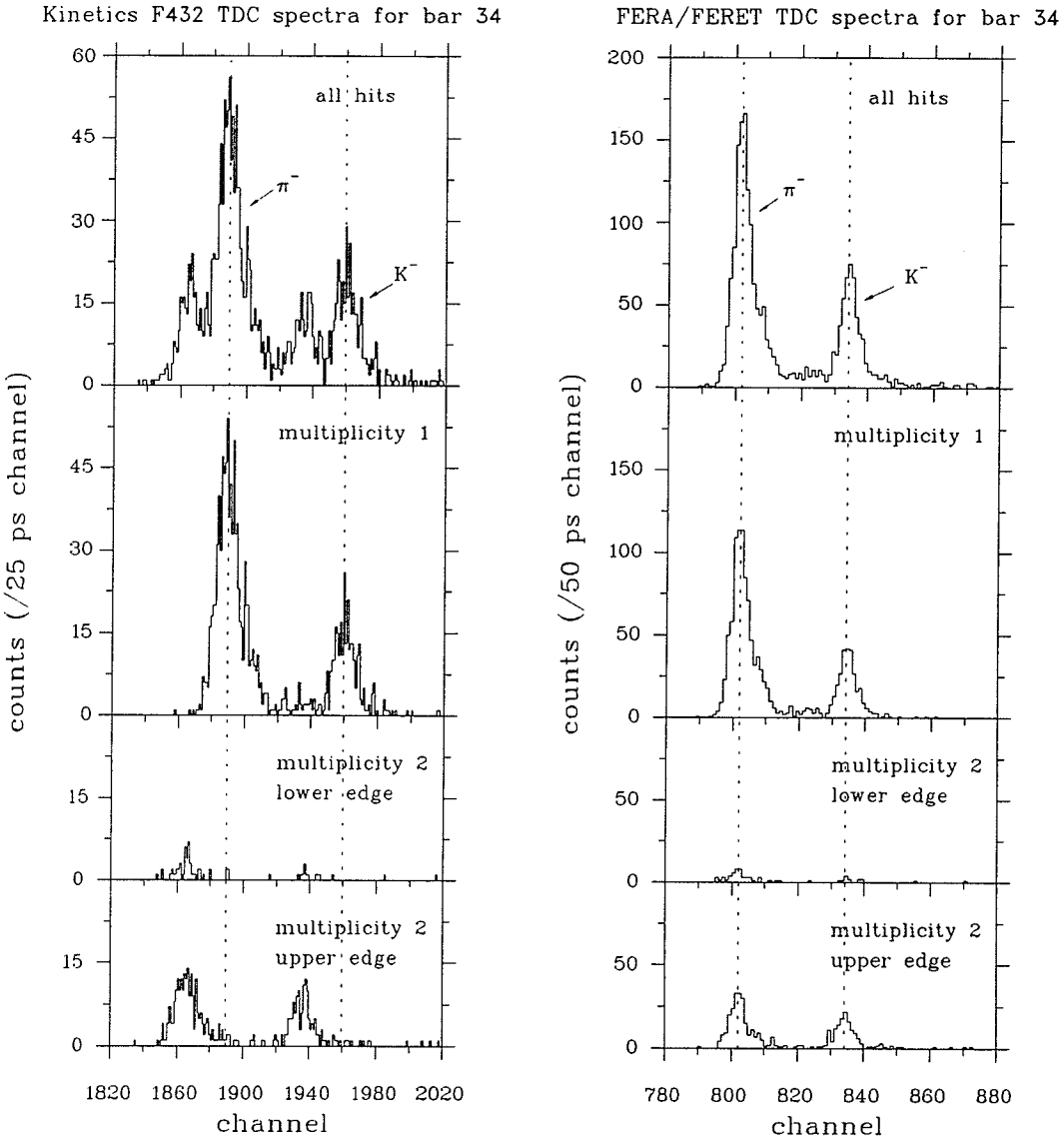

Figure 34: *Time average spectra for module 34 with both the Kinetics and Lecroy FERA/FERET TDCs from data taken during the BCL calibration. There should be two peaks corresponding to* π^- *and* K^-.

TDC channels which had the anomalous shifts from certain group of 4 channels. When the suspected wire-wrapped OR was disconnected from the mother board, the shifts in the TDC channel disappeared. Kinetics was studying the problem to confirm the information at the time of this writing. The problematic TDCs must now be repaired or replaced.

5 The Neutron Time of Flight Arrays

The neutron time of flight arrays consist of two identical arrays, each comprising fifty scintillator modules for neutron detection arranged in five layers of ten modules, providing a minimum of ~25.4 cm thickness of scintillator through the entire stack. An additional nine scintillator modules, each of 0.95 cm thickness, provide a veto layer to reject charged particles. Two long narrow scintillator fingers which span the width of the array are included to help monitor the performance of the arrays. All but the finger scintillators are viewed by two photomultiplier tubes, one at each end. The photomultiplier tube signals are monitored for both timing and signal size. The arrays are physically situated on either side of the experimental target and are suspended from a platform designed to hang these arrays and to hold the experimental target. Details of the various components of the neutron arrays follow in the next few sections.

5.1 The Veto Modules

The veto modules are made from 20.3 × 182.9 cm^2 (8.0" × 72.0") sheets of BC-408 scintillator of nominal thickness 0.95 cm ($\frac{3}{8}$"). The narrow ends of the scintillators are viewed by 2" diameter RCA-8575 photomultiplier tubes through twisted strip adiabatic light guides.

5.2 The Neutron Modules

The neutron modules are made from 15.24 × 182.9 cm^2 (6.0" × 72.0") frontal area size scintillator of 5.08 cm (2") nominal thickness. The ends of the scintillators are viewed by 2" diameter XP-2262H photomultiplier tubes via a simple tapered light guide. Most (80) of the 100 modules were constructed with recently fabricated scintillator (early 1989) while the other 20 were older scintillators which had been in use for several years on other experiments. The old

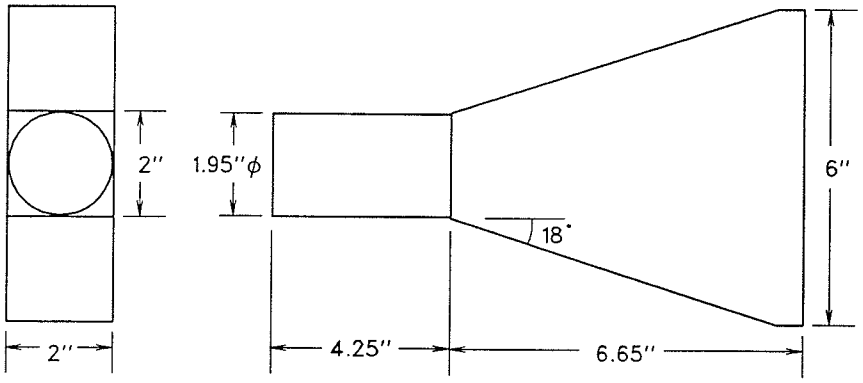

Figure 35: *The lightguide on each end of the neutron array modules.*

scintillators were placed in the final layer of 10 modules in each array so that the four layers closest to the target had all new scintillator. The old scintillator is Pilot-F made by Nuclear Enterprises Ltd. while the new scintillator is BC-408 made by Bicron Corporation which is Bicron's equivalent to Pilot-F. These scintillators have long attenuation lengths and are quite fast (its light output has relatively fast rise and decay times). A long attenuation length is important for bars of the length used here. The lightguides are of a simple design reducing the 2"×6" cross-section of the scintillator into a 2"×2" square which is attached to a 1.95" diameter circular cylinder to which the PMT couples. (See figure 35.) The material from which the lightguides were made is ultraviolet absorbing (UVA) plexiglass as tests against ultraviolet transmitting (UVT) plexiglass showed no performance advantage for the UVT plexiglass. The lightguides on the old modules are similar but have rounded edges. The XP2262 is a 19-pin 12-stage PMT with a maximum spectral sensitivity at ~420 nm which matches well against the 425 nm frequency of maximum emission for BC-408.

A schematic drawing of an end view of the scintillator array showing the relative positions of the veto and neutron scintillators in given in figure 36. Note that there are ~2.5 cm air gaps between the neutron bar layers.

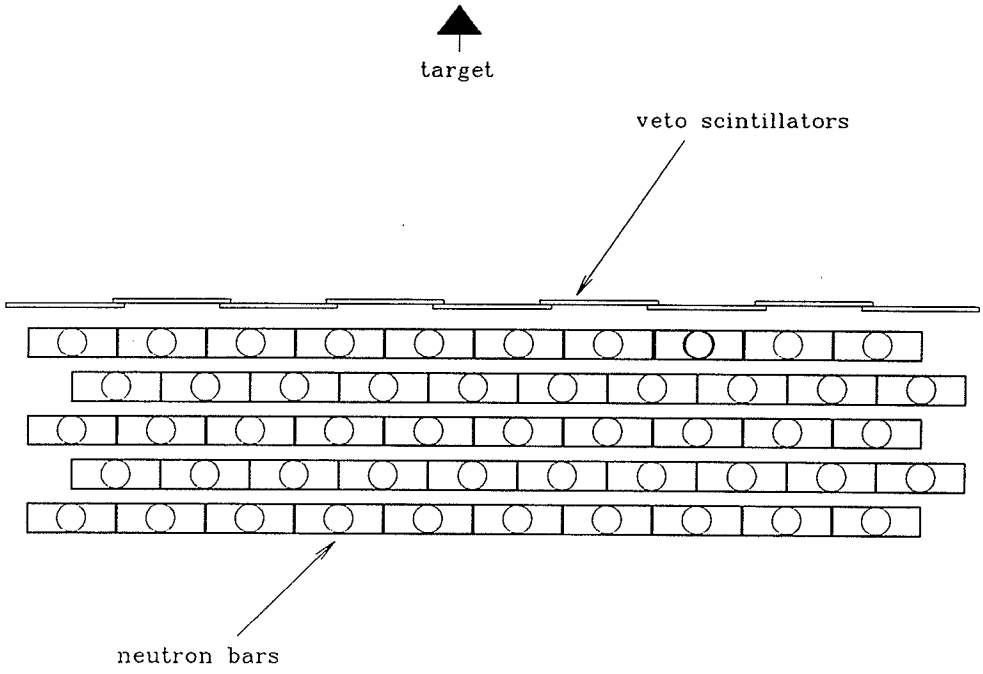

Figure 36: *End view of an array showing the relative positions of the veto and neutron scintillators.*

5.3 The Finger Counters

The two finger counters on each array are located behind the fifth and final layer of the neutron bars and lie with their long axes perpendicular to the long axes of the neutron bars. Thus only very penetrating charged particles, such as elastically scattered pions, will reach them having to travel through at least 26 cm of scintillator. One finger is located at the mid-point between the ends of the neutron bars while the other is located parallel to and 76 cm above the first. The dimension of each finger scintillator is $1 \times 1 \times 183$ cm^3 and is viewed by one Hamamatsu H3167 photomultiplier tube and base.

5.4 The Photomultiplier Bases for the Veto and Neutron Modules

The voltage divider chain that powers the PMT along with the entire PMT base assembly was custom designed. At the time of the design of the arrays, existing photomultiplier bases that were available could not be suitably incorporated into the detector without significant modifications to the base or, otherwise, without some unwieldy mechanical attachments. Quite significantly, the custom photomultiplier base was much less costly than other bases. The base was designed by G. Herb Coombes with the assistance of the University of Manitoba Group at TRIUMF in Vancouver. The base is very light weight due to its construction from polyvinylchloride (PVC) and is attached to the circular cylindrical light guides of the counters via a rubber O-ring taped onto the light guide and connected with a standard 2" PVC pipe plumbing fixture. Figure 37 shows a cross-section view of the GHC base. Both the RCA-8575 and the XP-2262H are 12-stage photomultiplier tubes but are not pin compatible. In fact, the former has a 21-pin assembly while the latter has a 19-pin assembly. Nonetheless, the voltage divider circuit that powers both tubes is the same electronically. Figure 38 shows a schematic of the voltage divider chain.

5.5 Electronics

The photomultiplier tube signals for all the veto and neutron modules are monitored by ADCs and TDCs. A schematic diagram of the monitoring electronics is shown in figure 39. The signals from the photomultiplier tubes are split, passively, and fed into the input of an ADC and into a constant fraction discriminator. The split ratio of the timing to signal size output is 10 to 1. The output of the CFD is then fed into a TDC via a NIM to ECL signal logic converter. Table 16 lists some of the specifications of the electronic components.

Table 16: *Some specifications of the neutron array electronics.*

CFD:	Ortec 934	- 4 channels - 100 MHz maximum input/output rate - 0 to –10 V input - –30 to –1000 mV adjustable threshold - $\leq \pm$ 150 ps walk - adjustable walk compensation network
TDC:	Kinetics F432-A01	- 64 channels - 12 bit resolution - 25 ps minimum LSB - common STOP - <300 μs conversion time
ADC:	Lecroy 1885F	- 96 channels - 15 bit resolution - 50 fC sensitivity - 8 event buffer - 265 μs conversion time

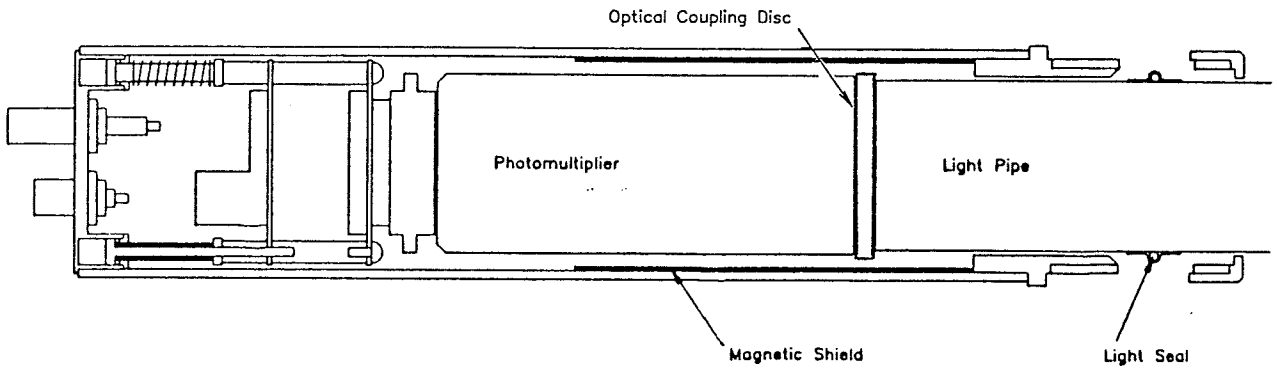

Figure 37: *Cross-sectional view of the GHC PMT base used in the veto and neutron modules.*

5.6 Calibration of Neutron Modules

The arrays were assembled in December 1989 to be used in BNL AGS Experiment 788 which studied the lifetime of single hypernuclei decay. After that experiment ran, the arrays were moved to the experimental area of the new beamline and were rewired with reduced signal cable lengths. To determine the calibration constants of the array modules in each of Experiment 788 and the H particle search, the arrays were lowered to the floor of the experimental area from their nominal hanging position for the runs and layed parallel to the ground for cosmic ray calibrations. Coincidence telescopes for the calibration were placed above and below the array stacks to define the cosmic ray trajectories through the array modules. Scintillators of 12 cm wide and ~150 cm long were positioned across the width of the arrays made up the coincidence telescope.

One coincidence telescope was located at the mid-point of the lengths of the bars and another was located 76 cm away. The former pair allowed the time difference offsets at the centre of the bars to be determined and the two pairs,

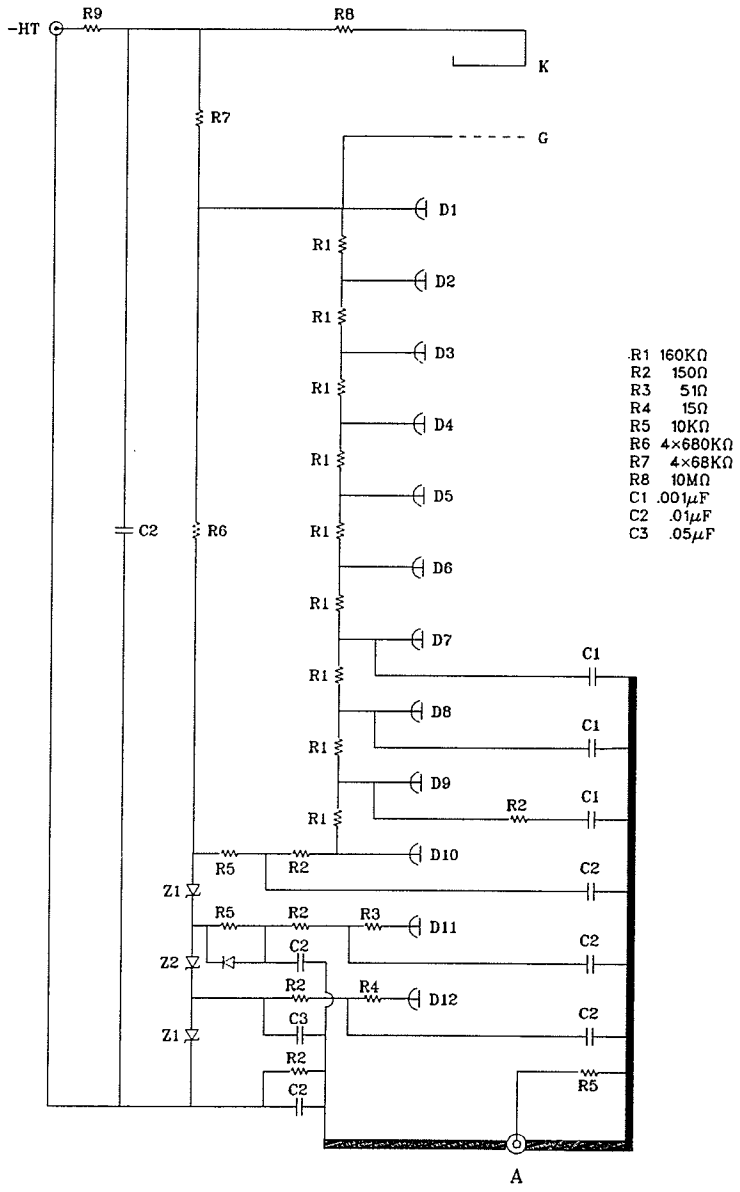

Figure 38: *Electronics diagram of the GHC PMT voltage divider.*

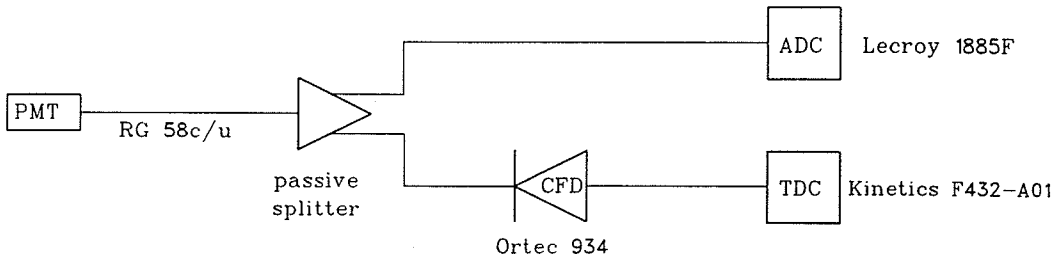

Figure 39: *Schematic of the veto and neutron module electronics.*

together, made it possible to estimate the effective speed of light in the modules. The time difference resolutions of the modules in the right neutron array were, on average, 461 ± 77 ps σ at the mid-point and 576 ± 72 ps σ 76 cm away from the mid-point. The effective speed of light in each module in the right array is plotted in figure 40. The module numbers corresponding to the veto layer are 0 to 9, the first neutron layer are 10 to 19, the second neutron layer 20 to 29 and so on .... The position resolutions of the modules, on average, were 3.7 ± 0.9 cm σ at the centre of the bars and 4.4 ± 0.6 cm σ 76 cm off centre. It is interesting to note that the average speed of light in the first two layers of the neutron modules is less than the average speed of light in the modules of the last three layers. The scintillator bars in the first two layers were put together by the Carnegie Mellon group in Pittsburgh, Pennsylvania, the bars in the third and fourth layers were put together at TRIUMF in Vancouver, BC for the Manitoba group, and the last layer were older existing scintillators. The differences in the manner in which the new scintillator modules were constructed that could possibly affect the speed of light in them were the reflective wrapping surrounding the scintillator and light guide surfaces — aluminum foil at CMU versus aluminized mylar at TRIUMF — and the extent to which surfaces were wrapped with these. In particular, the bars in the third and fourth layers did not have the tapered sides of the light guides exposed to aluminized mylar but had a piece of black matte vinyl placed

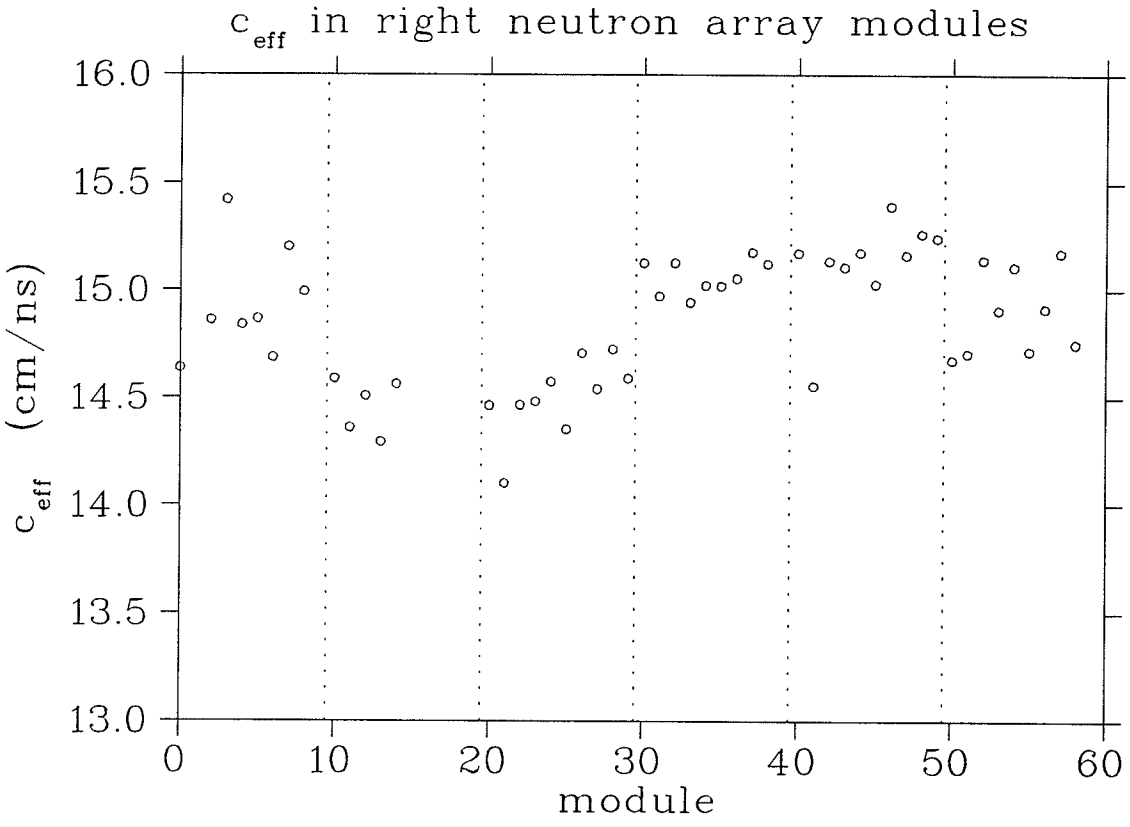

Figure 40: *Comparison of the effective light velocity in most of the elements of the right neutron array.*

against the sides between the aluminized mylar and light guide whereas the first and second layer bars had all their surfaces wrapped in aluminum foil. The black matte vinyl was inserted into the wrapping because preliminary tests with a gamma source on the bars at TRIUMF showed that there was a rather large pulse from light reflected from the opposite end of the bar when the signals from one of the photomultiplier tubes viewing the bar was monitored on an oscilloscope. This addition reduced the signal from the reflected light of the opposite end by $\sim$50%.

Only the relative time of flight offsets for the array modules could be determined with cosmic rays. The absolute offsets required the start timing to be from the IT counters. The time average offsets of the neutron modules were determined relative to that of modules in the first neutron layer corresponding to the same position by accepting only cosmic rays that had essentially vertical trajectories passing through the middle of modules from top to bottom of the arrays. The time average of the modules in the first layer are used as the time of flight start to the stop timing of the modules directly below them. By taking into account the flight time between the modules for the vertical cosmic rays the relative time average offsets of stacks of five modules in line with one another could be calculated. Thus there would be one overall timing constant for each of the ten stacks still to be determined after this. These overall timing constants were derived by aligning them to the photon peak observed during the experimental run: The photons were γ rays emitted from the target region due to interactions of the beam ($K^- \rightarrow \pi^-\pi^0$, $\pi^0 \rightarrow \gamma\gamma$).

The time average STOP resolution determined from the cosmic ray calibration for the modules in layers two to five was 181 ± 21 ps σ, on average.

Since both the start time and stop time were neutron modules and if the individual modules are assumed to have the same timing resolution then the start and stop timing resolutions are the same and the intrinsic average time

average resolution of the modules is simply a factor of $\frac{1}{\sqrt{2}}$ less than the above value, *i.e.* 128 ± 15 ps σ.

5.7 Monte Carlo Estimates of the Neutron Array Efficiencies

The efficiencies of the neutron detectors are required to determine quantities such as counting rates of events and consequently their cross-sections. In general, experimentally measuring the efficiencies of neutron detectors is difficult to accomplish due to a lack of facilities. Quite fortunately, however, the reaction processes of neutrons in hydrocarbon scintillator can be modeled in a Monte Carlo algorithm that yields good agreement with measured efficiencies of various scintillating detectors. Cecil, Anderson and Madey [39] refined an efficiency calculation code, developed by several others authors, that predicted efficiencies that agreed with experimental results to within a few percent for neutron energies from 1 MeV to about 300 MeV. This code is the basis for the calculation of the efficiency of the above neutron arrays which is presented here.

As noted earlier, the detection of neutrons relies upon the indirect observations of charged particles that are a result of interactions with the neutrons. The Monte Carlo code of [39] considers the following neutron interactions, both light producing and scattering, in plastic scintillators:

- elastic scattering off protons, $np \rightarrow np$, which is the only significant reaction channel for neutron detection below 5 MeV energy and is the dominant detection mechanism below ~25 MeV,
- diffractive and non-diffractive scattering off carbon, $n + \mathrm{C} \rightarrow n + \mathrm{C}$, which has a negligible light output,
- inelastic scattering off carbon with threshold 4.7 MeV, $n + \mathrm{C} \rightarrow n + \mathrm{C} + \gamma$,

where the γ may be detected by Compton scattering in the scintillator. This channel typically contributes <10% of the light output in the range 6–16 MeV and a negligible amount above 25 MeV.

- the inelastic reaction $n + \mathrm{C} \rightarrow \alpha + {}^{9}\mathrm{Be}$ with a threshold of 6.2 MeV which makes a small contribution to the efficiency for 6–20 MeV neutrons,
- the inelastic reaction $n + \mathrm{C} \rightarrow n + 3\alpha$ (threshold 7.9 MeV) which along with the former of the next reaction pair dominates the detection efficiency above 40 MeV,
- the inelastic reactions $n + \mathrm{C} \rightarrow p + {}^{12}\mathrm{B}$ (threshold 13.6 MeV) and $n + \mathrm{C} \rightarrow n + p + {}^{11}\mathrm{B}$ (threshold 16.0 MeV),
- and the inelastic reaction $n + \mathrm{C} \rightarrow n + n + {}^{11}\mathrm{C}$ (threshold 18.2 MeV) which itself produces no charged particles but adds to the efficiency a small amount by virtue of the possibility of the two resulting neutrons interacting to form charged particles.

The neutron-carbon inelastic cross-sections along with the neutron-proton elastic cross-section are plotted in figure 41.

The program simulates the propagation of neutrons through organic scintillator and determines by Monte Carlo whether or not those neutrons interact within the scintillator boundary. The input parameters for the program are the neutron energy, the dimensions of the scintillator, the orientation of the neutron trajectories as they impinge upon the scintillator surface, and the position on the scintillator surface where the neutrons enter. It can accommodate scintillator shapes that are either right-rectangular or right-circular cylindrical blocks and allows the initial hit position of the neutrons to be randomly distributed anywhere on the incident surface of the scintillator. If there is an interaction of the neutron within the scintillator, the program then chooses by Monte Carlo

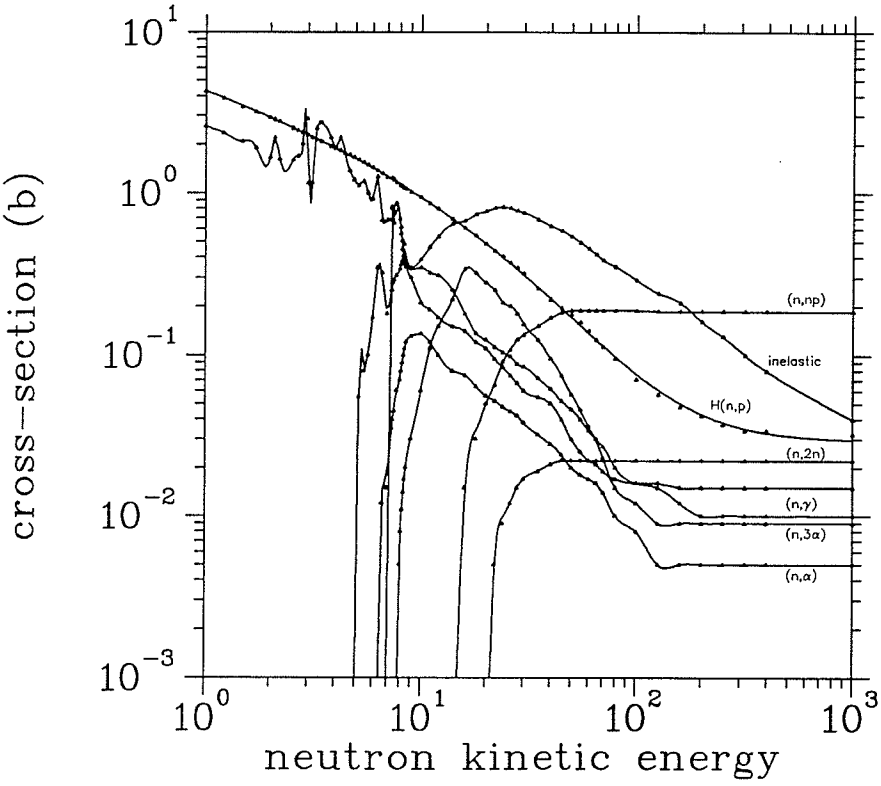

Figure 41: *Neutron-proton and neutron-carbon interaction cross-sections utilized in the neutron efficiency Monte Carlo code by Cecil* et al. *[37]*

what type of reaction has occurred and then calculates the amount of energy deposited in the scintillator, if any, by the charged particles produced. Charged particles which escape from the scintillator have the energy that they do deposit in the scintillator calculated from range-energy and energy-range curves for plastic scintillator.

The efficiency of the neutron arrays discussed here were estimated using the Cecil *et al.* [39] code with some modifications made to account for the particular aspects of the arrays. Since the detectors were composed of independent scintillator modules the program was modified so that it correctly determined the energy deposited in each module. This was done by following the Monte Carlo determined interaction length of a neutron through the array, taking into account the gaps between the layers of modules, until the neutron travelled the appropriate distance in scintillator to one of the modules or until it left the array. For a neutron interacting within the scintillator array, any charged particles produced in an interaction were followed through the modules until they stopped or until they left the array. Most of the charged particles stopped in the same scintillator module in which they originated. Charged particles that had sufficient energy and were produced close enough to the boundary of a scintillator module to escape it were followed onto the next scintillator module they encountered along their trajectories. Their energy losses in travelling through the opaque light tight wrapping of the modules and the air gaps in between those modules were estimated from curves fitted to the range-energy tables for polyethylene and air at standard temperature and pressure produced by Janni [40]. (Logarithmic polynomials were fitted to the table data as was done by Cecil *et al.* for the range-energy relationship of protons in plastic scintillator.) The opaque wrapping was taken to be 0.38 mm thickness polyethylene for all the modules — in actuality, the modules in layers three and four were wrapped in opaque black vinyl.

Table 17: *The solid angles subtended by the neutron array layers assuming a point source target.*

layer number	distance to back face (m)	solid angle Ω, (sr)
1	1.05	1.63
2	1.13	1.49
3	1.21	1.36
4	1.28	1.25
5	1.36	1.14

The other modification to the code was done to account for the geometry between the experimental target and the arrays. The efficiency calculation was done assuming the neutrons originated form a point source at the experimental target centre thus this factor had to be taken into account. The arrays were positioned with the first layers at approximately 1 m distance from the target and given the size of the active detector volume allowed for neutrons at relatively large angles (up to $\sim 35°$) relative to the normal of the detector face to travel through the arrays. Hence, the distance through scintillator that the neutrons traverse varies by significant amounts depending on their trajectory and, thus, the efficiency will vary accordingly. To average out the efficiency calculated from such a geometry, provisions for an isotropically random point source were inserted into the program.

The overall efficiency of the array was determined by taking the weighted average of the efficiencies determined for neutrons from the target randomly impinging upon the solid angle subtended by each layer in the array. The layers

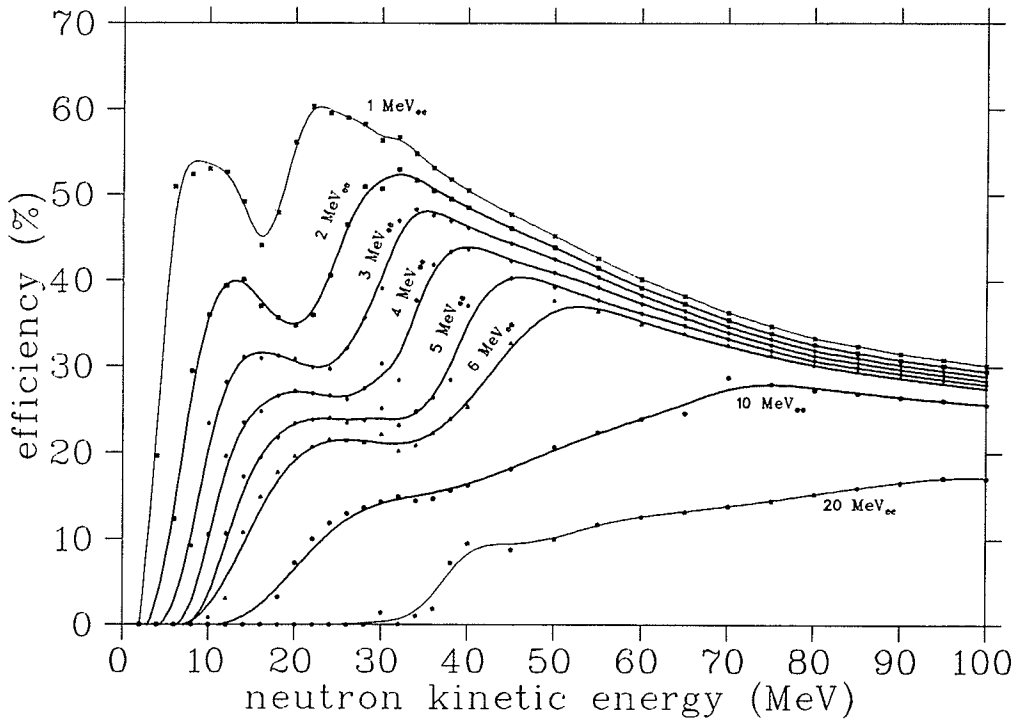

Figure 42: *Estimated neutron efficiency for each of the neutron arrays.*

were taken to be 183 × 157.5 cm^2, which included the area covered by the offset of the adjacent layers, for the solid angle calculation. Table 17 lists the solid angles covered by each of the five layers in the array. Figure 42 displays the results of the overall efficiency calculated with the Monte Carlo simulation. The various curves correspond to different threshold values of energy deposited in one module of the array and is represented in electron equivalent energy. As expected the higher the threshold is the lower the efficiency becomes. During the run the hardware threshold of the discriminators monitoring the neutron module photomultiplier tubes was set to about 2 MeV$_{ee}$ to reduce the rate from the background particles flooding the arrays.

6 Summary

The calibration and performance of the K^+ and neutron time of flight scintillation detectors in a search for the H particle has been presented in this document. The calibration of the K^+ time of flight array was done by reversing the experimental spectrometer dipole to bend the beam particles, which were mostly π^- at the time of the calibration, up into the array. For the 40 modules in the K^+ array, time of flight calibration constants were determined from the known flight path lengths and momenta of the the beam particles and mid-point timing calibration constants were determined with position defining finger scintillators located behind the array. The overall time of flight resolution of the K^+ modules was 0.29 ± 0.04 ns FWHM (or 0.12 ± 0.02 ns σ) including the contribution from the timing start scintillators which had a resolution of 0.16 ± 0.04 ns FWHM (or 68 ± 8 ps σ). The position resolution along the length of the 2 m bars was 3.5 ± 0.7 cm FWHM (or 1.5 ± 0.3 cm σ), on average, determined from the time difference resolution between the two photomultiplier tube signals from the ends of the scintillator bars and the effective velocity of light measured with the position defining finger scintillators. The validity of the method used to determine the time of flight calibration constants was checked using the data from the finger scintillators. Also, the problems with the Kinetics F432-A01 TDCs which involved anomalous time shifts in the time spectra for multiple bar hit events were resolved.

The intrinsic time of flight resolution of the scintillator elements in the neutron time of flight array was 128 ± 15 ps σ determined from using vertical cosmic rays traversing through the middle of the elements when the array was laid flat along the floor so that the elements were horizontal. The position resolutions of the elements, also determined with cosmic rays, were 3.7 ± 0.9 cm σ at the centre of the bars and 4.4 ± 0.6 cm σ 76 cm off centre of the 183 cm

long bars. A Monte Carlo simulation, which took into account the geometry and modularity of the neutron arrays, was carried out to estimate the neutron detection efficiency of the scintillation detector.

References

[1] R .L. Jaffe, *Phys. Rev. Lett.* **38**, 195 (1977).

[2] P. J. G. Mulders and A.W. Thomas, *J. Phys.* G **9**, 1159 (1983).

[3] P. J. G. Mulders, A. T. Aerts, and J.J. de Swart, *Phys. Rev.* D **17** 260 (1978).

[4] P. J. G. Mulders, A. T. Aerts, and J.J. de Swart, *Phys. Rev.* D **21** 2653 (1980).

[5] K. F. Lui and C. W. Wong, *Phys. Lett.* **113B**, 1 (1982).

[6] A. T. M. Aerts and J. Rafelski, *Phys. Lett.* **148B**, 337 (1984).

[7] M. Oka, K. Shimizu, and K. Yazaki, *Phys. Lett.* **130B**, 365 (1983); *Nucl. Phys.* **A464**, 700 (1987).

[8] B. Silvestre-Brac, J. Carbonell, C. Gignoux, *Phys. Rev.* D **36** 2083 (1987).

[9] A. P. Balachandran, A. Barducci, F. Lizzi, V. Rodgers, and A. Stern, *Phys. Rev. Lett.* **52**, 887 (1984).

[10] R. L. Jaffe and C. L. Korpa, *Nucl. Phys.* **B258**, 468 (1986).

[11] S. A. Yost and C. R. Nappi, *Phys. Rev.* D **32**, 816 (1985).

[12] P. B. Mackenzie and H. B. Thacker, *Phys. Rev. Lett.* **55**, 2539 (1985).

[13] Y. Iwasaki, T. Yoshie, and Y. Tsuboi, *Phys. Rev. Lett.* **60**, 1371 (1988).

[14] U. Straub *et al.*, *Phys. Lett.* **200B**, 241 (1988).

[15] J. L. Rosner, *Phys. Rev.* D **33**, 2043 (1986).

[16] G. Baym, E. W. Kolb, L. McLerran, T. P. Walker, and R. L. Jaffe, *Phys. Lett.* **160B**, 181 (1985).

[17] G. Wilquet *et al.*, *Phys. Lett.* **57B**, 97 (1975).

[18] Shahbazian *et al.*, *Nukleonika* **25**, (1980).

[19] D. P. Goyal *et al.*, *Phys. Rev.* D **21**, 607 (1978).

[20] A. S. Carroll *et al.*, *Phys. Rev. Lett.* **41**, 777 (1978).

[21] H. Ejiri *et al.*, *Phys. Lett.* **228B**, 24 (1989).

[22] B. A. Shahbazian, V. A. Sashin, A. O. Kechechyan and A. S. Martynov, *Phys. Lett.* **235B**, 208 (1990).

[23] A. N. Alekseev *et al.*, *Sov. J. Nucl. Phys.* **52**, 1016 (1990).

[24] S. Aoki *et al.*, *Phys. Rev. Lett.* **65**, 1729 (1990).

[25] S. Aoki *et al.*, Nagoya University preprint, February 1991.

[26] B. O. Kerbikov, *Sov. J. Nucl. Phys.* **39**, 516 (1984).

[27] C. B. Dover, D. J. Millener, A. Gal and D. H. Davis, BNL Preprint – 46383, June 1991.

[28] Experiment 813, AGS Research Proposal, January 1985.

[29] A. T. M. Aerts and C. B. Dover, *Phys. Rev. Lett.* **49**, 1752 (1982).

[30] A. T. M. Aerts and C. B. Dover, *Phys. Rev.* D **29**, 443 (1983).

[31] P. H. Pile, *Nucl. Phys.* **A450**, 517 (1986).

[32] J. Birks, *The Theory and Practice of Scintillation Counting*, New York:Macmillan, 1964.

[33] R. Garwin, *Rev. Sci. Instr.* **23**, 755 (1952).

[34] T. Massam, *Nuc. Instr. Meth.* **141**, 251 (1977).

[35] H. Hinterberger and R. Winston, *Rev. Sci. Instr.* **37**, 1094 (1966).

[36] W. Braunschweig, E. Königs, W. Sturm, W. Wallraff, *Nuc. Instr. Meth.* **134**, 261 (1976).

[37] L. K. Rangan, E. I. Shibata and J. S. Loos, *Nuc. Instr. Meth.* **A276**, 496 (1989).

[38] BNL Experiment 787, private communication.

[39] R. A. Cecil, B. D. Anderson, and R. Madey, *Nuc. Instr. Meth.* **161**, 439 (1979).

[40] J. F. Janni, *Atomic Data and Nuclear Data Tables*, **27**, 147 (1982).